Electronic Theses and Dissertations, 2004-2019

2010

Investigation Of Thermal, Elastic And Load-biased Transformation Strains In Niti Shape Memory Alloys

Shipeng Qiu
University of Central Florida

INVESTIGATION OF THERMAL, ELASTIC AND LOAD-BIASED TRANSFORMATION
STRAINS IN NITI SHAPE MEMORY ALLOYS

by

SHIPENG QIU
B.S. Tianjin University, 2000
M.S. Tianjin University, 2003
M.S. University of Central Florida, 2006

A dissertation submitted in partial fulfillment of the requirements
for the degree of Doctor of Philosophy
in the Department of Mechanical, Materials and Aerospace Engineering
in the College of Engineering and Computer Science
at the University of Central Florida
Orlando, Florida

Summer Term
2010

Major Professor: Raj Vaidyanathan

ABSTRACT

Polycrystalline NiTi shape memory alloys have the ability to recover their original, pre-deformed shape in the presence of external loads when heated through a solid-solid phase transformation from a lower-symmetry $B19'$ martensite phase to a higher-symmetry $B2$ austenite phase. The strain associated with a shape memory alloy in an actuator application typically has thermal, elastic and inelastic contributions. The objective of this work was to investigate the aforementioned strains by recourse to *in situ* neutron diffraction experiments during selected combinations of heating, cooling and/or mechanical loading. The primary studies were conducted on polycrystalline $Ni_{49.9}Ti_{50.1}$ specimens on the Spectrometer for MAterials Research at Temperature and Stress (SMARTS) at Los Alamos National Laboratory. Quantitative information on the phase-specific strain, texture and phase fraction evolution was obtained from the neutron data using Rietveld refinement and single-peak analyses, and compared with macroscopic data from extensometry.

First, the lattice strain evolution during heating and cooling in an unloaded sample (*i.e.,* free-recovery experiment) was studied. The lattice strain evolution remained linear with temperature and was not influenced by intergranular stresses, enabling the determination of a thermal expansion tensor that quantified the associated anisotropy due to the symmetry of $B19'$ NiTi. The tensor thus determined was subsequently used to obtain an average coefficient of thermal expansion that was consistent with macroscopic dilatometric measurements and a 30,000 grain polycrystalline self-consistent model. The accommodative nature of $B19'$ NiTi was found to

account for macroscopic shape changes lagging (with temperature) the start and finish of the transformation.

Second, the elastic response of *B19′* martensitic NiTi variants during monotonic loading was studied. Emphasis was placed on capturing and quantifying the strain anisotropy which arises from the symmetry of monoclinic martensite and internal stresses resulting from intergranular constraints between individual variants and load re-distribution among variants as the texture evolved during variant reorientation and detwinning. The methodology adopted took into account both tensile and compressive loading given the asymmetric response in the texture evolution. Plane specific elastic moduli were determined from neutron measurements and compared with those determined using a self-consistent polycrystalline deformation model and from recently reported elastic stiffness constants determined via *ab initio* calculations. The comparison among the three approaches further helped understand the influence of elastic anisotropy, intergranular constraint, and texture evolution on the deformation behavior of polycrystalline *B19′* NiTi. Connections were additionally made between the assessed elastic properties of martensitic NiTi single crystals (*i.e.,* the single crystal stiffness tensor) and the overall macroscopic response in bulk polycrystalline form.

Lastly, the role of upper-cycle temperature, *i.e.,* the maximum temperature reached during thermal cycling, was investigated during load-biased thermal cycling of NiTi shape memory alloys at selected combinations of stress and temperature. Results showed that the upper-cycle temperature, under isobaric conditions, significantly affected the amount of transformation strain and thus the work output available for actuation. With the objective of investigating the

underlying microstructural and micromechanical changes due to the influence of the upper-cycle temperature, the texture evolution was systematically analyzed. While the changes in transformation strain were closely related to the evolution in texture of the room temperature martensite, retained martensite in the austenite state could additionally affect the transformation strain. Additionally, multiple thermal cycles were performed under load-biased conditions in both NiTi and NiTiPd alloys, to further assess and understand the role of retained martensite. Dimensional and thermal stabilities of these alloys were correlated with the volume fraction and texture of retained martensite, and the internal strain evolution in these alloys. The role of symmetry, *i.e., B19'* monoclinic martensite vs. *B19* orthorhombic martensite in these alloys was also assessed.

This work not only established a methodology to study the thermal and elastic properties of the low symmetry *B19'* monoclinic martensite, but also provided valuable insight into quantitative micromechanical and microstructural changes responsible for the thermomechanical response of NiTi shape memory alloys. It has immediate implications for optimizing shape memory behavior in the alloys investigated, with extension to high temperature shape memory alloys with ternary and quaternary elemental additions, such as Pd, Pt and Hf.

Dedicated
to
my wife and parents

ACKNOWLEDGMENTS

I would like to express my deep gratitude to my advisor Dr. Raj Vaidyanathan. I'm really feeling grateful that he provided me this opportunity to join in a friendly group and work in an exciting area starting 2006. His technical guidance, life counsel and continuous support are highly appreciated. I would also like to express my sincere appreciation to Dr. Linan An, Dr. Kevin Coffey, Dr. Ali P. Gordon, and Dr. Aravinda Kar for serving on my committee and spending their valuable time evaluating my dissertation. I would like to express my special sincere gratitude to collaborators at NASA Glenn Research Center, Dr. Santo Padula II, Dr. Ronald Noebe, Darrell Gaydosh, Dr. Anita Garg and Glen Bigelow; at Los Alamos National Laboratory (LANL), Dr. Bjørn Clausen, Dr. Donald Brown and Thomas Sisneros, for contributing their valuable time and providing numerous valuable suggestions and experimental help.

Moreover, my gratitude is also extended to Cynthia Harle, Angelina Feliciano, Karen Glidewell and Kari Stiles of Advanced Materials Processing and Analysis Center (AMPAC) for their help in arranging all the traveling for me to attend conferences and perform the experiments in New Mexico. I would like to thank all my colleagues in Dr. Raj's group, especially Dr. Vinu Krishnan, Dr. Mahadevan Manjeri, Othmane Benafan and Doug Nicholson. It's really an honor and treasure to me, to know all these friendly and sincere people and form a life-long relationship.

Finally, sincere thanks go to my lovely wife and my dear parents, for their everlasting love, support, encouragement and understanding.

TABLE OF CONTENTS

LIST OF FIGURES

LIST OF TABLES

LIST OF ACRONYMS/SYMBOLS

ADP	Axial Distribution Plot
A_f	Austenite finish
A_s	Austenite start
DSC	Differential Scanning Calorimetry
EDM	Electrical Discharge Machining
GRC	Glenn Research Center
GSAS	General Structure Analysis System
HTSMA	High Temperature Shape Memory Alloy
M_d	Martensite desist
M_f	Martensite finish
M_p	Martensite peak
M_s	Martensite start
NASA	National Aeronautics and Space Administration
SMA	Shape Memory Alloy
SMARTS	Spectrometer for Materials Research at Temperature and Stress
SPF	Single Peak Fitting
TEM	Transmission Electron Microscopy
UCF	University of Central Florida
XRD	X-ray diffraction

CHAPTER ONE: INTRODUCTION

1.1 Motivation

Shape memory alloys (SMAs) have the ability to recover their original shape from macroscopic deformation introduced at low-temperature by heating the material above the phase transformation temperature. The shape recovery can occur against external loads enabling work output in actuator applications [1-4]. This phase transformation provides a unique energy conversion mode between thermal and mechanical energy. Near-equiatomic NiTi is one of the most commonly used commercial SMAs and the transformation is often between a cubic ($B2$) so-called austenite phase and a monoclinic ($B19'$) so-called martensite phase. NiTi SMAs have become one of the preferred choices for designing solid-state actuators due to their capability for large strain accommodation (up to 8%), high work output, excellent corrosion resistance, relatively wide range of operation temperatures achieved through slight compositional variations or thermomechanical treatments, and superior fatigue life, among other benefits [3, 5, 6].

The strain associated with NiTi SMAs in actuator applications typically has thermal, elastic and inelastic contributions. However, a comprehensive understanding of the thermal, elastic, variant reorientation/conversion and detwinning response of $B19'$ martensitic NiTi variants as they exist in bulk, polycrystalline aggregate form still remains elusive. Therefore, a lack of understanding of the aforementioned contributions poses a tremendous challenge in making direct connections between the lattice strain, phase volume fraction and texture evolution associated with the phase transformation at the atomistic scale and macroscopically measurable properties such as thermal

expansion, elastic modulus, transformation temperatures, work output, *etc*. Thus, this work is motivated by establishing such connections in order to provide a better understanding in modeling and engineering these alloys for desired properties and performance. The understanding obtained in this work on the binary NiTi SMAs can be extended to high temperature SMAs with ternary and quaternary elemental additions, such as Pd, Pt and Hf as well. Therefore, the primary motivation for this research was in accordance with the goals of a NASA Fundamental Aeronautics Program (FAP) project - to develop a suite of stable, high work output SMAs for a range of applications applicable at different stresses and temperatures, for use in adaptive structures and actuators through a fundamental understanding and control of material properties.

In situ neutron diffractions measurements during selected combinations of heating/cooling and mechanical loading on SMAs provide a unique approach to follow the quantitative micromechanical and microstructural changes, *e.g.,* volume fraction, intergranular strain and texture, during phase transformation. The diffraction experiments were performed on the Spectrometer for MAterials Research at Temperature and Stress (SMARTS) at Los Alamos National Laboratory (LANL). Compared to a conventional x-ray source, the increased penetration of neutrons is more representative of bulk polycrystalline behavior and is typically free of surface effects. This is particularly relevant for the measurements of SMAs, since polycrystalline samples differ significantly from single crystals due to the role of texture and intergranular stresses between grains.

Specifically, this work is motivated by the following:

1. No comprehensive experiments have been done to quantitatively follow the phase transformation associated with shape memory behavior in the absence of external loads. The anisotropic thermal expansion character of *B19′* martensitic NiTi variants is not clear yet. There is also a need to make available parametric and experimental input for various existing models of shape memory behavior.

2. The thermomechanical response of *B19′* martensitic NiTi variants in polycrystalline specimens can be complicated by the anisotropy which arises from the symmetry of monoclinic martensite (*i.e.,* the thirteen independent stiffness or compliance tensorial elements and four constants in the coefficient of thermal expansion tensor) and internal stresses that are influenced by intergranular constraints between individual martensite variants and load re-distribution among variants as the texture evolves due to variant reorientation and detwinning. The elastic response of individual *B19′* martensitic NiTi variants as they exist in bulk, polycrystalline aggregate form has not yet been explored.

3. A preliminary study showed that the maximum temperature reached during thermal cycling under constant stress significantly affected the observed thermomechanical response of NiTi SMAs, especially the amount of transformation strain available for actuation and thus the work output. However, the underlying mechanisms associated with the aforementioned differences in macroscopic response are not clear.

4. Little work has addressed the cyclic performance of SMA actuators in strain-temperature space where the shape memory effect is used. The role of retained martensite during thermal-mechanical cycling in NiTi and NiTiPd SMAs is not clear. Lack of such experimental data and understanding thus has become a major barrier for present and potential applications of shape memory actuators.

5. No emphasis has been placed on comparing the behavior of isolated micron-sized single crystals with their behavior when consolidated in bulk polycrystalline form, where the individual grain is constrained by surrounding material.

Experiments were hence designed to address the aforementioned issues, analyzed correspondingly and presented in this work.

1.2 Organization

The following table summarizes the content of each of the following chapters:

Chapter	Subject
2	Introduction to shape memroy alloys
3	Introduction to neutron diffraction and method of data analysis
4	Measurement of the lattice plane strain and phase fraction evolution during heating and cooling during free recovery in NiTi and determination of the thermal expansion tensor of the $B19'$ martensite
5	Study of elastic moduli and elastic anisotropy in polycystalline $B19'$ martensitic NiTi
6	Study of the effect of upper-cycle temperature on the load-biased strain-temperature response of NiTi
7	Study of the role of retained martensite during thermal-mechanical cycling in NiTi and NiTiPd
8	Identification of hard/easy directions in austenitic NiTi during phase transformation
9	Conclusions

CHAPTER TWO: INTRODUCTION TO SHAPE MEMORY ALLOYS

Shape memory alloys have emerged as an important material of considerable scientific and commercial interest. Due to the stand-alone nature of each of the following chapters, review of the literature has been done relevant to each topic addressed in the respective chapters. Hence, this chapter briefly introduces the history of shape memory alloys, presents the two major mechanisms associated with the shape recovery process – shape memory effect and superelasticity, and provides a sampling of various applications that use binary NiTi shape memory alloys.

2.1 Shape Memory Alloys

Shape Memory Alloys (SMAs) can remember their original or pre-deformed shape by undergoing a reversible solid-state phase transformation, induced either by temperature (shape memory effect) or stress (superelasticity). The phase transformation, between martensite (low temperature, low symmetry phase) and austenite (high temperature, high symmetry phase), is first-order, displacive and diffusionless. SMAs can accommodate strains up to 8% in their martensite phase. The strain recovery from martensite to austenite can take place against large forces (up to 500 MPa), resulting in their application as actuators [3, 7].

The first observation of the transformation which yielded the shape memory effect was made in 1932 in Au-Cd by Arne Ölander [8]. Six years later, in 1938, the transformation was observed in Cu-Zn by Greninger *et al.* [9]. A more detailed study of shape-memory behavior in Au-Cd was

made by Read and co-workers in 1951 [10]. It was not until 1962, that Buehler and co-workers [11] at the Naval Ordinance Laboratory, discovered the shape memory effect in an equiatomic alloy of NiTi. This alloy was named NITINOL, in honor of their workplace where the discovery of NiTi was made. Since then, extensive research has been carried out to better understand the physical and mechanical properties of these alloys and potential applications continue to be sought.

2.1.1 Shape Memory Effect

The shape memory effect refers to the ability of SMAs to recover/remember their original, pre-deformed shape when heated through a martensitic phase transformation. The martensitic phase transformation is a lattice transformation where a shearing deformation is involved as a result of the cooperative movement of atoms [7], resulting in a one-to-one lattice correspondence between the parent austenite phase and the resulting martensite phase. The whole shape recovery cycle associated with the shape memory effect is illustrated in Fig. 2.1. During cooling from the high temperature austenite phase without constraint, a self-accommodated martensite structure is formed. Due to its lower symmetry, this twinned martensite structure takes the original shape of the austenite phase by orienting the variants of the resultant martensite in various morphologies, thus showing no macroscopic deformation. When load is applied on the self-accommodated structure, detwinned martensite is formed to accommodate the strains that exceed the elastic regime which results in macroscopic deformation that remains even after unloading. However, no dislocations (which result in permanent deformation) are introduced during the martensite variant reorientation and/or detwinning process. The recovery process is initiated by heating the

6

deformed specimen through the phase transformation to the parent austenite phase to recover the macroscopic strain.

Fig. 2.2 shows a typical elongation versus temperature response of a shape memory alloy under a constant tensile load (also known as a load-bias test). During cooling from the austenite phase, the forward phase transformation starts at M_s (martensite start) and finishes at M_f (martensite finish). Upon heating, the reverse phase transformation from martensite to austenite begins at A_s (austenite start) and finishes at A_f (austenite finish). Also shown is the total shape recovery during the thermal cycle (ΔL) and the amount of hysteresis (ΔT) by comparing heating and cooling curves, which can be defined as the difference between the martensite formation temperature and the austenite formation temperature.

The shape memory effect can have either one-way or two-way character. One-way shape memory effect occurs when the SMA can only remember its original high temperature shape. On the other hand, two-way behavior enables the alloy to remember the low temperature deformed shape as well, which normally is achieved by "biasing" or "training" the SMA specimen by cycling between its low temperature shape and high temperature shape [3].

2.1.2 Superelasticity

Another unique property of shape memory alloys is superelasticity or pseudoelasticity. Superelasticity is a deformation mechanism where the high-temperature high symmetry phase transforms to a low-temperature, low symmetry phase, when subjected to an external applied

7

stress, thus producing a macroscopic strain that augments the elastic strain. Upon removing the stress, the low symmetry phase is no longer stable and transforms back to the high symmetry phase, resulting in a complete recovery of the macroscopic strain at the end of the mechanical cycle [7, 12]. The typical superelastic loading-unloading stress-strain response under isothermal conditions is shown in Fig. 2.3 for binary NiTi. Compared with the shape memory effect, the phase transformation involved during superelasticity is stress induced, rather than temperature induced. In various engineering applications [3], superelastic alloys are normally subjected to repetitive loading and unloading, accompanied by forward and reverse martensitic transformations of the parent austenite phase.

2.2 NiTi Shape Memory Alloys

Even though a wide range of SMAs are found to exhibit the shape memory effect or pseudoelasticity, NiTi alloys are considered to be one of the most practical systems owing to the combination of their superior material properties and commercial availability. In the case of near equiatomic NiTi, shape recovery occurs as a result of a thermoelastic phase transformation from a monoclinic, *B19'*, martensitic structure at low temperatures to a cubic, *B2*, austenitic structure at high temperatures. Variation in the composition and thermomechanical processing can change, *e.g.,* the transformation temperature, transformation pathway (*e.g.,* an intermediate trigonal *R*-phase can be formed during cooling from the *B2* phase) and hysteresis range, which in turn determines their final application that utilize either the shape memory effect or superelasticity.

Fig. 2.4 shows the equilibrium phase diagram for NiTi [4, 13]. The small inset shows metastable phase equilibrium between TiNi and Ti_3Ni_4, which is crucial in adjusting transformation temperatures and in determining optimum heat-treatments for improving shape memory characteristics. Further details can be found in Section 8 and 9 in Ref. [4]. On the Ni-rich side close to near equi-stoichiometry, a slight variation in the composition from 50 at.% to 51 at.% of Ni drastically changes the transformation temperature from around 70 °C to approximately - 120 °C. In contrast, on the Ni-lean side of near equi-stoichiometry, the transformation temperatures are less sensitive to compositional changes. Excess Ti can be precipitated out as Ti_2Ni phase, which keeps the matrix at near stoichiometric composition.

Due to their unique properties, NiTi SMAs have generated tremendous commercial interest. Fig. 2.5 shows some of the applications utilizing their superelastic effect, which includes stents, orthodontic wires, mobile phone antennae and eyeglass frames [14]. Fig. 2.6 shows Boeing's design of a variable geometry chevron (VGC) that incorporates beam components of NiTi [15]. The idea behind the design is that the shape of the chevron can be actively controlled with SMAs and assumes different geometries during take off, landing and cruise, which can mitigate noise and maximize fuel efficiency, respectively. More details about typical properties and representative applications of NiTi SMAs can be found in Refs. [3, 5, 12, 16, 17].
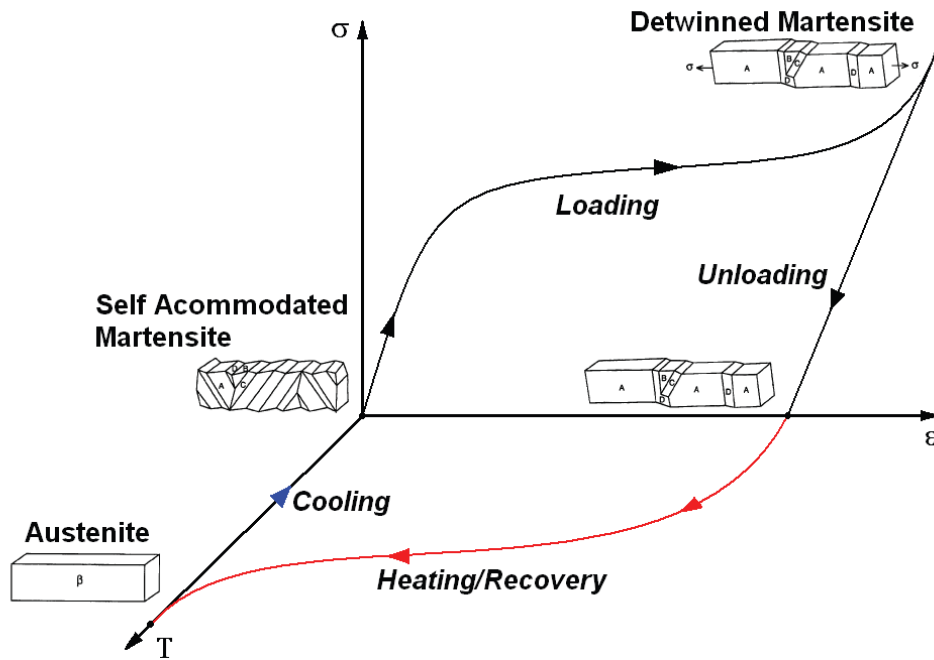
Figure 2.1 A representative stress-strain-temperature curve showing the shape memory effect [18]
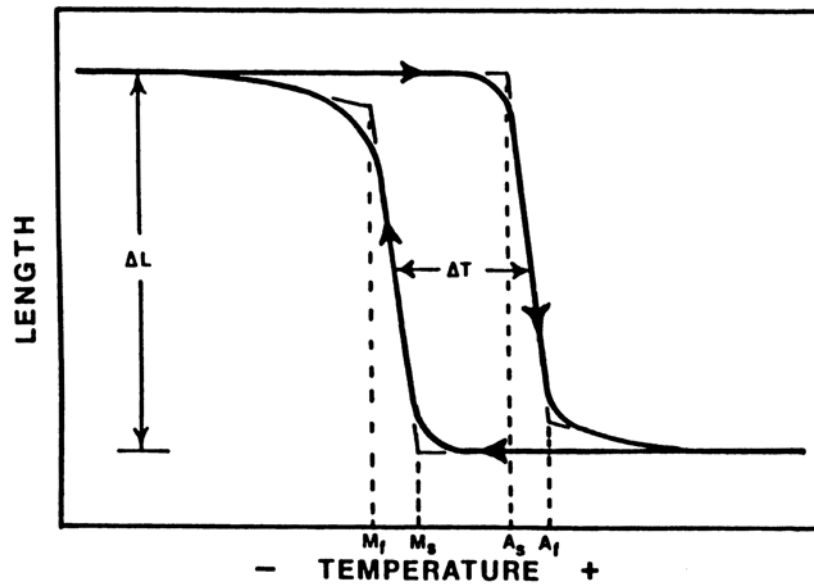
Figure 2.2 Representative thermally induced phase transformation curves showing four critical transformation temperatures - austenite start (A_s), austenite finish (A_f), martensite start (M_s), martensite finish (M_f), hysteresis (ΔT) and shape recovery (ΔL) associated with the shape memory effect [19]
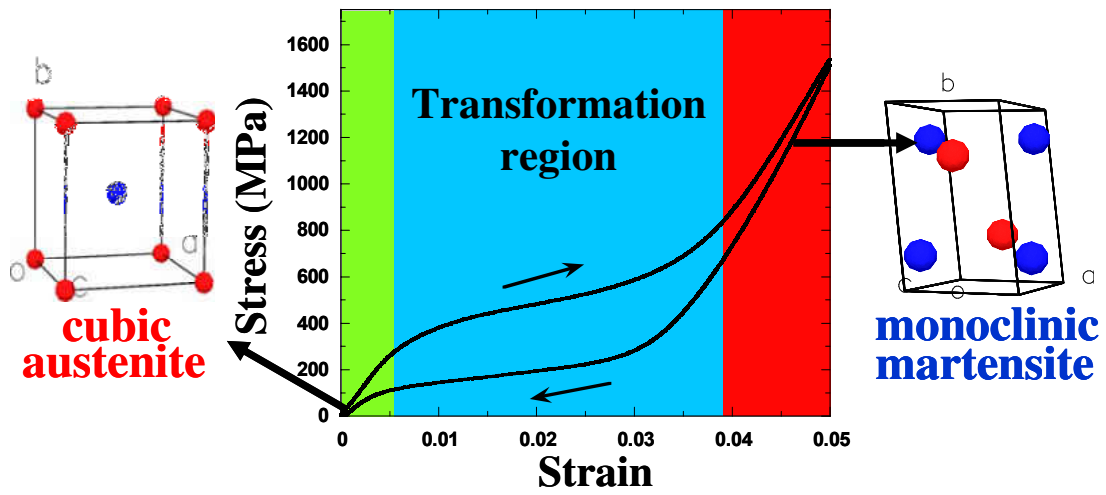
Figure 2.3 Representative stress-strain response of NiTi during isothermal monotonic testing showing superelastic behavior
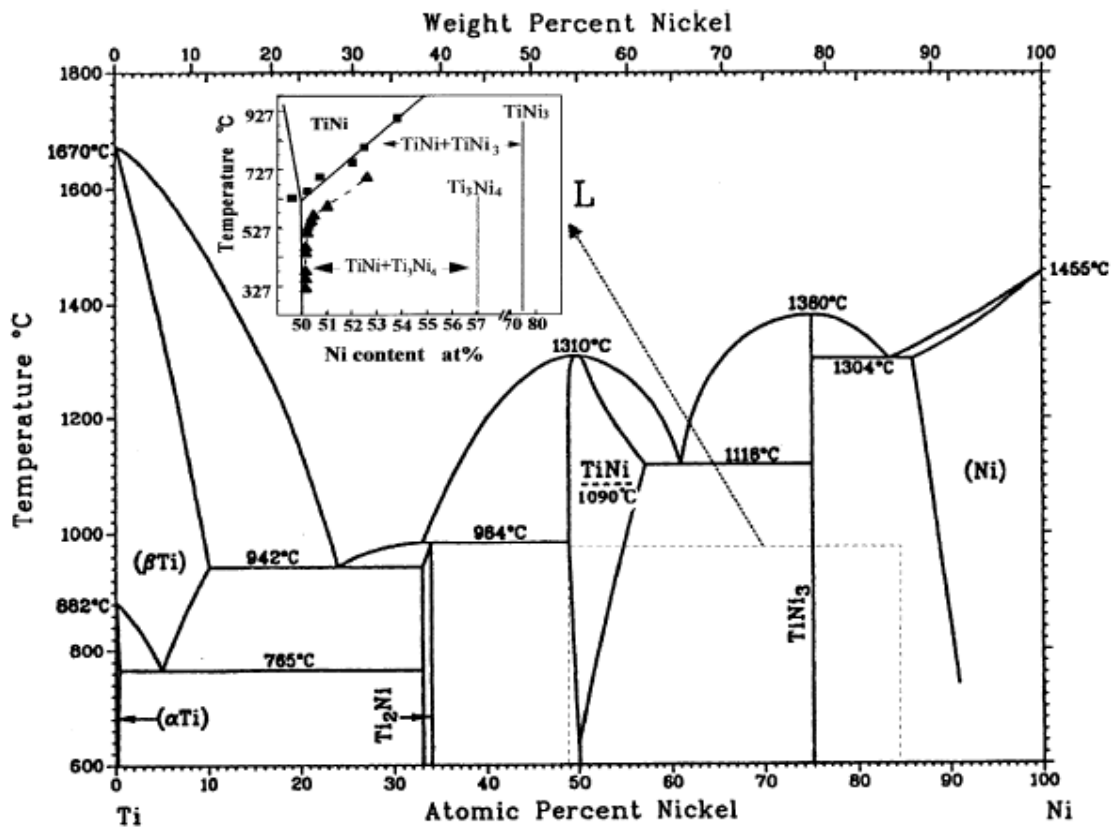
Figure 2.4 Phase diagram of NiTi [4, 13]

11
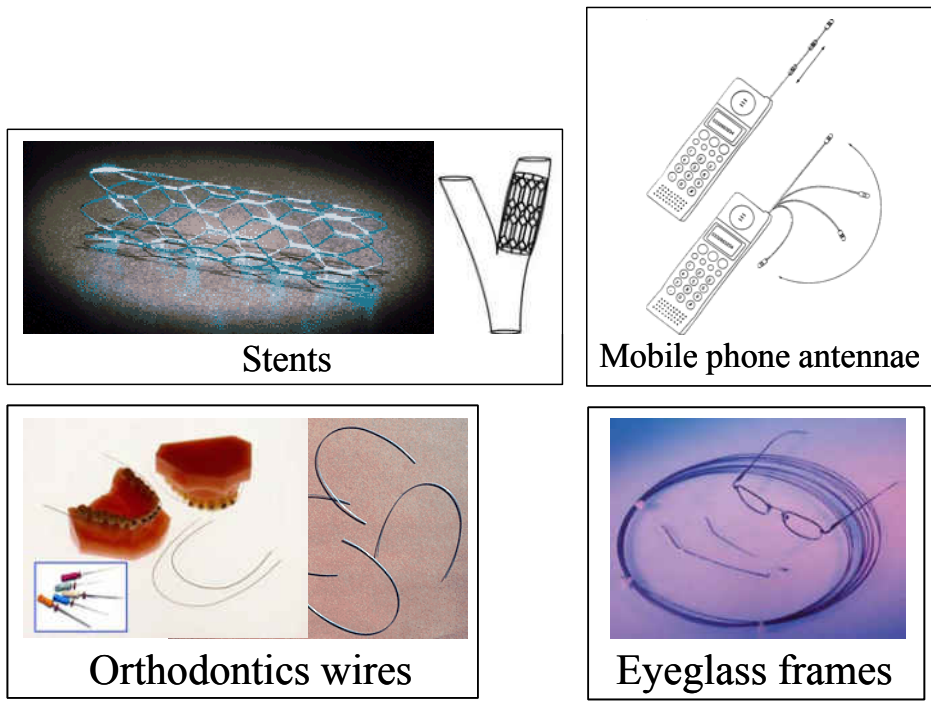
Figure 2.5 Representative applications of superelastic NiTi [14]

Figure 2.6 Shape memory NiTi actuated variable geometry chevrons [15]

CHAPTER THREE: NEUTRON DIFFRACTION AND NEUTRON SPECTRA ANALYSES

In this chapter, the neutron diffraction technique is first briefly introduced. Quantitative phase specific information on the evolution of strains, texture and phase volume fractions can be obtained by recourse to Rietveld refinement as well as single peak analyses from the acquired neutron spectra.

3.1 Neutron Diffraction

Free neutrons are ideal tools for the investigation of the atomic and molecular structure in condensed materials [20, 21]. Either reactor or spallation sources can be used for producing free neutrons effectively. For reactor sources, neutrons are produced in a nuclear reactor by the fissioning of atoms in the reactor fuel, which is invariably uranium for research reactors. These neutrons can be extracted from the moderator block and are guided to the experimental devices outside the reactor shielding. For most experiments, monochromatic neutrons are needed, which have to be filtered out from the thermal spectrum leaving the moderator. Some neutron facilities, *e.g.,* the one at the Manuel Lujan, Jr. Neutron Science Center at Los Alamos (LANSCE), on the other hand, use accelerators to produce spallation neutrons, in which neutrons arrive in pulses rather than continuously as they do at a reactor. In this case, monochromator crystals used at reactors are no longer needed and all the neutrons with different wavelengths/energy can be used, compared with those only in a narrow energy band available at a reactor source. When pulsed sources or mechanical choppers are used, the time-of-flight technique can be used to measure the energy and the energy change of neutrons.

While diffraction characterization can be also carried out with x-rays and electrons, scattering interactions between the different beams and materials are different. While the interaction is electromagnetic for x-rays, it is electrostatic for an electron beam. Both of these interactions are strong and neither type of beam penetrates matter very deeply. Neutrons, having no charge, can interact with atomic nuclei via the very short-range strong nuclear force and thus can penetrate matter much more deeply than the aforementioned two types of sources (several millimeters, compared to a few micrometers for x-rays from a conventional source). Therefore, the neutron diffraction technique is especially conducive to studying the bulk behavior of materials, *e.g.,* crystal structure, residual stress, phase fraction, and texture [22]. Further details concerning the theory of neutron diffraction and its application to materials characterization can be found in Refs. [23, 24].

3.1.1 Neutron Diffraction Measurements on SMARTS

The Spectrometer for MAterials Research at Temperature and Stress (SMARTS) at Los Alamos National Laboratory (LANL) was used to conduct the neutron diffraction experiments. SMARTS, performing in "time-of-flight" mode and using a pulsed neutron source, is a third-generation neutron diffractometer optimized for the study of engineering materials. It provides an exciting range of capabilities for studying polycrystalline materials focusing on two areas: the measurement of deformation under stress and extreme temperature, and the measurement of spatially resolved strain fields. SMARTS has two banks of detectors, Bank 1 and Bank 2, one opposing the other, as is shown in Fig. 3.1. The loading axis forms an angle of 45 degree with the incident neutron beams, so that the two banks can collect diffracted beams from two directions, respectively: one collects diffracted beams from the lattice planes whose plane

normals are perpendicular to the loading axis (Bank 1), and the other from the lattice planes whose plane normals are parallel to the loading axis (Bank 2). The specimens were mounted horizontally and loaded in uniaxial tension or compression on a servo-hydraulic load frame. Detailed information on the diffraction setup and load/temperature capabilities can be found in Ref. [25]. Neutron diffraction spectra can be simultaneously acquired, with the sample being mechanically loaded and/or subjected to temperature changes, obtaining strain measurements both parallel and perpendicular to the loading direction.

3.2 Rietveld Refinement

The Rietveld refinement technique [26], which was originally introduced for the analysis of constant wavelength neutron diffraction data [27], is being broadly used for the analysis of neutron, x-ray and synchrotron diffraction data nowadays. In the Rietveld refinement [26] technique implemented in the LANL code General Structure Analysis System (GSAS) [28], a mathematic model is developed according to

$$Y_c = Y_b + \sum_h SKF_h^2 P(\Delta T_h). \tag{3.1}$$

The intensity at every point in the raw spectrum is determined by adding the calculated background intensity, Y_b, and Bragg scattering intensities, which contain a scale factor S, a correction factor K, a structure factor F_h and a profile function $P(\Delta T_h)$. The correction factor K contains a term describing the changes in the predicted intensity due to texture and the profile function is further determined by the displacement ΔT_h of the profile point from the reflection position. Thus, the variations in intensity due to changes in phase volume fractions (in multiphase materials) or to preferred orientation (texture) can be accounted for. The refinement procedure varies selected parameters (*e.g.,* atom positions, thermal parameters, profile functions,

phase volume fractions, lattice parameters, and phase texture, etc.), and constructs linear constraints between parameters (*e.g.,* atomic fraction of phase A + atomic fraction of phase B = 100%), until the calculated and measured spectra match in a least-squares fit. Errors are quantified and are associated with the statistics of the fit. A generalized spherical harmonic description [29, 30] was used to account for the evolving texture in the existing phases. The profile function that fits the data best is a combination of two functions: the first is the result of convoluting two back-to-back exponentials with a Gaussian function, and the other is a linear combination of a Lorentzian and a Gaussian (pseudo-Voigt) function. A typical diffraction pattern and Rietveld refinement output is shown in Fig. 3.2. The crosses in red are the measured data and the line through them in green is the Rietveld least squares fit. The red and black tick marks indicate reflections from the martensite and austenite phases, respectively. Errors between refinement and measurement are quantified and represented by the difference curve in purple shown at the bottom of the figure.

3.2.1 Strain Analysis

The technique of using diffraction spectra for internal stress measurements relies on using atomic planes in specimens as internal strain gauges [31]. The distances between atomic planes, directly obtained from diffraction spectra, were used to compute strains. The strain information, then coupled with elasticity constants, provides a measurement of the internal stresses. In the current version of GSAS, the elastic strain ε_{hkl} associated with a plane *hkl* is expressed by

$$\varepsilon_{hkl} = \varepsilon_{isotropic} + \varepsilon_{anisotropic} = \frac{\alpha}{C} + \frac{\beta \cos\phi}{C} + \frac{\gamma A_{hkl}}{C}, \qquad (3.2)$$

where α is a fitting parameters which fits peaks in the diffraction spectrum by varying the lattice

constants a, b, and c so that $\dfrac{\Delta a}{a} = \dfrac{\Delta b}{b} = \dfrac{\Delta c}{c}$ [32]. Based on this definition, α is used to account

for the isotropic phase strain that follows the average polycrystalline deformation, since ε_{hkl} have

no hkl dependence. The second fitting parameter, β, accounts for the anisotropy in a given

direction where ϕ is the angle between the hkl plane normal and the c axis. Following Daymond

et $al.$ [33], a cubic anisotropy factor γ was also used to shift the position of each peak from a

perfect cubic structure by a quantity proportional to γA_{hkl}, where A_{hkl} is given by:

$$A_{hkl} = \frac{h^2 k^2 + h^2 l^2 + k^2 l^2}{(h^2 + k^2 + l^2)^2} \tag{3.3}$$

C in Eq. (3.2) is a diffractometer constant used to convert time-of-flight data to d-spacings. Only

the parameters α and γ were used to fit the cubic austenitic phase. In the case of the monoclinic

or orthorhombic martensite, only the parameters α and β were used during Rietveld refinement.

3.2.2 Texture Analysis

The procedures outlined by Von Dreele [29] for texture analyses were followed and Rietveld

refinement of the acquired neutron spectra was performed using an 8th order spherical-harmonic

description of the texture. Two approaches were adopted to follow the texture evolution in the

martensite and austenite phases. The first representation used inverse pole figures (IPFs). IPFs

were calculated and plotted with generic mapping tools [34]. The input for plotting the IPFs was

based on Rietveld refinement of spectra from a single bank. Hence the approach enabled

following the texture evolution in the longitudinal as well as the transverse direction separately

depending on the detector bank used.

The full texture distribution was also examined by simultaneously using diffraction patterns recorded in both detectors of SMARTS and making an axisymmetric texture assumption. The assumption is valid considering that both the hot-drawing process and uniaxial loading are inherently axisymmetric. This second approach generated axial distribution plots, obtained by refining two banks of diffraction data simultaneously, to study the actual distribution of a particular crystallographic orientation, as shown in Fig. 3.3. These plots correspond to a radial slice through the pole figure and are applicable here because of the cylindrical symmetry in the sample. In an axial distribution plot, the y-axis is a measure of the number of grains (compared to a randomly oriented polycrystal) that are oriented at an angle between that normal to the chosen plane and the loading axis. Based on the above definition, a random polycrystalline sample would be represented by a horizontal line at unity in the plot, with typical values of 2-5 for moderate texture (*e.g.*, 70% rolled steel has an index of 3-4), 10-15 for a strong texture (*e.g.*, wire drawing) [35].

3.3 Single Peak Fitting

By fitting individual diffraction peaks, lattice strain and peak broadening with respect to a subset of grains of the same crystallographic orientation relative to the loading direction was determined. GSAS single peak fitting [36] uses a Gaussian line shape function convoluted with a known instrumental resolution function. A typical single peak fit output using SMARTS spectra is shown in Fig. 3.4. The strain, ε_{hkl}, for a plane, *hkl*, at a given stress or temperature was subsequently quantified by,

$$\varepsilon_{hkl} = \frac{d^{hkl} - d_0^{hkl}}{d_0^{hkl}}, \tag{3.4}$$

where d_0^{hkl} and d^{hkl} are the planar d-spacings in the initial and final conditions, respectively, corresponding to a stress or temperature change in the system.

Besides strain information, intensity and full width at half maximum (FWHM) of a diffraction peak was also quantified by performing peak fitting on a specific *hkl* reflection. By studying the evolution of the changes in the relative intensities of diffraction peaks in a particular phase, a qualitative means to follow the texture or preferred orientation evolution in that phase was also adopted. The FWHM information, on the other hand, provided information on the development of heterogeneous strain and/or changes in martensite variant size due to possible variant coalescence.

3.4 Figures
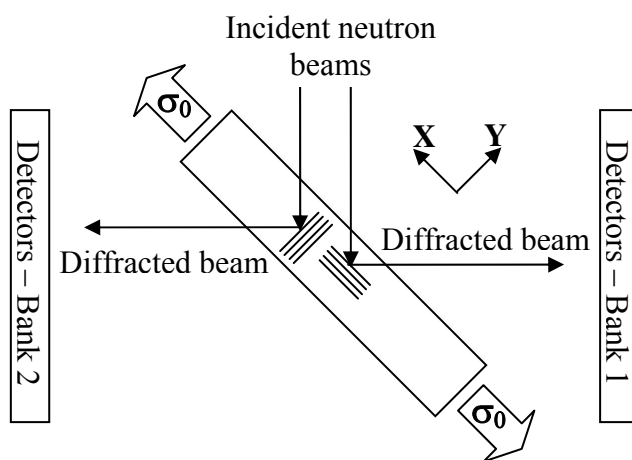
Figure 3.1 Schematic of the neutron diffraction setup at Los Alamos National Laboratory. The specimen can also be loaded in compression.
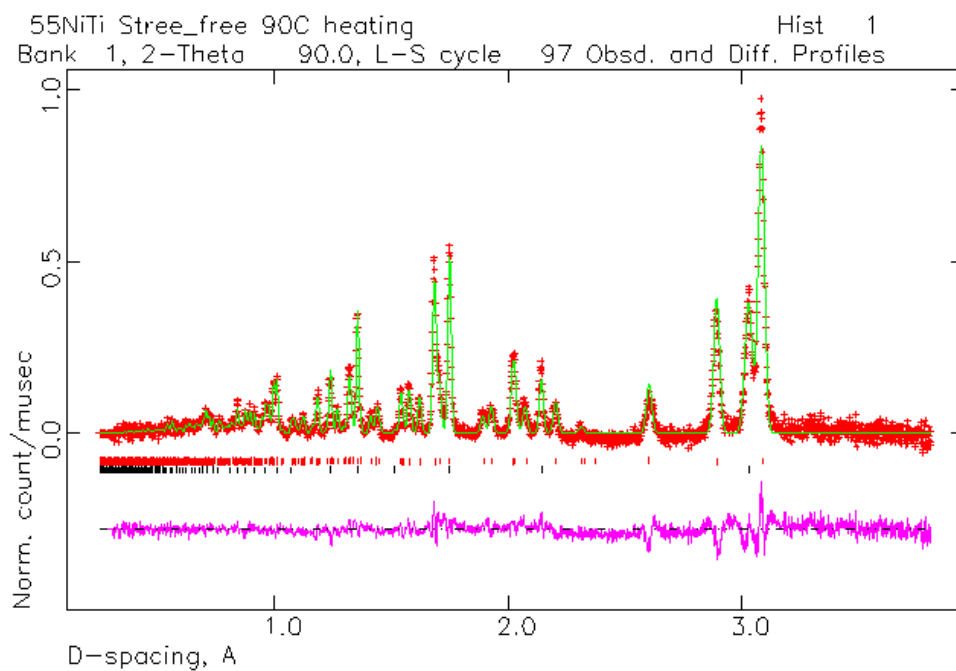
Figure 3.2 A sample Rietveld refinement output of a diffraction spectrum using GSAS
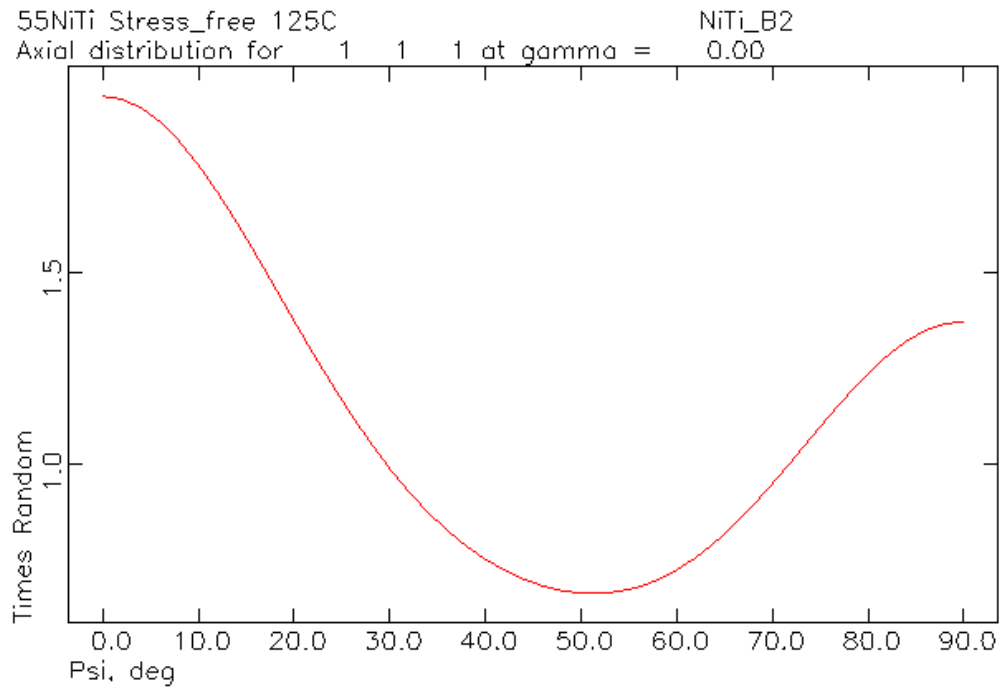
Figure 3.3 A representative axial distribution plot
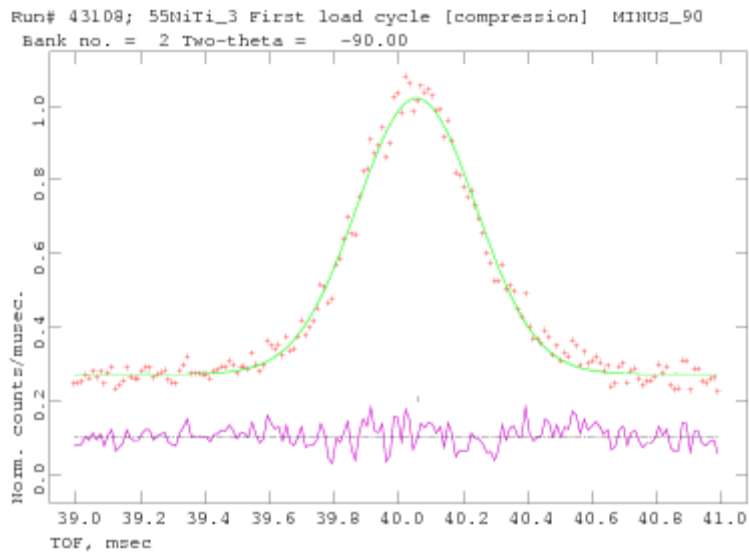
Figure 3.4 A representative single peak fit from SMARTS spectrum

CHAPTER FOUR: MEASUREMENT OF THE LATTICE PLANE STRAIN AND PHASE FRACTION EVOLUTION DURING HEATING AND COOLING IN NiTi SHAPE MEMORY ALLOYS

In this chapter, in situ neutron diffraction measurements that were performed during heating and cooling through the phase transformation in an unloaded sample of shape memory NiTi are described. The lattice plane specific strain evolution remains linear with temperature and is not influenced by intergranular stresses, enabling the determination of the thermal expansion tensor of B19' NiTi. The neutron measurements are consistent with macroscopic dilatometric measurements and a 30,000 grain polycrystalline self-consistent model. The accommodative nature of B19' NiTi results in macroscopic shape changes being offset (with temperature) from the start and finish of the transformation. The texture does not evolve in the absence of biasing stresses.

4.1 Introduction

A comprehensive understanding of the NiTi SMAs, especially in polycrystalline form, remains elusive due to the challenge of making direct connections between the lattice strain, phase volume fraction and texture evolution associated with the phase transformation at the atomistic scale, and macroscopically measurable properties such as transformation temperatures, work output, dimensional stability, thermal expansion, stress-strain and strain-temperature behaviors, *etc*. The objective of this work is to establish such connections by performing *in situ* neutron diffraction experiments to quantify the lattice strain, phase volume fraction and texture evolution as the *B19'* phase transforms to the *B2* phase during heating and transforms back during cooling.

Implicit in the nature of the diffraction technique is that it provides direct observation of the phase transformation, enabling comparison with commonly used indirect assessments of the phase transformation (*e.g.*, through differential scanning calorimetry (DSC), dilatometry or resistivity measurements) that determine one or more associated properties (*e.g.*, heat capacity, shape change or electrical resistance). The measurements are performed in a nominally unloaded sample or in the so-called free-recovery condition [37] with the objective of establishing baseline properties that are not influenced by externally applied stresses. Even though neutron diffraction has been successfully utilized to study bulk NiTi samples previously (*e.g.*, Refs. [36, 38-40]), no experiments have been done to quantitatively follow the phase transformation associated with shape memory behavior under free-recovery conditions. In addition to making these connections between atomic scale measurements (vis-à-vis neutron diffraction experiments) and macroscopic measurements (vis-à-vis strain-temperature experiments), this work is additionally motivated by a need to make available parametric and experimental input for various existing models of shape memory behavior (*e.g.*, Refs. [41-44]).

4.2 Experimental Procedures

Ten millimeter diameter rods of NiTi (nominal composition of 49.9 at.% Ni) were produced by Special Metals, New Hartford, NY, in the hot-rolled/hot-drawn and hot-straightened condition. The martensite finish (M_f), martensite start (M_s), austenite start (A_s) and austenite finish (A_f), were determined by DSC to be 46, 71, 86 and 109 ± 2 ºC, respectively. Cylindrical tensile specimens (5.08 mm in diameter and 15.24 mm in gauge length) were fabricated by a conventional turning operation using a CNC lathe. *In situ* neutron diffraction measurements were performed in "time-of-flight" mode on the Spectrometer for MAterials Research at Temperature

and Stress (SMARTS) at Los Alamos National Laboratory (LANL). Detailed information on the diffraction setup can be found elsewhere [25]. Optical microscopy showed an average grain size of 40 μm, which ensured that there were sufficient number of grains in the gauge and diffracting volumes for measurements representative of bulk polycrystalline behavior. Two heating/cooling cycles were done at a rate of 15 °C/min between 25 °C and 175 °C, with neutron spectra being acquired during the second cycle. The first cycle was performed to relieve residual stress resulting from machining and stabilize material behavior. The second cycle was interrupted at a total of 27 selected temperatures to record neutron spectra. At each temperature, a holding period of 5 min was used to allow for the sample to equilibrate, and 30 min to acquire neutron spectra of adequate statistical quality. The macroscopic strain was measured and reported from an extensometer (gauge length of 10 mm and strain accuracy of 3×10^{-4}) placed on the sample.

4.3 Results and Discussion

Fig. 4.1 shows sections of diffraction spectra acquired at selected temperatures during the heating/cooling cycle. Upon heating, the intensities of the peaks corresponding to 001 and 110 planes in the *B19′* phase decrease, while those corresponding to 100 planes in the *B2* phase increase concomitantly due to the transformation. Upon cooling, the reverse holds true. Thus the progression and complete reversibility of the phase transformation between *B19′* and *B2* phases is directly observed without any intermediate phases (*e.g.*, a trigonal *R*-phase). The hysteresis associated with the transformation [40] is also evident from qualitatively comparing the spectra acquired at 80 °C during heating and cooling, wherein the 001 *B19′* peak is seen during heating but not during cooling.

The Rietveld refinement technique [26], implemented in the LANL code General Structure Analysis System (GSAS) [28], was used to analyze the acquired neutron spectra. Fig. 4.2 shows the evolution with temperature of the macroscopic strain (obtained from extensometry) and volume percentage of *B19′* phase (quantified by refinement of the neutron spectra). A strain increase of about 0.03% was observed by comparing before and after the heating/cooling cycle at 20 °C, which is comparable to the measurement resolution and could be also due to the variant reorientation under even minimal residual stress through transformation. While a one to one correspondence between the two curves is observed, careful examination shows nascent *B2* phase being formed during heating with no detectable change in the macroscopic shape-change strain. The last *B19′* variants to transform to the *B2* phase also appear to not affect the macroscopic shape-change strain. A similar converse observation was made during cooling and additionally substantiated by qualitative examination of spectra close to the start and finish of the phase transformation during heating and cooling. For example, during heating, the extensometer first detected macroscopic strain changes associated with the *B2* phase at 92 °C. However, a neutron spectrum acquired at 80 °C already showed evidence of the *B2* phase. Similarly, at temperatures above 102 °C, no shape-change strains were measurable on the extensometer while the neutron spectrum at 110 °C showed about 5.5 vol.% of *B19′* phase. This difference can be attributed to the accommodative nature of the *B19′* phase, wherein the elastic, thermal and allotropic mismatch is minimized [35, 45] close to the finish of the forward transformation and the start of the reverse transformation (*i.e.*, when few *B2* grains exist in a matrix of *B19′* variants), and vice-versa during the start of the forward transformation and finish of the reverse transformation. Thus a technique based on macroscopic shape changes to determine the

25

transformation temperatures (*e.g.*, Ref. [37]) cannot precisely capture the start and finish of the transformation given the accommodative nature of the *B19′* phase.

Peak positions and interplanar spacings were determined by GSAS single peak fitting [36]. Strains in the respective phases were subsequently quantified from,

$$\varepsilon_{hkl} = \frac{d^{hkl} - d_0^{hkl}}{d_0^{hkl}},$$
(4.1)

where d_0^{hkl} is the planar d-spacing at an initial condition, and d^{hkl} is the planar d-spacing at the selected temperature. The value of d_0^{hkl} was arbitrarily measured for the *B19′* phase at 25 ℃ and for the *B2* phase at 175 °C. The choice of the reference temperatures is not significant since relative rather than absolute strains are considered in the analyses.

The solid symbols in Fig. 4.3(a) are strains determined using Eq. (4.1) along directions normal to various *B19′* planes. The respective strains with temperature during heating of the *B19′* phase and its subsequent transformation to the *B2* phase are only reported from planes corresponding to non-overlapping peaks in the neutron spectra to reduce error. We particularly note that the strains increase or decrease linearly with temperature despite being associated with varying volume percentages of the *B19′* phase (*i.e.*, from being 100% at 25 ℃ to 16% at 100 ℃). While the increase or decrease is attributed to anisotropy arising from crystal symmetry (or lack thereof), the linearity is attributed to the accommodative nature of the *B19′* phase and its ability to reorient/detwin and to selectively transform to the *B2* phase, thereby accommodating any associated intergranular stresses arising from either like *B19′* grains or *B2* grains [35, 45, 46]. A linear fit of data from a given lattice plane then corresponds to the thermal expansion in the

direction normal to that plane. For the 020, 111, 120, 001, 110, $11\bar{1}$, $10\bar{1}$ and $20\bar{1}$ planes

shown in Fig. 4.3(a), these values were determined to be 42.22, 36.75, 30.74, 26.62, 8.67, -17.06,

-25.29 and -49.48 (x10^{-6}/°C), respectively. Adapting from Ref. [47], the thermal expansion

tensor was determined from the aforementioned neutron measurements as outlined in the

following. For a monoclinic crystal, the thermal expansion A_r in a direction l is given by

$$A_r = l_T \alpha_{ij} l = \begin{pmatrix} l_1 & l_2 & l_3 \end{pmatrix} \begin{pmatrix} \alpha_{11} & 0 & \alpha_{13} \\ 0 & \alpha_{22} & 0 \\ \alpha_{13} & 0 & \alpha_{33} \end{pmatrix} \begin{pmatrix} l_1 \\ l_2 \\ l_3 \end{pmatrix}, \tag{4.2}$$

where α_{ij} is the thermal expansion tensor. In matrix notation,

$$A = \Theta \alpha \Rightarrow \begin{pmatrix} A_1 \\ A_2 \\ \vdots \\ A_n \end{pmatrix} = \begin{pmatrix} l_1^2 & l_2^2 & l_3^2 & 2l_1 l_3 \\ m_1^2 & m_2^2 & m_3^2 & 2m_1 m_3 \\ \vdots & \vdots & \vdots & \vdots \\ n_1^2 & n_2^2 & n_3^2 & 2n_1 n_3 \end{pmatrix} \begin{pmatrix} \alpha_{11} \\ \alpha_{22} \\ \alpha_{33} \\ \alpha_{13} \end{pmatrix}. \tag{4.3}$$

The lattice parameters required to account for non-orthogonality in the monoclinic structure were

determined to be $a = 0.467$ nm, $b = 0.414$ nm, $c = 0.291$ nm and $\beta = 97.55°$ from Rietveld

refinement of the neutron spectrum at 25 °C. Appendix A tabulates peak reflections

corresponding to the P112$_1$/m structure for martensite. Even though four values, A_1, A_2, A_3 and

A_4, were sufficient to determine α in Eq. (4.3) for the *B19′* phase, a least squares method was

adopted to obtain the best value according to

$$\alpha = (\Theta_T \Theta)^{-1} \Theta_T A. \tag{4.4}$$

The components of the thermal expansion tensor as determined using the procedure outlined

above are reported in Table 4.1. To highlight consistency between the neutron measurements and

the thermal expansion tensor determination, the components of the thermal expansion tensor in

Table 4.1 were used to determine the thermal expansion along directions for which lattice stains

were measured. The determination was done using Eq. (4.2) and the results are shown as solid lines in Fig. 4.3(a). The solid lines reasonably capture the thermal expansion anisotropy in the *B19′* phase, consistent with our assumption of intergranular stress relaxation, since four independent constants in the thermal expansion tensor were adequate to capture the lattice strain evolution with temperature when compared to thirteen independent constants in the elastic stiffness tensor that would otherwise additionally be required. A 30,000 grain self-consistent polycrystalline deformation model [48, 49] with elastic stiffness constants from *ab initio* calculations [50] and subsequent experimental validation [39] was also used to assess the role of intergranular stresses. The model prediction was substantially better with the measured values when the intergranular stresses were allowed to fully relax and the average coefficient of thermal expansion from this model (CTE†) is included in Table 4.1. The coordinate axes of the thermal expansion tensor were transformed to obtain principal coefficients of thermal expansion which are also reported in Table 4.1. These principal coefficients were further averaged to obtain an isotropic, volume-averaged value (CTE*) and reported in Table 4.1 along with values from extensometry (CTE) measured in this work. The results compare favorably and also agree with previously reported dilatometric values, *e.g.*, 8.1 x 10^{-6}/°C (heating) and 8.9 x 10^{-6}/°C (cooling) for the *B19′* phase [45]. Neutron spectra were also similarly analyzed for the *B2* phase during cooling. The lattice parameter in the cubic austenite structure was determined to be $a = 0.303\,\mathrm{nm}$ from Rietveld refinement of the neutron spectrum at 125 °C, and peak reflections corresponding to the Pm3m structure for austenite were tabulated in Appendix A as well. A notable difference is the fact that the inherent cubic symmetry of the *B2* phase results in $\alpha_{11} = \alpha_{22} = \alpha_{33}$ with all other components being zero in Eq. (4.2). Fig. 4.3(b) shows the strains determined using Eq. (4.1) along 100 , 110 , 111 , 210 , 211 and 311 directions in the *B2* phase with temperature. As

28

expected, given that there is only one independent constant in the thermal expansion tensor, there is no anisotropy in the lattice strain vs. temperature response and the data are indistinguishable within error. Again, this observed behavior is attributed to the ability of the *B19′* phase to accommodate intergranular strains in the *B2* phase during the transformation. The corresponding average values for the *B2* phase from neutron measurements and extensometry are reported in Table 4.1 and compare favorably. The values also compare favorably with previously reported macroscopic values, 12.6 x 10^{-6}/°C (heating) and 11.5 x 10^{-6}/°C (cooling), for the *B2* phase [45]. Table 4.1 also reports corresponding values for the *B19′* phase during cooling and the *B2* phase during heating. The values are consistent with those obtained from the *B19′* phase during heating and the *B2* phase during cooling and are not discussed here to avoid redundancy.

By recourse to a generalized spherical harmonic description of the preferred orientation or texture [29, 30] in the Rietveld refinement procedure, the texture evolution during heating and cooling in both *B19′* and *B2* phases was investigated by examining axial distribution plots. These plots are a radial slice of the corresponding pole figure and are used here because of the cylindrical symmetry in the sample geometry. Fig. 4.4 is the axial distribution plot for *B19′* 001. In this axial distribution plot, the y-axis is a measure of the number of grains (compared to a randomly oriented polycrystal) that are oriented at an angle (Φ) between that normal to the 001 plane and the sample's long axis. Thus, a random polycrystalline sample would be represented by a horizontal line at unity, with typical values of 2-5 for moderate texture (*e.g.*, 70% rolled steel has an index of 3-4), 10-15 for a strong texture (*e.g.*, wire drawing) [35]. In addition to showing the absence of strong starting texture (maximum value is close to 1.5) no significant evolution was observed in the texture during heating and cooling in Fig. 4.4. This lack of texture

evolution was also verified by examining spectra and considering normalized peak intensity ratios reported as a ratio of the peak intensity at a given temperature to that of the peak intensity at 25 ºC during heating and cooling. The lack of texture evolution is expected since there is neither external biasing stress (as in *e.g.*, Ref. [36]) nor intergranular stress during the transformation, and is consistent with the observed lattice strain evolution with temperature.

4.4 Conclusions

The implications of this work which quantitatively links the lattice strain and phase fraction evolution with macroscopic measurements during a shape memory transformation are now highlighted. The measured lattice strain vs. temperature response points to the fundamentally accommodative nature of the *B19'* phase during the transformation that seeks to minimize elastic, thermal and allotropic mismatch, and was additionally validated in this work using a 30,000 grain polycrystalline self-consistent model. From the thermal expansion tensor determined here, the thermal expansion anisotropy of the *B19'* monoclinic structure is now known. This quantitative determination of the direction dependent thermal strains is of value in deconvoluting and determining strains purely resulting from the phase transformation (as opposed to elastic and thermal strains). Furthermore, for high temperature shape memory alloys, *e.g.*, NiTiPt, where strains associated with the transformation can be smaller, the established methodology is important and can aid in identifying desirable textures, to obtain higher magnitude of strain changes during heating/cooling. Lastly, this work urges caution in establishing standards based on indirect measurements of the phase transformation (*e.g.*, ASTM F2082-03 [37]), given the offset between atomic scale activity and macroscopic behavior attributed to the accommodative

nature of the *B19'* phase – as observed in this work while directly comparing neutron spectra and

the dilatometric response during the phase transformation.

Table 4.1 Components of the thermal expansion tensor and coefficients of thermal expansion (CTE) determined from neutron spectra, extensometry and a self-consistent model (10^{-6}/°C) in *B19′* and *B2* NiTi during heating and cooling..

			Heating (10^{-6}/°C)	Cooling (10^{-6}/°C)
B19′ NiTi	Thermal expansion tensor components	α_{11}	-47.2	-30.8
		α_{22}	43.8	32.1
		α_{33}	22.7	27.3
		α_{31}	29.0	32.4
	CTE*		6.4	9.5
	CTE†		8.1	10.9
	CTE (extensometry)		10.3	9.0
B2 NiTi	CTE*		13.0	13.1
	CTE (extensometry)		12.4	12.3

*isotropic average †self-consistent model

32

4.6 Figures
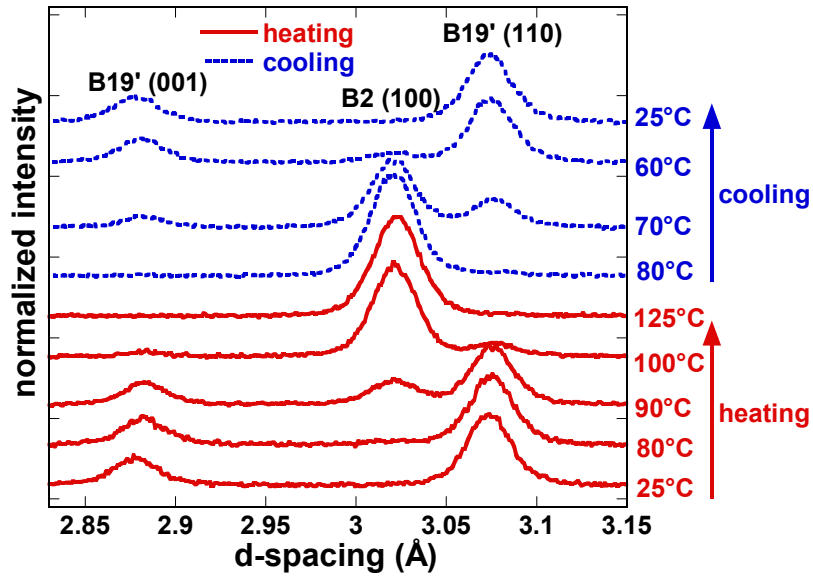
Figure 4.1 Section of neutron diffraction spectra acquired during heating and cooling. The spectra are normalized and displaced along the y-axis for clarity, and are shown here from lattice planes parallel to the length of the sample.
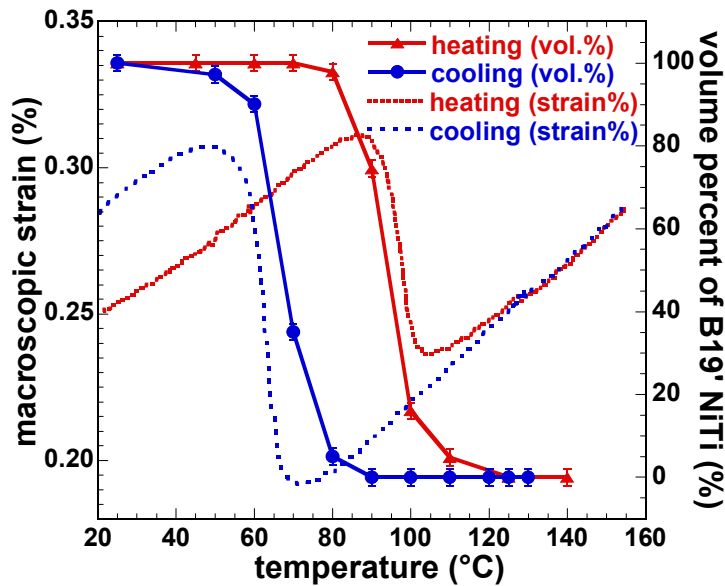
Figure 4.2 Evolution of macroscopic strain from extensometry (dotted lines) and volume percent of *B19'* phase from Rietveld refinement of neutron diffraction spectra (solid lines) with temperature.
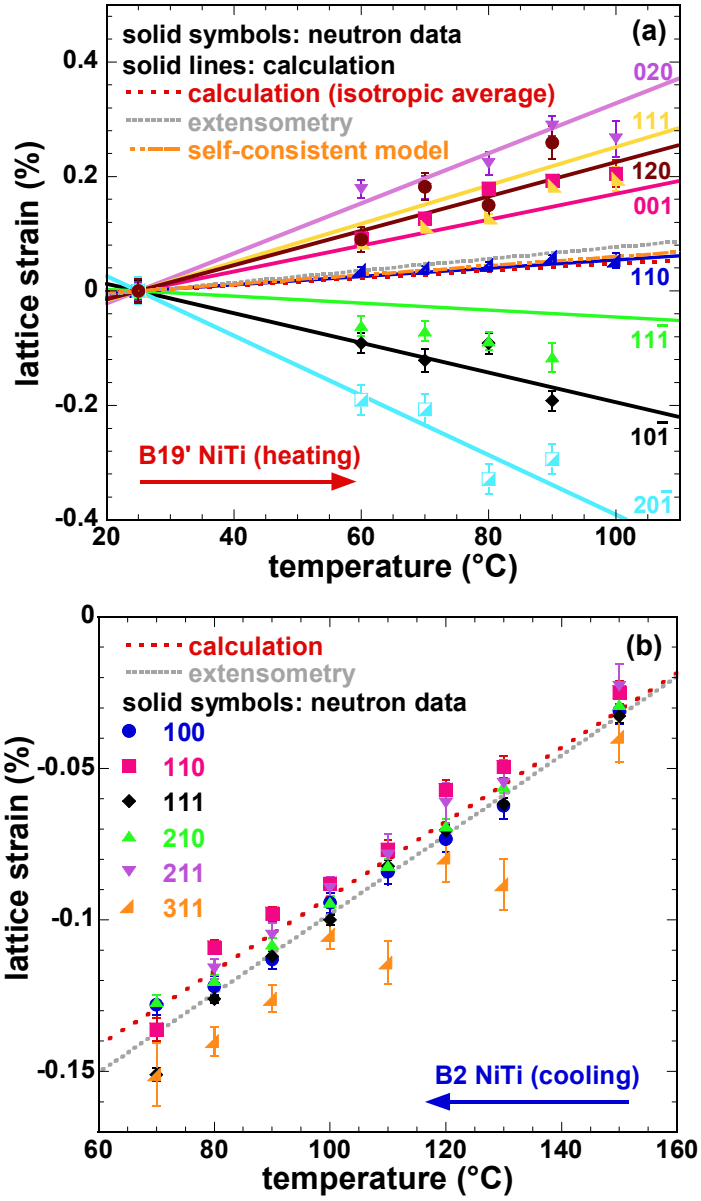
Figure 4.3 Lattice strain evolution as a function of temperature in (a) *B19'* NiTi during heating (b) *B2* NiTi during cooling. The data shown here are from lattice planes parallel to the length of the sample. The symbols are from neutron data and the lines are from the thermal expansion tensor determined in this work and macroscopic extensometry.
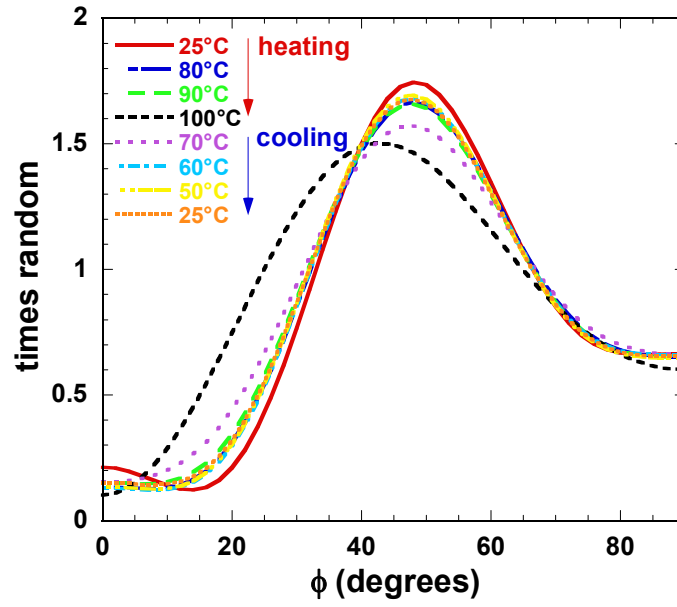
Figure 4.4 001 axial distribution plots for *B19′* NiTi during heating and cooling.

Appendix A:

The d-spacing of various *hkl* reflections of martensite in NiTi (no load, at 25 °C). The lattice

parameters are: $a = 0.291\,\text{nm}$, $b = 0.467\,\text{nm}$, $c = 0.414\,\text{nm}$ and $\gamma = 97.55°$.

H	K	L	Multiplicity	d-spacing (Å)
0	1	0	2	4.63037
0	1	1	4	3.08339
1	0	0	2	2.88584
-1	1	0	2	2.60829
1	0	1	4	2.36613
1	1	0	2	2.31593
0	2	0	2	2.31519
-1	1	1	4	2.20578
0	0	2	2	2.06652
1	1	1	4	2.02036
0	2	1	4	2.01987
-1	2	0	2	1.93461
0	1	2	4	1.88711
-1	2	1	4	1.75216
1	2	0	2	1.69982
1	0	2	4	1.68016
-1	1	2	4	1.61976
1	2	1	4	1.57206
0	3	0	2	1.54346
1	1	2	4	1.54192
0	2	2	4	1.5417
0	3	1	4	1.44592
2	0	0	2	1.44292
-1	3	0	2	1.44238
-2	1	0	2	1.43224
-1	2	2	4	1.41231
2	0	1	4	1.36229
-1	3	1	4	1.36183
-2	1	1	4	1.35329
2	1	0	2	1.32874
0	1	3	4	1.32047
1	2	2	4	1.31277
-2	2	0	2	1.30415
1	3	0	2	1.29204
2	1	1	4	1.26497
-2	2	1	4	1.2437
1	0	3	4	1.24327
0	3	2	4	1.23661
1	3	1	4	1.23319
-1	1	3	4	1.21819

1	1	3	4	1.18402
0	2	3	4	1.18392
2	0	2	4	1.18306
-1	3	2	4	1.18277
-2	1	2	4	1.17716
2	2	0	2	1.15796
0	4	0	2	1.15759
-2	3	0	2	1.13104
-1	4	0	2	1.12693
-1	2	3	4	1.12221
2	1	2	4	1.11764
2	2	1	4	1.11503
0	4	1	4	1.1147
-2	2	2	4	1.10289
1	3	2	4	1.09554
-2	3	1	4	1.09093
-1	4	1	4	1.08724
1	2	3	4	1.07029
0	0	4	2	1.03326
1	4	0	2	1.02856
0	3	3	4	1.0278
2	2	2	4	1.01018
0	4	2	4	1.00994
0	1	4	4	1.00846

The d-spacing of various *hkl* reflections of austenite in NiTi (no load, at 125 °C). The lattice parameter is: $a = 0.303\,\text{nm}$.

H	K	L	Multiplicity	d-spacing (Å)
1	0	0	6	3.03024
1	1	0	12	2.14271
1	1	1	8	1.74951
2	0	0	6	1.51512
2	1	0	24	1.35517
2	1	1	24	1.23709
2	2	0	12	1.07135
3	0	0	6	1.01008
2	2	1	24	1.01008
3	1	0	24	0.95825
3	1	1	24	0.91365
2	2	2	8	0.87476
3	2	0	24	0.84044
3	2	1	48	0.80987
4	0	0	6	0.75756
4	1	0	24	0.73494
3	2	2	24	0.73494
4	1	1	24	0.71424
3	3	0	12	0.71424
3	3	1	24	0.69519
4	2	0	24	0.67758
4	2	1	48	0.66125
3	3	2	24	0.64605
4	2	2	24	0.61855
5	0	0	6	0.60605
4	3	0	24	0.60605

CHAPTER FIVE: ON ELASTIC MODULI AND ELASTIC ANISOTROPY IN POLYCRYSTALLINE MARTENSITIC NɪTɪ

This chapter provides insight into the elastic response of B19' martensitic NiTi variants as they exist in bulk, polycrystalline aggregate form during monotonic tensile and compressive loading. The experimental effort centered on using in situ neutron diffraction during loading and the computational effort centered on using a 30,000 variant self-consistent polycrystalline deformation model. The neutron diffraction experiments were used to measure elastic moduli in several directions along with an average Young's modulus and a Poisson's ratio. The measurements were compared with predictions from the self-consistent model that accounted for the elastic intergranular constraint, and also with predictions of single crystal behavior from previously published ab initio studies. Variant conversion and detwinning processes that influenced the intergranular constraint occurred even at stresses where the macroscopic stress-strain response appeared linear and direct evidence of changes in texture were captured in inverse pole figures constructed from the neutron diffraction measurements.

5.1 Introduction

The macroscopic recoverable strain associated with the shape memory behavior in polycrystalline NiTi alloys can be expected to depend on individual cubic austenite grains and monoclinic martensite variants that are subjected to various compatibility and minimization conditions. An understanding of various contributing factors to the macroscopic recoverable strain is important in optimizing the thermomechanical response of existing polycrystalline

alloys as well as in engineering new alloys with ternary and quaternary elemental additions for use at elevated or low temperatures. The strain associated with a shape memory alloy in an actuator application typically has thermal, elastic and inelastic contributions. The thermal strains arise from thermal expansion and can be captured for an isolated austenite grain or martensite variant through the coefficient of thermal expansion tensor. Similarly, the elastic strain can be captured through the elastic stiffness tensor. The inelastic strains on the other hand primarily arise from phase transformation, variant reorientation/conversion and detwinning, and can be captured by examining the crystallographic relationship between the austenite and martensite phases as well as the crystallography of martensite. The inelastic strain can also have additional contributions from a retained or residual phase (almost always martensite) that nominally would have been expected to transform, and in some cases, may even include contributions from dislocation based plasticity. Despite the thermal and elastic strain contributions being smaller in magnitude than strains arising from the aforementioned inelastic contributions, they affect the overall thermomechanical response by modifying the stress state. This influence is enhanced further by the anisotropic nature of these contributions. These anisotropic thermal and elastic strains also dictate the texture development where small differences in strain can result in an entirely different selection of preferred variants (*e.g.,* that either result in a small net compressive strain or a small net tensile strain in the analyses presented in Ref. [51]). Furthermore, in shape memory alloys for elevated temperature applications where recoverable strains are smaller in order to maintain dimensional stability in the system, the elastic and thermal contributions cannot be ignored in the design and implementation of shape memory actuators.

Despite the value in assessing and understanding the thermal and elastic strain contributions to the overall thermomechanical response of shape memory alloys, several modeling efforts that have sought to capture the overall polycrystalline response of NiTi, have not rigorously considered the thermal and elastic properties of individual NiTi crystals. This is particularly true of *B19′* martensitic NiTi and can be attributed to a lack of experimental data given the difficulty in obtaining good quality single crystals. In a previous complementary publication, the authors have determined the coefficient of thermal expansion tensor for *B19′* martensitic NiTi and assessed the thermal strain anisotropy during heating and cooling [52]. Connections were also made between the single crystal coefficient of thermal expansion tensor and the average dilatometric response from polycrystalline *B19′* martensitic NiTi.

The objective of this work is to provide insight into the elastic response of *B19′* martensitic NiTi variants as they exist in bulk, polycrystalline aggregate form during monotonic loading. Emphasis is placed on capturing and quantifying the strain anisotropy which arises from the symmetry of monoclinic martensite (*i.e.,* the thirteen stiffness or compliance tensorial elements) and internal stresses that are influenced by intergranular constraints between individual martensite variants and load re-distribution among variants as the texture evolves due to variant reorientation and detwinning. Both tensile and compressive loading are considered given the existing asymmetric variant reorientation and detwinning response. The methodology adopted in this paper is both experimental and computational. The experimental effort centers on using neutron diffraction during loading. The technique allows for texture and atomic scale, volume-averaged mechanical characterization of grain sub-sets within bulk, polycrystalline aggregates. The computational effort centers on a 30,000 variant self-consistent polycrystalline deformation

model to predict the anisotropic elastic response of *B19′* NiTi based on recently reported elastic stiffness constants from *ab initio* calculations [50] and make comparisons with the neutron diffraction experiments. The modeling effort additionally assesses the role of variant-scale intergranular stresses in the consolidated polycrystalline bulk response. As done previously for the case of thermal strains [52], connections are also made between the elastic properties of martensitic NiTi single crystals (*i.e.,* the single crystal stiffness tensor) and the overall macroscopic response in bulk polycrystalline form. Thus, by comparing results from neutron diffraction experiments, macroscopic extensometry measurements, a self-consistent model and a previously published *ab initio* determination of the stiffness tensor for *B19′* martensitic NiTi, this work quantifies the internal elastic strain evolution during loading in polycrystalline *B19′* martensitic NiTi that is influenced by crystalline symmetry (or lack thereof), intergranular interaction and constraints, and strain re-distribution among variants due to variant reorientation and detwinning.

5.2 Experimental and Computational Procedures

5.2.1 Material

Ten millimeter diameter rods of NiTi (nominal composition 49.9 at.% Ni) were produced by Special Metals, New Hartford, NY, in the hot-rolled/hot-drawn and hot-straightened condition. Cylindrical tensile specimens (5.08 mm in diameter and 15.24 mm in gauge length) with threaded ends were fabricated by a conventional turning operation using a CNC lathe. The characteristic phase transformation temperatures, martensite finish (M_f), martensite start (M_s), austenite start (A_s) and austenite finish (A_f) were determined by differential scanning calorimetry to be 46, 71, 86 and 109 ± 2 °C, respectively. No intermediate phase, *e.g.,* R-phase, or multi-

stage transformation was observed. Optical microscopy showed an average grain size of 40 μm in the alloy.

5.2.2 Neutron Diffraction during Mechanical Loading

In situ neutron diffraction measurements during loading were performed in "time-of-flight" mode on the Spectrometer for MAterials Research at Temperature and Stress (SMARTS) at Los Alamos National Laboratory (LANL). Samples were separately tested in tension and compression at selected stresses at room temperature while neutron diffraction spectra were simultaneously acquired. Neutron spectra were obtained at compressive stresses of 0.5 (nominally unloaded), 100, 200, 300, 324, 357 and 450 MPa, and tensile stresses of 0.5 (nominally unloaded), 100, 200, 233, 252, 269, 375 and 450 MPa. The ramp rate was 0.075 mm/min and at each stress the corresponding neutron diffraction spectrum was acquired for about 30 min to ensure adequate statistical quality for analysis. The macroscopic strain was measured and reported from an extensometer placed on the sample (gauge length of 10 mm and strain resolution of 5×10^{-5}).

5.2.3 Self-Consistent Modeling

A 30,000 variant self-consistent polycrystalline deformation model [48, 49] was used to predict the anisotropic elastic response of *B19′* martensitic NiTi. The model used recently reported stiffness constants from first-principles calculations [50] as input and treated each variant as an ellipsoidal inclusion embedded in a homogeneous effective medium according to Eshelby theory [53, 54]. The overall response of the polycrystal and individual variants was determined in a self-

consistent manner by accounting for the elastic anisotropy of individual variants and the existing polycrystalline constraint. The numerical implementation of the formulation is described in detail in Refs. [48, 49]

5.3 Results and Discussion

5.3.1 Lattice Parameters and Initial Texture

Fig. 5.1 shows results of the Rietveld refinement procedure of spectra acquired from the NiTi sample at room temperature in the nominally unloaded condition. Spectra corresponding to diffracting lattice planes perpendicular to the cylindrical axis of the sample (*i.e.,* with plane normals along the long axis of the sample) and parallel to the cylindrical axis of the sample are shown and are incorporated together in the Rietveld refinement procedure. The best fit obtained for *B19'* martensite corresponded to the $P112_1/m$ structure with the following lattice parameters: a = 2.9131 Å, b = 4.6770 Å, c = 4.1299 Å and γ = 97.790°, with relative uncertainty of roughly 1 x 10^{-4} Å. We note that from the two commonly adopted conventions for describing the monoclinic unit cell [47], we chose the *c* axis as the diad axis and γ as the non-orthogonal angle. As expected from the processing history of the alloy used (*i.e.,* absence of cold work), the starting texture or preferred orientation of variants was weak and was determined to have a texture index of 1.14 (1 corresponding to a random polycrystalline sample). The texture index was obtained by integrating the orientation distribution function, which maps the probability of each of the possible variant orientations with respect to the external sample dimensions, over all space [30, 55]. In a subsequent section, IPFs of the sample in this nominally unloaded condition are presented and analyzed with other IPFs in the context of examining the texture evolution

44

with loading. We note that a weak starting texture was desired in this work in order to assess the role of variant reorientation and detwinning on the elastic strain anisotropy and hence a sample with strong starting texture was not selected.

5.3.2 Young's and Volume Averaged Elastic Moduli

Fig. 5.2 is the macroscopic stress-strain response during uniaxial tensile and compressive loading from the two specimens used, with the solid symbols indicating stresses at which neutron spectra were acquired. For both compressive and tensile loading, the initial response is macroscopically linear to the same stress and can be attributed to mostly elastic deformation of the *B19'* martensite. At higher stresses, the deformation is dominated by variant reorientation and detwinning that manifests as non-linearity in the macroscopic stress-strain response. Recognizing from previous work [39] that variant reorientation and detwinning occurs at low stresses even when the macroscopic stress-strain response appears to be linear, we obtain a Young's modulus of 50.4 ± 3 GPa from the observed stress-strain response from both specimens. The onset of macroscopic non-linearity was established to be at 210.1 ± 4 MPa in both specimens using a 0.2% strain offset criterion. No differences in the apparent Young's modulus or the macroscopic onset of variant reorientation and detwinning are expected given that the specimen initially comprises of mostly randomly oriented grains with very little texture. Following variant reorientation and detwinning, the texture in terms of the *B19'* martensite variants evolves differently in tension and compression resulting in differences between the slope of the stress-strain response in tension and compression as observed in Fig. 5.2.

Rietveld refinement of neutron spectra can be used to obtain a volume averaged strain in polycrystalline samples. This approach has previously been shown to track the lattice plane or direction specific strains in superelastic NiTi [56], steel [33] and beryllium [57]. The strain in a direction perpendicular to a given *hkl* plane, ε_{hkl}, can be formulated as having isotropic and anisotropic contributions. In *B19'* martensite, the isotropic strain contribution can be captured by fitting all peaks in the neutron spectra according to $\frac{\Delta a}{a} = \frac{\Delta b}{b} = \frac{\Delta c}{c}$ where a, b and c are the lattice parameters. The anisotropic strain contribution can be captured by fitting peaks depending on the orientation of their plane normals relative to a chosen axis. Here for the case of *B19'* martensite, the c-axis was the chosen axis and a cosine dependence was used. Thus

$$\varepsilon_{hkl} = \varepsilon_{isotropic} + \varepsilon_{anisotropic} = \frac{\alpha}{C} + \frac{\beta \cos\phi}{C}, \tag{5.1}$$

where α and β are the Rietveld fitting parameters, C is the diffractometer constant used to convert time-of-flight neutron data to d-spacing and ϕ is the angle between the *hkl* plane normal and the *c* axis. Based on the formulation of strain in Eq. (5.1), by setting β to zero, volume averaged isotropic strains in a direction along the loading axis were determined at stresses below 210 MPa for which neutron spectra were available (see Fig. 5.2). The corresponding applied stress was divided by the strains thus obtained to give an average modulus of 134 ± 4 GPa. The value for the modulus compared well with a recently reported average modulus value of 122.3 GPa from *ab initio* studies [50] and a previously reported modulus value of 101 GPa from nano-indentation [39]. Here we note that these values are considerably higher than values commonly used for *B19'* NiTi (*e.g.*, 20-50 GPa, [39]) and as previously presented the discrepancy is attributed to variant reorientation and detwinning at low stresses.

5.3.3 Direction and Lattice Plane Specific Elastic Moduli

Fig. 5.3 through Fig. 5.6 show the applied stress - lattice strain response in *B19'* martensite as determined from single peak fits of individual lattice plane reflections in the neutron spectra. The strain, ε_{hkl}, for a particular plane, *hkl*, at a given applied stress is reported from,

$$\varepsilon_{hkl} = \frac{d^{hkl} - d_0^{hkl}}{d_0^{hkl}}, \tag{5.2}$$

where d_0^{hkl} is the planar d-spacing in the nominally unloaded condition (0.5 MPa in this experiment) and d^{hkl} is the planar d-spacing at the given applied stress. The data shown here are from diffracting lattice planes perpendicular to the cylindrical or loading axis of the sample (*i.e.,* with plane normals along the long or loading axis of the sample). We note that given the diffraction geometry with fixed detectors and a polychromatic neutron source, the data reported in these figures are from diffracting planes in individual variants that are oriented so as to satisfy the Bragg condition (*i.e.,* variants with diffracting lattice planes perpendicular to the loading direction.) These diffracting variants are a subset of all variants, homogeneously distributed and each surrounded by twin related or differently oriented variants in the diffracting volume (approx. 100 mm³). Hence the strain, ε_{hkl}, is the average strain in a direction normal to the *hkl* plane and is measured in all variants (in the diffracting volume) that are oriented with their *hkl* plane normals along the loading axis. The strains presented in the aforementioned figures include error bars associated with the statistics of fitting the peak reflections in the neutron spectra and are only shown for those planes and directions with reduced error (*e.g.,* overlapping peaks are not reported). We note that data corresponding to the maximum stress of 450 MPa is not available for all orientations in these figures, since the texture evolution with increasing stress orients diffracting planes away from the detector bank from which the neutron data is presented. Thus

there are no symbols indicating lattice strains up to 450 MPa from certain planes, *e.g.,* 100, 012, 102 in Fig. 5.3 and 121 in Fig. 5.4.

For each *hkl* plane represented in Fig. 5.3 through Fig. 5.6, two sets of lines are also shown. The first line (dashed), for a given *hkl* plane, represents the elastic modulus E_{hkl} in a direction normal to that *hkl* plane in a martensite variant as determined from,

$$\frac{1}{E_{hkl}} = l_1^4 S_{11} + 2l_1^2 l_2^2 S_{12} + 2l_1^2 l_3^2 S_{13} + 2l_1^3 l_3 S_{15} + l_2^4 S_{22} + 2l_2^2 l_3^2 S_{23} + 2l_1 l_2^2 l_3 S_{25}$$
$$+ l_3^4 S_{33} + 2l_1 l_3^3 S_{35} + l_2^2 l_3^2 S_{44} + 2l_1 l_2^2 l_3 S_{46} + l_1^2 l_3^2 S_{55} + l_1^2 l_2^2 S_{66} \tag{5.3}$$

where S_{ij} is the single crystal compliance tensor in collapsed matrix notation and l_1, l_2 and l_3 are the direction cosines in the direction normal to the *hkl* plane [47]. For *B19′* martensite, S_{ij} has thirteen independent constants and the values used here were obtained from Ref. [50]. The second line (solid), for a given *hkl* plane, is the equivalent elastic modulus from the self-consistent model previously described. Two horizontal dotted lines at ± 210.1 MPa are also shown to guide the eye in determining the onset of macroscopic non-linearity (corresponding to large-scale variant reorientation and/or detwinning) in the stress-strain response in Fig. 5.2. Recognizing that the texture evolution following variant reorientation and detwinning in tension and compression are different, Fig. 5.3 through Fig. 5.6 combine data from specimens loaded in tension and compression in order to assess the effect of texture evolution on the strain evolution as a result of variant reorientation and/or detwinning. This combined representation is adopted since it facilitates the easy identification of asymmetry in the stress-stress response in variants in tension and compression that arise due to differences in variant reorientation and detwinning in tension and compression.

From the neutron diffraction data presented in Fig. 5.3 through Fig. 5.6 (symbols), elastic moduli

in directions normal to given *hkl* planes were also determined from linear fits of data obtained in

the initial loading region in tension and compression. These moduli from the neutron

measurements ($E_{hkl}^{neutron}$) are reported in Table 5.1. A total of 5 or 6 points (specified in Table 5.1)

were used for each fit and the smallest linearity correlation coefficient among the various linear

fits (also specified in Table 5.1) was 0.978. Also included in Table 5.1 are values from the *ab*

initio predictions from Ref. [50] using Eq. (5.3) ($E_{hkl}^{crystal}$), results from the self-consistent model

(E_{hkl}^{model}) and error percentages, both, between the *ab initio* predictions using Eq. (5.3) and the

neutron measurement $\left(\dfrac{E_{hkl}^{crystal} - E_{hkl}^{neutron}}{E_{hkl}^{neutron}} \right)$, and between the self-consistent model and the neutron

measurements $\left(\dfrac{E_{hkl}^{model} - E_{hkl}^{neutron}}{E_{hkl}^{neutron}} \right)$. An anisotropic elastic response was observed in the neutron

measurements for the *B19′* martensite phase, with a maximum modulus of 167.1 GPa in the

direction normal to the 102 plane and a minimum modulus of 78.2 GPa in the direction normal to

the -110 plane. There was reasonable agreement (less than 10% error) between the *ab initio*

predictions from Eq. (5.3) and the moduli from neutron diffraction in directions perpendicular to

100, 012, 102, -112 and -122 planes. The agreement between the neutron diffraction

measurements in directions perpendicular to the 100, 012 and -120 planes and results from the

self-consistent model was even better (less than 5% error). The main difference between using

Eq. (5.3) and the self-consistent model predictions is that the former approach applies to single

crystals and thereby implicitly ignores the intergranular constraint that arises in polycrystalline

samples. The self-consistent approach on the other hand accounts for the elastic intergranular

constraint as an individual grain (variant in this case) is surrounded by other grains (twin related

or non-twin related variants in this case). This then implies that in directions perpendicular to

100, 012, -120, 121, 011, -121 and -110 planes in *B19′* martensite, or more generally in variants

oriented with their 100, 012, -120, 121, 011, -121 and -110 planes perpendicular to the loading

direction in polycrystalline *B19′* martensite, the role of intergranular constraint is significant

since there is better agreement between the neutron diffraction measurements and the predictions

from the self-consistent model than there is between the neutron diffraction measurements and

those from Eq. (5.3). However, there is still substantial disagreement (errors greater than 20%)

between the self-consistent model predictions and the neutron measurements in directions

perpendicular to -122, -111, 011, -121 and -110 planes. As previously indicated, the strains

determined from Eq. (5.2) represent strains in variants that are homogenously distributed

throughout the diffracting volume. Thus the moduli obtained from the neutron diffraction data

implicitly include the effects of intergranular constraint. The intergranular constraint arises from

the neighboring variants immediately surrounding the diffracting variants due to the

polycrystalline nature of the sample. While the elastic intergranular constraint is considered in

the self-consistent model, the inelastic contributions are not. These inelastic contributions result

in load partitioning of the applied stress as a result of the variant undergoing reorientation or

conversion or as a result of possible detwinning in a variant that is surrounded by a twin related

variant. The effect of these inelastic contributions at higher stresses can be seen in Fig. 5.6

wherein the neutron data corresponding to 011, -121 and -110 planes are presented. In this figure,

at stresses above 210 MPa (corresponding to the onset of macroscopic detwinning), the stress-

strain response from the neutron measurements tracks the stress-strain predictions from the *ab*

initio calculations using Eq. (5.3) more closely (*i.e.,* the slope of the stress-strain response of the

symbols above 210 MPa follow the corresponding dashed lines). A similar case can be made for

the -120 planes in Fig. 5.4. However in this case, the inelastic contributions though evident at stresses above 210 MPa do not influence the comparison between moduli in the elastic region of the macroscopic response (since an error of less of 5% was observed). We note that load partitioning resulting from variant reorientation and detwinning can also increase the intergranular constraint leading to stiffening in the observed stress-strain response as seen in compression in a direction perpendicular to the -112 plane in Fig. 5.4 and the -122 and -111 planes in Fig 5.5. This general behavior wherein there is a change in slope in the stress-strain response in neutron data obtained at higher stresses due to variant conversion and detwinning is analogous to strain redistribution associated with stress-induced transformations in superelastic NiTi [36], plasticity in face-centered cubic austenitic steel [33], aluminum and copper [58], and twinning in hexagonal close packed beryllium [59] and orthorhombic uranium [57].

Thus when variant conversion and detwinning relax most of the intergranular constraint arising from the neighboring variants, the moduli from neutron measurements compares well with the predictions from Eq. (5.3) that consider single crystals implicitly without any intergranular constraint. Previously, it has been shown that detwinning occurs at stresses as low as 66 MPa in *B19′* martensitic NiTi [39]. More evidence of this variant conversion and detwinning, based upon the observed texture evolution, is present in the next section.

5.3.4 Texture Evolution

Fig. 5.7 shows IPFs for the longitudinal direction (*i.e.,* plane normals along the loading axis) in *B19′* martensite loaded in tension while Fig. 5.8 shows IPFs for the transverse direction (*i.e.,* plane normals perpendicular to the loading axis). Fig. 5.9 and Fig. 5.10 are the corresponding

figures obtained during compressive loading. The first IPF in each of these figures are enlarged and identify the diffracting *hkl* poles (normals to the diffracting *hkl* planes) [60]. The IPFs show the distribution of a selected direction in the specimen relative to the crystal axes. Thus the numbers at the top left hand corner of each IPF indicate the respective maximum and minimum densities of grains with the given pole along the given sample direction, in multiples of random distribution (1 corresponding to a random distribution). For clarity in illustration, each figure adopts a unique scale given the differences in the strengths of texture (*e.g.,* 0 to 7.25 in Fig. 5.7 and 0 to 2.8 in Fig. 5.8). Fig. 5.7 shows a maximum intensity of 1.86 (times random) near the 001 pole, which is consistent with the weak texture index of 1.14 determined in the previous section.

The purpose of presenting Fig. 5.7 through Fig. 5.10 here is to show direct experimental evidence of variant reorientation and detwinning that influence the intergranular constraint thereby affecting the moduli discussed in the preceding section. As an example, we examine the case of moduli measured by neutron diffraction in a direction perpendicular to the 011 plane. The modulus measured in this work is 117.1 GPa and compared well with moduli similarly measured in previously reported work (122 GPa in compression and 113 GPa in tension) [39]. However, the modulus from the *ab initio* calculation using Eq. (5.3) predicted a modulus of 175.9 GPa and that from the self-consistent model a modulus of 155.7 GPa. From Fig. 5.8 which shows IPFs from diffracting planes (in tension) parallel to the loading direction, the intensity at the 011 orientation decreases as follows with increasing stress: 0.9493 (0 MPa), 0.9465 (100 MPa), 0.9195 (200 MPa). This behavior would also be expected in compression when a direction perpendicular to the loading direction is considered (albeit with different intensities since the

sense of the stress is the same due to a Poisson expansion but the magnitude is not). This expected behavior is observed in Fig. 5.9 where the intensity at the 011 orientation decreases as follows with increasing stress: 0.4431 (0 MPa), 0.4522 (-100 MPa), 0.4320 (-200 MPa). We emphasize that these changes occur at stresses below 210 MPa where the macroscopic stress strain response is mostly linear. As a result of these observed changes in texture the modulus measured by neutron diffraction in a direction perpendicular to the 011 plane is even lower than the self-consistent model predictions which cannot account for relaxation in intergranular constraint due to these changes in texture. The intensity at the 011 orientation continued to decrease as follows with increasing stress in Fig. 5.8: 0.8954 (233 MPa), 0.7501 (252 MPa), 0.7088 (269 MPa), 0.5630 (375 MPa) and 0.4743 (450 MPa) and as follows with increasing stress in Fig. 5.9: 0.3545 (-300 MPa), 0.3179 (-324 MPa), 0.2559 (-357 MPa), and 0.1869 (-450 MPa). We note comparable behavior in other directions reported in Table 5.1 and in Fig. 5.3 through Fig. 5.10 but caution that the quantitative connection between texture evolution, intergranular constraint and elastic moduli is not straight forward given the accommodative nature of martensite.

5.3.5 Poisson's Ratios

In section 5.3.2, an average elastic modulus was determined in a direction along the applied load by selecting neutron spectra from the bank of detectors that contained information from diffracting planes perpendicular to the loading direction. The same procedure was repeated in a direction perpendicular to the applied load by considering diffracting planes parallel to the loading direction and the resulting modulus was divided to obtain a Poisson's ratio. A value of

0.387 ± 0.030 was obtained and compared well with the theoretical value of 0.36 predicted in Ref. [50].

The concept of a generally defined Poisson's ratio is extended to the case of the non-orthogonal *B19′* NiTi monoclinic lattice in order to make comparisons between the neutron measurements and the stiffness tensor reported in Ref. [50] as outlined in the following. The approach adopted was motivated by considering two mutually perpendicular planes, $h_1k_1l_1$ and $h_2k_2l_2$, within the same variant in the *B19′* lattice where $h_1k_1l_1$ is perpendicular and $h_2k_2l_2$ is parallel to the loading direction. When these two sets of planes satisfy the Bragg diffraction condition, strains can be obtained in directions normal to these planes from the two banks of detectors used on SMARTS. Thus a diffraction Poisson's ratio ν can be defined as a ratio of strains in which $\varepsilon_\perp$ and $\varepsilon_{//}$ are the strains perpendicular (from $h_2k_2l_2$ planes) and parallel (from $h_1k_1l_1$ planes) to the loading direction, respectively. Among the eleven planes previously presented in this study, the 012 (representing $h_1k_1l_1$) and 100 (representing $h_2k_2l_2$) planes were chosen. The angle between these two planes is 87° and approximately satisfies the requirement that the planes be mutually perpendicular in the same variant. Additionally these planes are not influenced by intergranular constraints as seen by the agreement between moduli from neutron diffraction, *ab initio* calculations from Eq. (5.3) and the self-consistent model (Table 5.1). Thus the Poisson's ratio ν defined is

$$\nu = -\frac{\varepsilon_\perp^{h_2k_2l_2}}{\varepsilon_{//}^{h_1k_1l_1}} = -\frac{\varepsilon_{100}}{\varepsilon_{012}} \tag{5.4}$$

We recognize from the scattering geometry that while certain variants can satisfy the Bragg condition and diffract resulting in peak reflections that help determine both $\varepsilon_\perp$ and $\varepsilon_{//}$, other variants can satisfy the Bragg condition and diffract resulting in peak reflections that help

determine either $\varepsilon_\perp$ or $\varepsilon_{//}$. However in the later case given that the planes chosen are not substantially influenced by intergranular stresses we expect the contribution to represent the average matrix behavior (because of the random sampling of variants in the diffraction volume) that is dominated by anisotropy arising from the crystal symmetry. This reasoning makes possible a comparison between the aforementioned diffraction Poisson's ratio and a value determined from the stiffness tensor reported in Ref. [50]. In Eq. (5.4), ε_{012} per unit stress is the reciprocal of the elastic modulus in a direction perpendicular to the 012 plane when the plane is oriented perpendicular to the loading direction. By using a value of 145.4 GPa from Table 5.1, a value of 6.878×10^{-12} Pa^{-1} was obtained for ε_{012} per unit stress. ε_{100} per unit stress is the reciprocal of the elastic modulus in a direction perpendicular to the 100 plane but when the 100 plane is oriented parallel to the loading direction. This modulus was determined to be 323.1 GPa from fitting the stress-strain response from the appropriate detector bank resulting in a value of 3.095×10^{-12} Pa^{-1} for ε_{100} per unit stress. A value of 0.45 was thus obtained for the Poisson's ratio defined in Eq. (5.4).

In order to make comparisons with the equivalent Poisson's ratio from Ref. [50], the corresponding ε_{012} per unit stress in Eq. (5.4) was determined to be 7.353×10^{-12} Pa^{-1}, by using a value of 136.0 GPa from Table 5.1. The determination of ε_{100} per unit stress has to account for the non-orthogonal nature of the *B19'* lattice and is presented as follows.

An orthogonal α-β-γ coordinate system is defined relative to the diffracting monoclinic variant under consideration as shown in Fig. 5.11. The objective is to determine a normal strain in the γ direction when a uniaxial stress σ is applied in the β direction normal to the *HKL* plane. The

HKL indices in this variant are obtained from *hkl* indices in the non-orthogonal monoclinic unit cell. A uniaxial stress σ applied in the β direction normal to the *HKL* plane results in the following stress tensor in the α-β-γ coordinate system:

$$\sigma_{ij}^{\alpha\beta\gamma} = \begin{pmatrix} 0 & 0 & 0 \\ 0 & \sigma & 0 \\ 0 & 0 & 0 \end{pmatrix} \tag{5.5}$$

This stress tensor is transformed into the original x-y-z coordinate system with the following axes (unit vectors):

$$x = \begin{bmatrix} 1 & 0 & 0 \end{bmatrix}, \, y = \begin{bmatrix} 0 & 1 & 0 \end{bmatrix}, \, z = \begin{bmatrix} 0 & 0 & 1 \end{bmatrix} \tag{5.6}$$

The axes (unit vectors) in the α-β-γ coordinate system are:

$$\alpha = \frac{1}{\sqrt{l^2 + h^2}} \begin{bmatrix} -l & 0 & h \end{bmatrix},$$

$$\beta = \frac{1}{\sqrt{(hk)^2 + (l^2 + h^2)^2 + (lk)^2}} \begin{bmatrix} -hk & l^2 + h^2 & -lk \end{bmatrix}, \tag{5.7}$$

$$\gamma = \frac{1}{\sqrt{l^2 + h^2 + k^2}} \begin{bmatrix} h & k & l \end{bmatrix}$$

and result in the following direction cosines between axes in the x-y-z and α-β-γ coordinate systems:

$$\begin{pmatrix} a_{\alpha x} & a_{\alpha y} & a_{\alpha z} \\ a_{\beta x} & a_{\beta y} & a_{\beta z} \\ a_{\gamma x} & a_{\gamma y} & a_{\gamma z} \end{pmatrix} = \begin{pmatrix} \dfrac{-l}{\sqrt{l^2 + h^2}} & 0 & \dfrac{h}{\sqrt{l^2 + h^2}} \\ \dfrac{-kh}{\sqrt{k^2 + l^2 + h^2}\sqrt{l^2 + h^2}} & \dfrac{\sqrt{l^2 + h^2}}{\sqrt{k^2 + l^2 + h^2}} & \dfrac{-lk}{\sqrt{k^2 + l^2 + h^2}\sqrt{l^2 + h^2}} \\ \dfrac{h}{\sqrt{k^2 + l^2 + h^2}} & \dfrac{k}{\sqrt{k^2 + l^2 + h^2}} & \dfrac{l}{\sqrt{k^2 + l^2 + h^2}} \end{pmatrix} \tag{5.8}$$

The stress tensor in the x-y-z coordinate system is then

$$\sigma_{kl}^{xyz} = a_{ki}a_{lj}\sigma_{ij}^{\alpha\beta\gamma} \Rightarrow \begin{pmatrix} \sigma_1 \\ \sigma_2 \\ \sigma_3 \\ \sigma_4 \\ \sigma_5 \\ \sigma_6 \end{pmatrix} = \begin{pmatrix} \dfrac{h^2 k^2}{h^2+l^2} \\ h^2+l^2 \\ \dfrac{l^2 k^2}{h^2+l^2} \\ -lk \\ \dfrac{hlk^2}{h^2+l^2} \\ -hk \end{pmatrix} \left(\dfrac{1}{h^2+k^2+l^2} \right) \sigma \tag{5.9}$$

In contracted notation, for monoclinic symmetry, the strain ε_i can be obtained from the stress σ_j

through the compliance matrix S_{ij} from

$$\varepsilon_i = S_{ij}\sigma_j = \begin{pmatrix} S_{11} & S_{12} & S_{13} & 0 & S_{15} & 0 \\ S_{12} & S_{22} & S_{23} & 0 & S_{25} & 0 \\ S_{13} & S_{23} & S_{33} & 0 & S_{35} & 0 \\ 0 & 0 & 0 & S_{44} & 0 & S_{46} \\ S_{15} & S_{25} & S_{35} & 0 & S_{55} & 0 \\ 0 & 0 & 0 & S_{46} & 0 & S_{66} \end{pmatrix} \sigma_j \tag{5.10}$$

Rewriting in tensor notation gives

$$\varepsilon_{ij}^{xyz} = \begin{pmatrix} \varepsilon_1 \\ \varepsilon_2 \\ \varepsilon_3 \\ \varepsilon_4 \\ \varepsilon_5 \\ \varepsilon_6 \end{pmatrix} = \begin{pmatrix} h^2 k^2 S_{11} + \left(h^2+l^2\right)^2 S_{12} + k^2 l^2 S_{13} + hk^2 l S_{15} \\ h^2 k^2 S_{12} + \left(h^2+l^2\right)^2 S_{22} + k^2 l^2 S_{23} + hk^2 l S_{25} \\ h^2 k^2 S_{13} + \left(h^2+l^2\right)^2 S_{23} + k^2 l^2 S_{33} + hk^2 l S_{35} \\ -\dfrac{1}{2}\left(klS_{44} + hkS_{46}\right)\left(h^2+l^2\right) \\ h^2 k^2 S_{15} + \left(h^2+l^2\right)^2 S_{25} + k^2 l^2 S_{35} + hk^2 l S_{55} \\ \dfrac{1}{2}\left(klS_{46} - hkS_{66}\right)\left(h^2+l^2\right) \end{pmatrix} \dfrac{\sigma}{\left(h^2+l^2\right)\left(h^2+k^2+l^2\right)} \tag{5.11}$$

The strain in the α-β-γ coordinate system is then obtained by transforming back from the x-y-z

coordinate system using

$$\varepsilon_{kl}^{\alpha\beta\gamma} = a_{ki}a_{lj}\varepsilon_{ij}^{xyz} \tag{5.12}$$

From the above equation, the strain $\varepsilon_{\gamma\gamma}$ is

$$\varepsilon_{\gamma\gamma} = \left(a_{\gamma x}^{2} \varepsilon_1 + a_{\gamma y}^{2} \varepsilon_2 + a_{\gamma z}^{2} \varepsilon_3 + 2 a_{\gamma x} a_{\gamma y} \varepsilon_6 + 2 a_{\gamma x} a_{\gamma z} \varepsilon_5 + 2 a_{\gamma y} a_{\gamma z} \varepsilon_4 \right) \sigma \qquad (5.13)$$

The strain $\varepsilon_{\perp}^{100}$ is the same as $\varepsilon_{\gamma\gamma}$ which reduces to $S_{23}\sigma$ from above. Thus, ε_{100} per unit stress is shown to be equal to S_{23} (-0.00334 GPa^{-1}) in Ref. [50]. The value of 0.454 is therefore obtained from Eq. (5.4) and compares well with the value of 0.450 obtained from the neutron diffraction measurements.

5.4 Conclusions

This work has provided insight into the elastic response of *B19′* martensitic NiTi variants as they exist in bulk, polycrystalline aggregate form during monotonic compressive and tensile loading. The following conclusions are made by comparing results from *in situ* neutron diffraction experiments during tensile and compressive loading, macroscopic extensometry measurements, a 30,000 grain self-consistent model and a previously published *ab initio* determination of the stiffness tensor for *B19′* martensitic NiTi:

1. There was good agreement between the neutron diffraction measurements reported in this work and the stiffness tensor predicted from *ab initio* studies in Ref. [50]. Given the challenges in obtaining good quality single crystals of martensitic NiTi and the large number of independent constants in the stiffness tenor (thirteen), to the best of the authors' knowledge, this was the first reported validation of the aforementioned theoretically predicted stiffness tensor for *B19′* martensite. The validation was accomplished by measuring elastic moduli in several directions, an average Young's modulus and Poisson's ratio, as well as by defining and measuring a unique Poisson's ratio, and comparing the neutron experiments with theory.

2. From the neutron diffraction measurements an average Young's modulus of 134 GPa and a Poisson's ratio of 0.39 were obtained. Corresponding measurements from extensometry resulted in a deflated Young's modulus due to variant reorientation and detwinning that occur even at lower stresses where the macroscopic stress-strain extensometry appears linear. Direct evidence of variant reorientation and detwinning at low stresses is provided in IPFs constructed from *in situ* neutron diffraction measurements during loading.

3. The neutron diffraction measurements of direction dependent elastic moduli from martensite variants in a polycrystalline aggregate were influenced by crystalline symmetry (or lack thereof), intergranular interaction and constraints, and strain redistribution among variants due to variant reorientation and detwinning. When variant reorientation/conversion and detwinning relax most of the intergranular constraint arising from the neighboring variants, the moduli from neutron measurements compared well with the predictions of single crystals behavior.

5.5 Tables

Table 5.1 Elastic moduli in directions perpendicular to *hkl* planes as determined (i) in a single crystal from Eq. (5.3) ($E_{hkl}^{crystal}$), (ii) from a self-consistent polycrystalline model (E_{hkl}^{model}) and (iii) *in situ* neutron diffraction measurements in a polycrystalline sample ($E_{hkl}^{neutron}$). For a given direction, the number of points used for the linear fit, the linearity correlation coefficient (R) and the error percentages, both, between (i) and (iii) above $\left(\dfrac{E_{hkl}^{crystal} - E_{hkl}^{neutron}}{E_{hkl}^{neutron}} \right)$ and (ii) and (iii) above $\left(\dfrac{E_{hkl}^{model} - E_{hkl}^{neutron}}{E_{hkl}^{neutron}} \right)$ are also indicated.

hkl	Single crystal $E_{hkl}^{crystal}$	Model E_{hkl}^{model}	Neutron diffraction			$\left\| \dfrac{E_{hkl}^{crystal} - E_{hkl}^{neutron}}{E_{hkl}^{neutron}} \right\|$	$\left\| \dfrac{E_{hkl}^{model} - E_{hkl}^{neutron}}{E_{hkl}^{neutron}} \right\|$
			$E_{hkl}^{neutron}$	# of points	R		
100	128.2	129.8	132.2	6	0.997	3.0%	1.8%
012	136.0	146.7	145.4	6	0.978	6.5%	0.9%
102	157.3	152.8	167.1	6	0.999	5.8%	8.6%
-120	33.8	106.0	101.4	6	0.997	66.6%	4.5%
121	84.2	116.3	104.6	6	0.996	19.5%	11.2%
-112	177.6	147.6	165.1	6	0.999	7.6%	10.6%
-122	120.2	143.7	110.5	5	0.991	8.7%	30.0%
-111	85.9	130.2	104.7	5	0.999	17.9%	24.4%
011	175.9	155.7	117.1	6	0.995	50.2%	33.0%
-121	53.4	122.0	93.3	5	1.000	42.8%	30.8%
-110	41.0	105.1	78.2	6	0.997	47.5%	34.4%

(a)   (b)
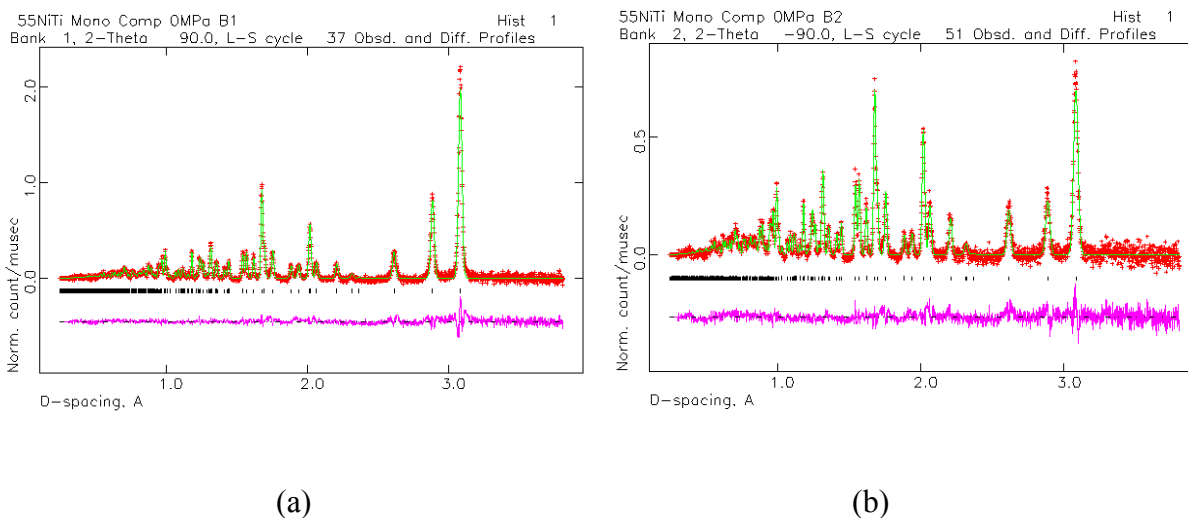
Figure 5.1 Representative GSAS Rietveld refinements of spectra from the monoclinic *B19'* martensite phase recorded at 25 °C in the nominally unloaded condition corresponding to diffracting lattice planes (a) parallel (Bank 1) and (b) perpendicular (Bank 2) to the long axis of the specimen. The crosses are the measured data and the line through them is the Rietveld least squares fit. The tick marks indicate reflections from the martensite. The difference curve between refinement and measurement is also shown at the bottom of the figure.
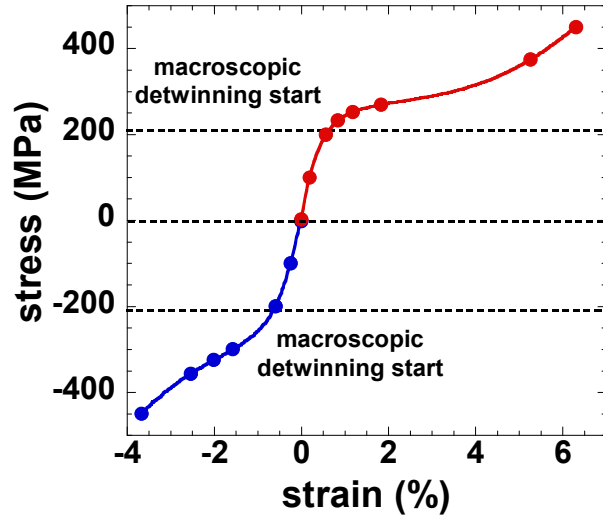
Figure 5.2 Applied stress vs. macroscopic strain measured by extensometry for NiTi in tension and compression. The symbols indicate the stresses at which neutron diffraction spectra were obtained during loading.
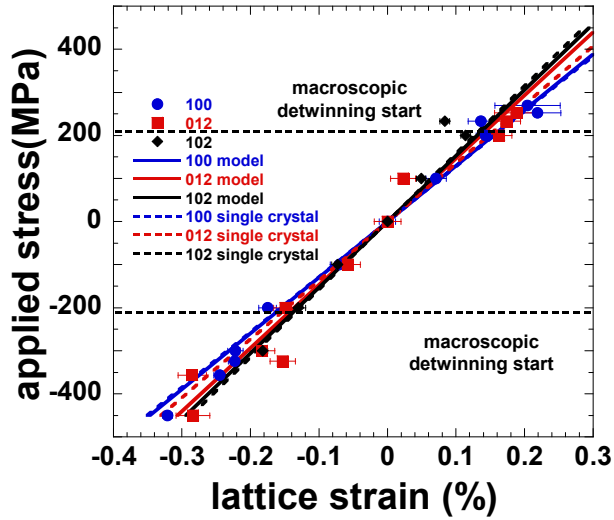
Figure 5.3 Lattice strains in a direction perpendicular to the 100, 012 and 102 planes in NiTi with applied stress. Symbols correspond to neutron diffraction measurements from diffracting planes oriented perpendicular to the loading direction. The solid lines are corresponding predictions of lattice strains with stress in a single crystal from Eq. (5.3) and the dashed lines are corresponding predictions from a self-consistent polycrystalline model.
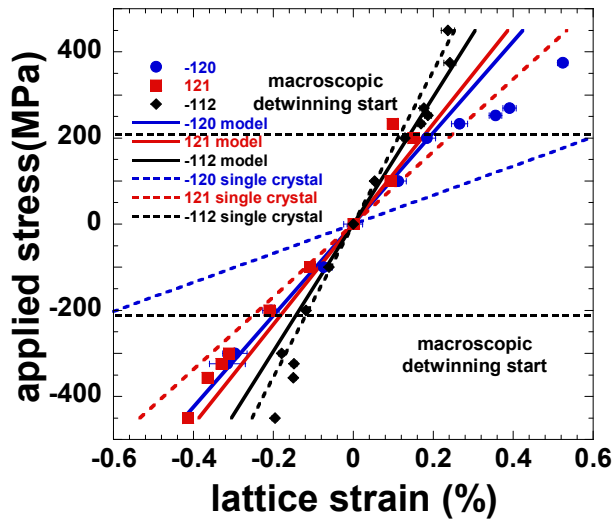
Figure 5.4 Lattice strains in a direction perpendicular to the -120, 121 and -112 planes in NiTi with applied stress. Symbols correspond to neutron diffraction measurements from diffracting planes oriented perpendicular to the loading direction. The solid lines are corresponding predictions of lattice strains with stress in a single crystal from Eq. (5.3) and the dashed lines are corresponding predictions from a self-consistent polycrystalline model.

63
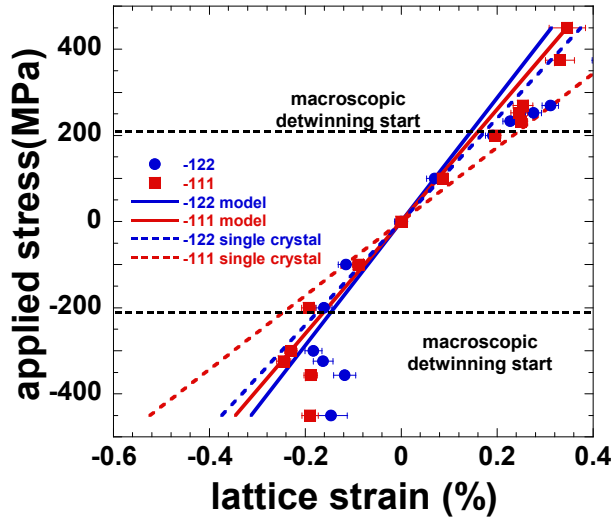
Figure 5.5 Lattice strains in a direction perpendicular to the -122 and -111 planes in NiTi with applied stress. Symbols correspond to neutron diffraction measurements from diffracting planes oriented perpendicular to the loading direction. The solid lines are corresponding predictions of lattice strains with stress in a single crystal from Eq. (5.3) and the dashed lines are corresponding predictions from a self-consistent polycrystalline model.
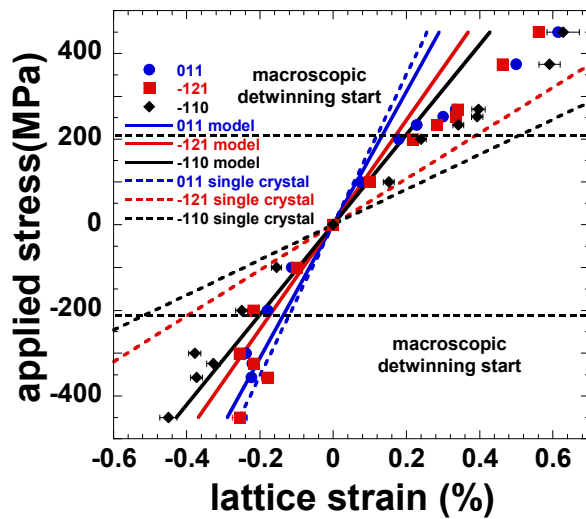
Figure 5.6 Lattice strains in a direction perpendicular to the 011, -121 and -110 planes in NiTi with applied stress. Symbols correspond to neutron diffraction measurements from diffracting planes oriented perpendicular to the loading direction. The solid lines are corresponding predictions of lattice strains with stress in a single crystal from Eq. (5.3) and the dashed lines are corresponding predictions from a self-consistent polycrystalline model.
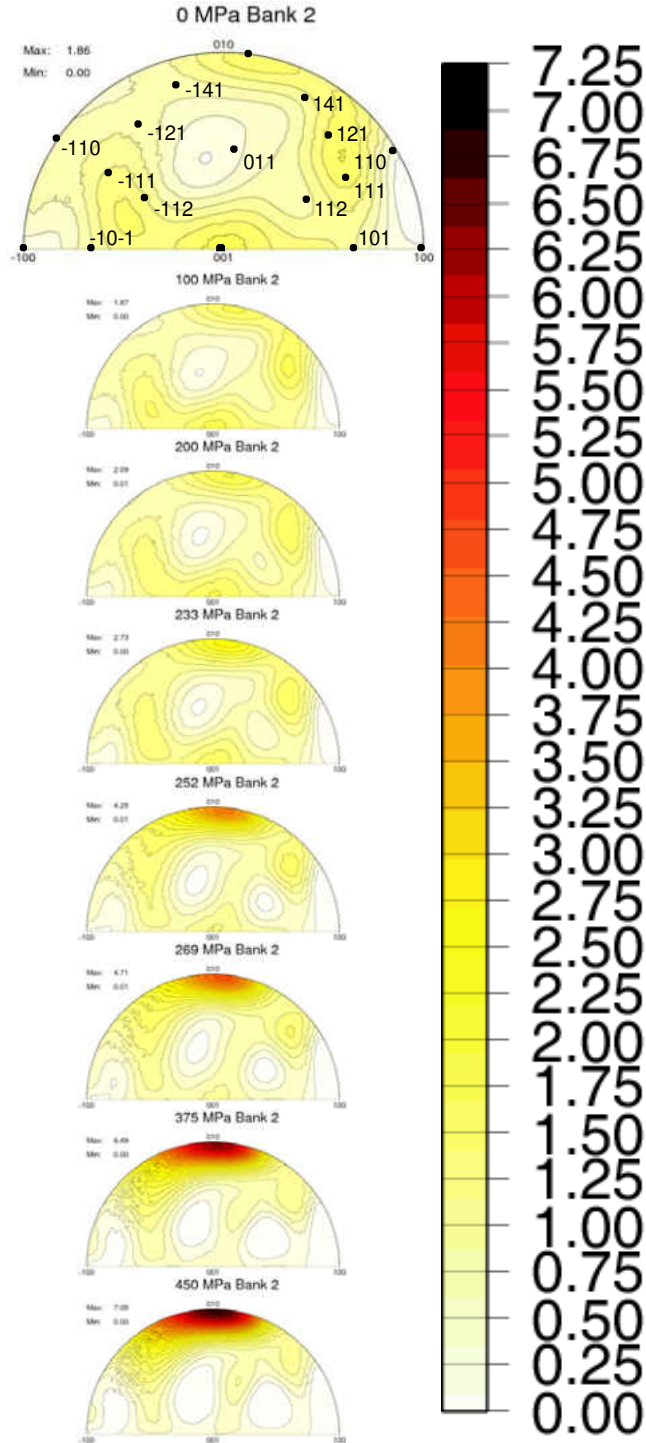
Figure 5.7 Inverse pole figures (IPFs) for the longitudinal direction in *B19'* martensitic NiTi loaded in tension. For a given IPF, the corresponding applied stress is indicated above the IPF. The top left hand corner also indicates the respective maximum and minimum intensities observed in the given IPF, in multiples of random distribution (1 corresponding to a random distribution). For clarity in presentation, the scale chosen is unique to this figure.
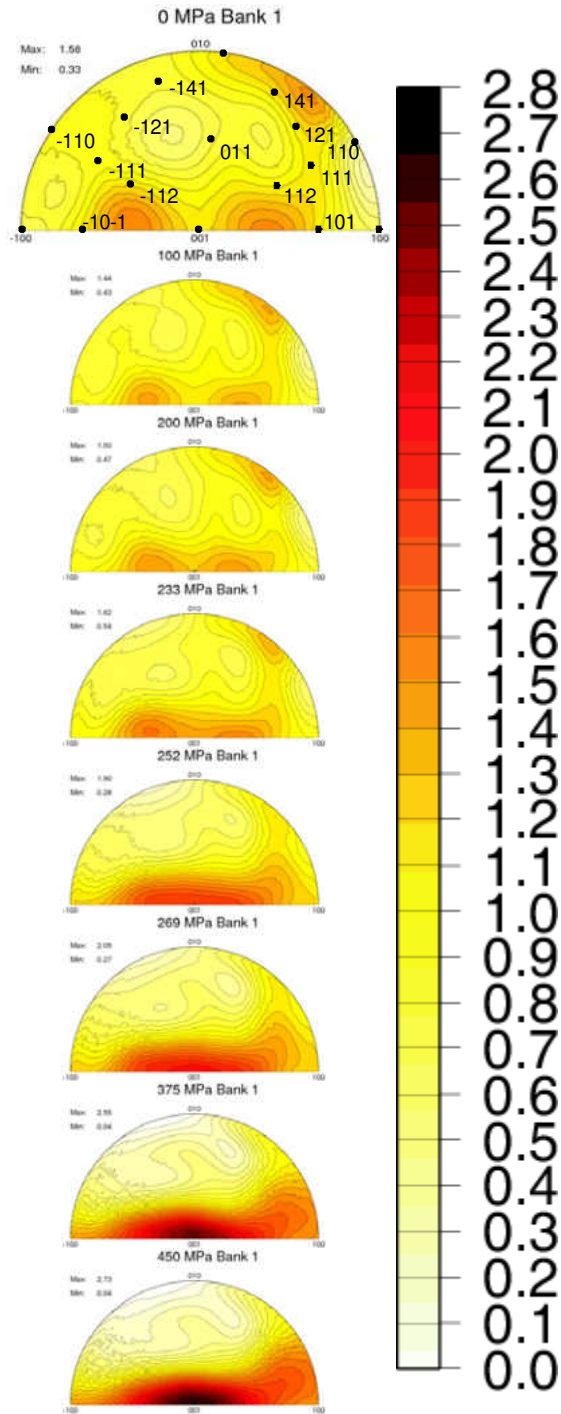
Figure 5.8 Inverse pole figures (IPFs) for the transverse direction in *B19′* martensitic NiTi in tension. For a given IPF, the corresponding applied stress is indicated above the IPF. The top left hand corner also indicates the respective maximum and minimum intensities observed in the given IPF, in multiples of random distribution (1 corresponding to a random distribution). For clarity in presentation, the scale chosen is unique to this figure.
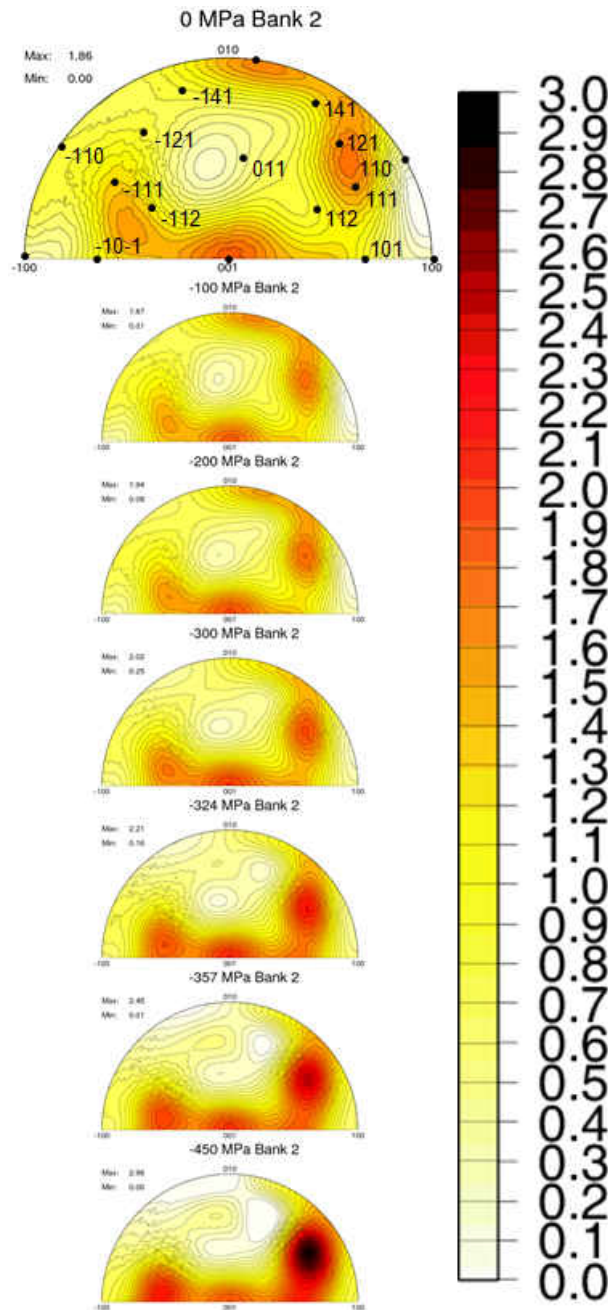
Figure 5.9 Inverse pole figures (IPFs) for the longitudinal direction in *B19′* martensitic NiTi loaded in compression. For a given IPF, the corresponding applied stress is indicated above the IPF. The top left hand corner also indicates the respective maximum and minimum intensities observed in the given IPF, in multiples of random distribution (1 corresponding to a random distribution). For clarity in presentation, the scale chosen is unique to this figure.
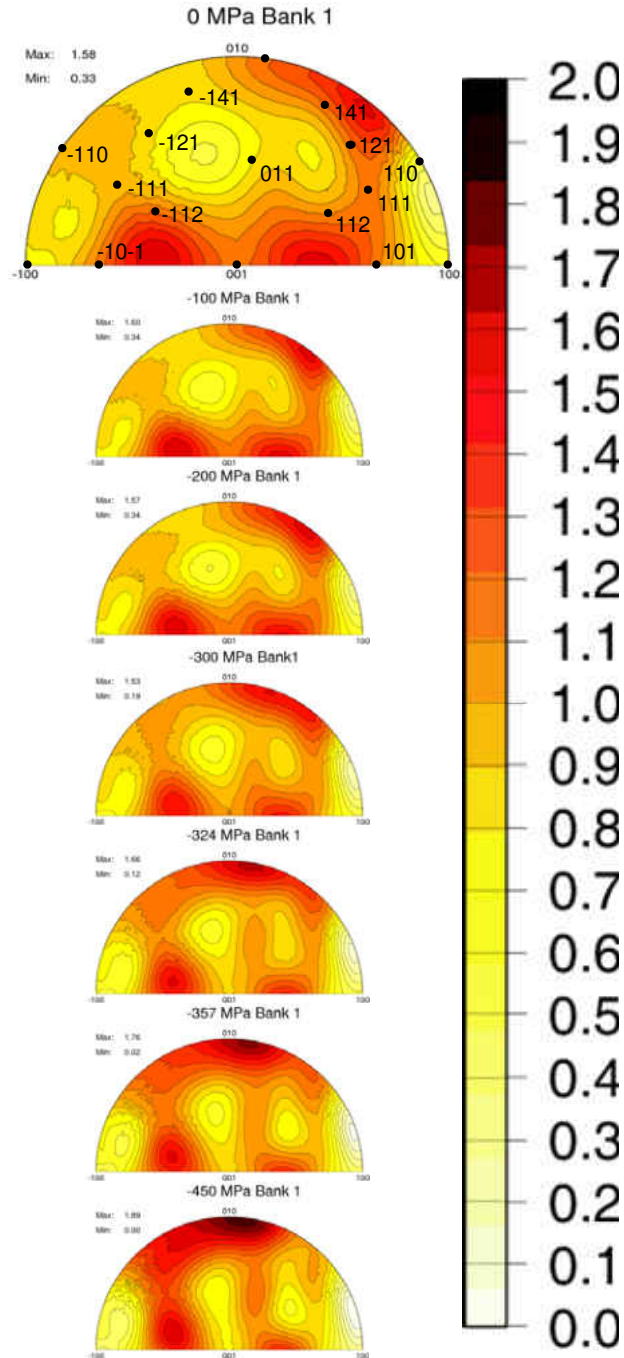
Figure 5.10 Inverse pole figures (IPFs) for the transverse direction in *B19'* martensitic NiTi in compression. For a given IPF, the corresponding applied stress is indicated above the IPF. The top left hand corner also indicates the respective maximum and minimum intensities observed in the given IPF, in multiples of random distribution (1 corresponding to a random distribution). For clarity in presentation, the scale chosen is unique to this figure.
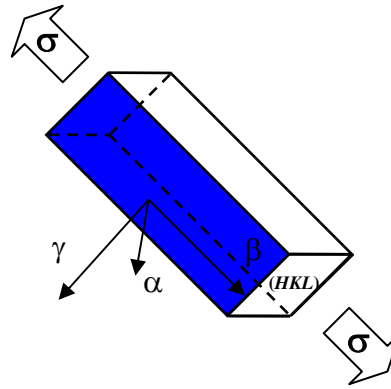
Figure 5.11 The α-β-γ coordinate system defined relative to the diffracting monoclinic variant. Note that the non-orthogonality of the monoclinic unit cell is corrected while going from *hkl* to *HKL* indices.

CHAPTER SIX: AN IN SITU NEUTRON DIFFRACTION STUDY OF THE EFFECT OF UPPER-CYCLE TEMPERATURE ON THE LOAD-BIASED STRAIN-TEMPERATURE RESPONSE OF NıTı

Shape memory NiTi was subjected to neutron diffraction during load-biased thermal cycling under different combinations of applied stress (100 MPa, 200 MPa and 300 MPa) and upper-cycle temperatures (165 ºC, 230 ºC, 290 ºC and 320 ºC). The objective was an in situ examination of the microstructural and micromechanical evolution during the shape memory process, to determine the influence of the upper-cycle temperature on the changes in macroscopic transformation behaviors. Quantitative analyses of texture and lattice strain in both the martensite and austenite phases were obtained through Rietveld refinement of the recorded neutron spectra. The texture analyses were presented in the forms of individual peak ratios, inverse pole figures, and axial distribution plots and the evolution of peak broadening was also determined, to obtain a complete and systematic picture of the underlying microstructural and micromechanical changes. The differences in transformation strain observed during the load-biased thermal cycling under various conditions of stress and upper cycle temperature were found to correlate with changes in the texture of the room temperature martensite and the volume fraction of the martensite retained in the austenite state.

6.1 Introduction

Among the various considerations in the design of SMA actuators with desired performance in a particular temperature range, the work output and repeatability require special attention. Work output can be defined as the product of the applied stress and transformation strain, which is the

difference in strain at the austenite start (A_s) and austenite finish (A_f) temperature [61]. Repeatability refers to the actuator's ability to operate between its deformed shape upon cooling and its original shape upon heating through multiple, successive cycles without accumulating unrecoverable strains. Repeatable actuation characteristics produce dimensionally stable components and facilitate better control, which are particularly vital for actuators designed to work through multiple cycles. In most cases, some open-loop strain (defined as the difference in strain of the martensite state between the start and finish of a thermal cycle) is observed. This parameter can be used to evaluate the dimensional stability of the actuator under service conditions with smaller levels of open-loop strain indicating better repeatability, a characteristic that is highly desirable.

Previous research has focused on studying the effect of applied stress on the performance related parameters of SMA actuators, *e.g.,* transformation strain, open-loop strain, and transformation temperatures [62, 63]. A preliminary study showed that the maximum temperature reached during thermal cycling (or upper-cycle temperature, abbreviated as UCT) under constant stress could significantly affect the observed thermomechanical response of NiTi, especially the amount of transformation strain available for actuation and thus the work output [61]. However, the underlying mechanisms associated with the aforementioned differences in macroscopic response are not clear, and could be due to martensite reorientation and detwinning, retained martensite, or dislocation slip for the different conditions. More recently [64], an extensive load-biased thermal cycling investigation, using selected combinations of stress and UCT, was completed. This study focused on the role of UCT in affecting NiTi actuator transformation behavior related parameters, *i.e.,* transformation temperatures, transformation strain, and open-loop strain. Results from an *in situ* neutron diffraction experiment, performed at the same

71

selected combinations of stress and UCT, provided preliminary correlations between microstructural evolution and the macroscopic changes observed. However, that work was limited in that no quantitative internal strain information was provided and the texture evolution was only followed by recourse to the changes in intensity ratios of two representative diffraction peaks in the diffraction spectra.

Recognizing the existing limitations from previous research, we further extended the analysis of the neutron spectra obtained through *in situ* measurements in Ref. [64], by providing a more detailed and thorough texture and internal strain analysis in both the martensite and austenite phases. The objective of this work was to discern the major contributions of the underlying microstructural and micromechanical changes to the variations in the macroscopic actuator performance. Additionally, in our previous research [52], we have shown that due to the accommodating nature of the martensite phase, there could be a difference in the transformation temperatures measured using direct (*e.g.,* neutron diffraction) and indirect measurement techniques (*e.g.,* ASTM F2082-03 [37]). This difference can lead to remnant or retained martensite that is unaccounted for in the system even after heating to a temperature that would be considered to be "fully" austenitic as determined by the indirect measurement technique. Hence, by providing more detailed and concrete neutron diffraction data analysis, this chapter aims to achieve a better understanding of the UCT influence on SMA performance. In addition, since the optimal temperature chosen during thermal cycling can both maximize the work output and avoid unnecessary overheating, a better understanding of the UCT effect via the aforementioned approach would be beneficial in optimizing the operation of SMA-based actuators. Such an approach would lead to actuator operation with desirable work output, increased energy

72

efficiency and enhanced bandwidth capability. In addition, an understanding of the microstructural and micromechanical evolution would also provide insights important to the modeling of SMA actuator performance.

6.2 Experimental Procedures

Ten millimeter diameter rods of NiTi (nominal composition of 49.9 at.% Ni) were produced by Special Metals, New Hartford, NY, in the hot-rolled/hot-drawn and hot-straightened condition. Cylindrical tensile specimens, 5.08 mm in diameter and 15.24 mm in gauge length, with threaded ends were machined out of the rods by a conventional turning operation. The characteristic phase transformation temperatures, martensite finish (M_f), martensite start (M_s), austenite start (A_s) and austenite finish (A_f), were determined by DSC to be 46, 71, 86 and 109 ± 2 °C, respectively. Using optical microscopy, the average grain size of the material was determined to be ~40 μm, ensuring that a sufficient number of grains were present in the gauge and diffracting volumes to allow the neutron diffraction measurements to be representative of bulk behavior in the polycrystalline samples.

In situ neutron diffraction measurements were performed in "time-of-flight (TOF)" mode on the Spectrometer for MAterials Research at Temperature and Stress (SMARTS) at Los Alamos National Laboratory (LANL). Two no-load thermal cycles between room temperature and 200 °C were performed on the as-machined specimen prior to the following load-biased thermal cycling tests, to relieve residual stress from the machining operation. A series of load-biased thermal cycling tests were completed at selected combinations of tensile stress (100, 200 and 300 MPa) and UCT (165, 230, 290 and 320 °C), with neutron diffraction spectra acquired both at

room temperature (martensite state) and at the highest temperature reached during thermal cycling (austenite state). The chosen combinations of stress and temperature are a subset of testing conditions from Ref. [64], due to the limited beam time available for the experiments. Fig. 6.1 shows an example of the macroscopic strain-temperature response from a sample loaded in series to 100/200/300 MPa under an UCT of 165 °C. The macroscopic strain was measured and reported from an extensometer placed on the sample (gauge length of 10 mm and strain resolution of 5×10^{-5}). The corresponding strain path is indicated sequentially by the letters a through o. Initially, a stress of 100 MPa was applied in the martensite phase at room temperature (to point a). Then under 100 MPa, the sample was subjected to two heating/cooling cycles at a rate of 15 °C/min between room temperature and 165 °C (points b through e), with neutron spectra being acquired during the second cycle (at points c, d and e). Transient microstructural and micromechanical changes occur in the first cycle compared with subsequent cycles, and hence is not used for analysis [61]. A holding period of 5 min was allowed for the temperature to equilibrate before acquiring neutron spectra. It took about 30 min at an average beam current of 100 μA for spectrum acquisition at each point, which ensures adequate statistical quality for further detailed analysis. After the second cycle under 100 MPa, load was increased to 200 MPa in the martensite phase at room temperature (point f) on the same sample, followed by two heating/cooling cycles between room temperature and 165 °C (points g through j). Neutron spectra were collected at comparable points (*e.g.,* h, i and j) to follow the strain and texture evolution in both the martensite and austenite phases. A stress of 300 MPa was applied subsequently (from j to k), following the same experimental scheme through two thermal cycles (indicating by the points through k, l, m, n and o in sequence) and with neutron spectra correspondingly recorded at points m, n and o. To determine the influence of the selected UCTs

74

on the load-bias response, UCTs of 230 °C, 290 °C and 320 °C were used to repeat the aforementioned test on new samples from the same batch of material.

6.3 Results and Discussion

6.3.1 Martensite Evolution

6.3.1.1 Texture

Fig. 6.2 (center) shows the changes in transformation and open-loop strain as a function of UCT and stress. The data in the graph represents the intensity ratios of the two single peak reflections of 100 and 011. The data shown here are from lattice planes aligned parallel to the loading axis. A similar approach was adopted in Ref. [64], using the ratios as a qualitative indication of the texture evolution in the room temperature $B19'$ martensite phase. The data for the 300 MPa, 320 °C case was not available because the sample broke during testing at this condition. Correlations between the peak reflection ratios, macroscopic property changes and selected load-biased thermal cycling conditions can be summarized as follows:

(1) For a given applied stress, increasing the UCT generally causes an increase in the transformation strain that eventually reaches a maximum, which is commensurate with the change in intensity ratios of the 100/011 martensite reflections;

(2) At the same UCT, increasing the applied stress from 100 to 200 MPa increases the transformation strain, with a corresponding increase in the intensity ratios of the 100/011 martensite reflections. A further increase in the applied stress to 300 MPa lowers the

transformation strain, while the intensity ratios of the 100/011 martensite reflections are unchanged from those at 200 MPa;

(3) For the conditions investigated, the transformation strain peaks around 200 MPa/290 °C, corresponding to a maximization of the intensity ratio of the 100/011 martensite reflections;

(4) The open-loop strains under 100 and 200 MPa are very similar, and increase significantly at 300 MPa.

While using the changing ratios of two representative diffraction peaks provides preliminary, qualitative information in texture evolution, IPFs of the *B19'* phase, based on the Rietveld refinement from the entire bank of detectors, were further plotted in the transverse direction to show the details and overall texture evolution, as shown in Fig. 6.2. The transverse direction was chosen because of the higher signal/noise ratio, which enabled a better assessment of subtle changes. The aforementioned observations (1)-(3) still hold true and are supported by systematically following the changes in IPFs with varying stress and temperature. The major difference between the intensity ratios of the 100/011 martensite reflections and the IPFs is observed for the 320 °C UCT condition (for both 100 and 200 MPa), which shows texture that is similar to the texture at lower temperatures (for both stresses). For example, at an applied stress of 200 MPa, the texture seems similar when comparing IPFs at 230 °C and 320 °C. Similar observations are made at corresponding temperatures with an applied stress of 100 MPa. This subtlety in the texture evolution, however, is not captured using the method relying on the 100/011 reflection ratio changes.

Fig. 6.3(a) is a 100 axial distribution plot (ADP) for the *B19′* martensite phase at room temperature during load-biased thermal cycling at selected combinations of UCT and stress, supplementing the information on the texture evolution from the IPFs. In an ADP, the y-axis is a measure of the number of grains (compared to a randomly oriented polycrystal) that are oriented at an angle (ϕ) between the normal of the chosen plane and the loading axis [56]. As shown in Fig. 6.3(a), the shape of the ADP corresponds to a preferential alignment of 100 martensite variants parallel to the tensile loading axis. A similar approach was used to study the axial distribution of 011 martensite variants, which in contrast to the 100 martensite variants, shows a preferential alignment perpendicular to the loading axis. Under tension, the favorable alignment of 100 martensite variants parallel to the loading axis, in conjunction with the alignment of 011 martensite variants perpendicular to the loading axis, is consistent with a (11-1) type I twinning mechanism in NiTi [56, 65]. Further magnification in the region around ϕ=90 provides a direct observation of the evolution of 100 variants parallel to the loading axis with stress and UCT, as shown in Fig. 6.3(b). Examination shows the same trend as that observed in the 100/011 reflection ratio changes as well as in the IPFs, in which higher applied stress and higher UCT (up to a temperature limit of ~320 °C) tend to increase the martensite texture by biasing the system towards the favorable alignment of 100 and 011 variants, with more 100 variants being parallel to and more 011 variants being perpendicular to the loading axis. Investigation of the 011 ADP yields information that supports the same argument and is omitted here to avoid redundancy. Even though the ADPs are determined through refining two banks of diffraction data simultaneously, which is a different approach from obtaining the IPFs, this consistency between different methods validates our analysis of the texture evolution presented above.

Fig. 6.4 presents the normalized raw spectra recorded at a UCT of 165 °C as a function of applied stress, indicating a build-up of retained martensite with increasing stress. At 300 MPa/165 °C, the magnitude of the peak representing the 100 martensite reflection is generally indicative of around 3-4 vol.% retained martensite, but the highly textured structure of the martensite could render this assessment tricky. Regardless, lowering the externally applied stress at the same UCT or increasing the UCT at the same externally applied stress reduces the expected volume fraction of the martensite retained in the system, making the direct observation and evaluation even more difficult. However, the influence of retained martensite on the system (even at low volume fractions) should not be overlooked, as will be seen later when discussing its influence on the evolution of both transformation and internal strain.

The differences in transformation strain observed during the load-biased thermal cycling under various conditions of stress and UCT can thus be correlated with the aforementioned microstructural evolution of the texture of the room temperature martensite. Transformation strain is larger when the room temperature martensite is more textured, which can be achieved by increasing the applied stress or UCT (within certain limits). The volume fraction of the martensite retained in the austenite state could additionally affect the transformation strain. When decreasing the applied stress at the same UCT and/or increasing the UCT at the same applied stress, more martensite variants transform into austenite and higher transformation strain can be thus achieved.

As shown in Fig. 6.4, some amount of retained martensite remains in the austenite state during the reverse transformation upon heating, and the stress fields around the retained martensite may

induce a preferred variant orientation upon cooling. This is similar to the mechanism for two-way shape memory effect, in which certain orientations of the variants can be induced by internal stresses generated after heavy deformation. When increasing the UCT at the same applied stress, less retained martensite will remain upon conversion, thereby promoting the transformation strain. In addition, fewer constraints would be present in the system during cooling and martensite formed under the applied stress would thus achieve a preferred orientation or texture more easily, therefore generating higher transformation strain during the next heating cycle. However, at a critical temperature, less texture evolution is observed with further increases in the UCT. As presented in a later section, intergranular stresses in the austenite were found to relax with heating to higher UCTs. This relaxation can be expected to reduce the biasing stresses while forming martensite during cooling resulting in a weaker texture as observed at higher UCTs in Fig. 6.2 and Fig. 6.3. Additionally, relaxation mechanisms associated with plasticity may also contribute to the aforementioned behavior since an increase in the open-loop strain at high UCTs is also observed. The observed decrease in texture corresponds macroscopically to a reduction in the observed transformation strain. However, an increase in the open-loop strain at high UCTs is also observed, and plasticity could be involved in this process. Plastic deformation hence could compete with the transformation strain, and could be partially responsible for the observed reduction in transformation strain.

At the same UCT, increasing the applied stress from 100 to 200 MPa favors the formation of a more textured variant structure, thereby offering greater amounts of strain output after phase transformation upon heating. Even though higher volume fractions of retained martensite are also expected due to the increase in applied stress, the texturing mechanism is dominant in this

case. However, increasing the applied stress from 200 MPa to 300 MPa, results in larger amounts of retained martensite being formed. This condition, coupled with the fact that the texture was nearly unchanged as well as plasticity competing with the transformation process, leads to a decrease in transformation strain.

6.3.1.2 Lattice Strain Evolution

While the texture evolution in the martensite phase provides a reasonable explanation for the transformation strain changes, we are also interested in understanding how other parameters are also affected, *e.g.,* lattice strain and peak broadening. Fig. 6.5 shows lattice strain evolution in the 100 and 011 planes in the *B19′* martensite phase at room temperature in the transverse direction, after the load-biased thermal cycling, at different combinations of stress and UCT. The lattice strain in the martensite phase in the case of 100 MPa/165 °C load-biased thermal cycling was arbitrarily considered to be zero and used as a reference to follow relative changes in the lattice strain at other combinations of stress and temperature. The following observations were made:

(1) At the same UCT, for both 100 and 011 reflections, lattice strain increases with the increase of the applied stress, as expected;

(2) At the same applied stress, for both 100 and 011 reflections, lattice strain increases with the increase in UCT initially, followed by a drop after 290 °C, the point at which the transformation strain is maximized;

(3) When comparing differences in stress levels at the same UCT, the difference in lattice strains is almost the same for all 100 MPa increases of stress in both 100 and 011 cases. This is

demonstrated by all curves corresponding to different applied stress evolving in a similar trend with temperature.

The difference in the magnitudes of the lattice strains between 100 and 011 reflections can be attributed to the elastic anisotropy of the martensite phase [50]. At the same stress, the evolution of the lattice strain is consistent with both the evolution of the transformation strain and the evolution of the martensitic texture, *i.e.,* as the transformation strain becomes larger the internal strain becomes larger as well. When the system achieves an optimal martensite variant structure, the lattice strain reaches a maximum, indicative of the changes that have occurred in the underlying microstructure. A decrease in lattice strain above 290 °C (similar to the decrease in texture) is observed as well. While it was mentioned previously that there is a similarity of the texture (in terms of the IPFs) when comparing 200 MPa/230 °C vs. 200 MPa/320 °C, and 100 MPa/230 °C vs. 100 MPa/320 °C, respectively, consistency between the resultant texture and internal strain evolution is observed as well. For example, the lattice strains under 200 MPa/230 °C and 200 MPa/320 °C are comparable for both 100 and 011 cases, individually. The fact that lattice strains, for both 100 and 011 cases, evolve in a similar trend with the upper cycle temperature at different stresses seems to suggest that similar mechanisms are consistently driving these changes, as far as the combinations of stress and temperature investigated in this study. Otherwise, strain redistribution can be expected to occur when a new deformation mechanism initiates, *e.g.,* plasticity. For example, previous research showed that strain redistribution and load transfer happened close to the onset of macroscopic plasticity, *e.g.,* in fcc austenitic steel [33], hcp beryllium [59], orthorhombic uranium [57] and fcc aluminum and copper [58], and large deviations in strain in the response of individual planes occurred.

6.3.1.3 Peak Breadth Evolution

Fig. 6.6 shows evolution of the peak broadening, represented by the full width half maximum (FWHM) of 100 and 011 reflections in the *B19′* martensite phase at room temperature after the load-bias response at different combinations of UCT and stress. The following observations were made:

(1) At the same UCT, for both 100 and 011 reflections, FWHM increases with the increase in the applied stress, as expected;

(2) At the same applied stress, for both 100 and 011 reflections, FWHM decreases with an increase in UCT initially, followed by an increase above 290 °C.

At the same UCT, increasing the stress has a tendency to induce heterogeneity of the internal strain distribution, hence leading to the broadening as expected. With an increase of the temperature at the same applied stress, the peak narrows. For example, at 100 MPa, below 290 °C, peak width narrows while the lattice strain increases and the martensite becomes more textured with increasing UCT. As the martensite variants evolve to a more preferred variant structure, shown as a preferential alignment of more 100 martensite variants along the transverse direction, the stress distribution surrounding the 100 variants becomes more uniform, therefore resulting in a narrowing of the peak widths. Moreover, the size increase of the diffracting unit - the correspondence variant, due to the martensite variant combination/growth during the evolution process, could additionally contribute to the peak narrowing. However, when further

increasing the temperature above 290 °C, the peak broadens. In this case, less texture is observed and the inverse explanation now holds.

6.3.2 Evolution in Austenite

From the results obtained from analysis of the individual peak ratios, IPFs, and ADPs, the evolution of the room temperature martensite texture is shown to be an important contributor to the amount of transformation strain observed. However, the amount of martensite retained in the austenite state on heating also plays an important role in determining the transformation strain, since the transformation strain is taken as the strain difference between the martensite and austenite phases. Hence, changes occurring in the austenite state (*e.g.,* texture, lattice strain) are equally important and deserve further investigation.

6.3.2.1 Texture Evolution

Fig. 6.7 shows the IPFs of the *B2* phase in the loading direction at selected combinations of UCT and stress, which can be utilized to understand the corresponding texture evolution as a function of both stress and temperature. Fewer grains with their 111 planes are preferentially aligned perpendicular to the tensile loading direction, by either increasing the applied stress at the same UCT, or increasing UCT at the same applied stress.

Fig. 6.8(a) shows evolution of 111 axial distribution for the *B2* austenite phase at selected combinations of UCT and stress, supporting the texture evolution presented above. The overall shape of the ADP corresponds to a preferential alignment of 111 austenite planes perpendicular

to the loading axis under tension. Further magnification in the region around $\phi=0$ provides a direct observation of the evolution of 111 with stress and UCT along the loading direction, as shown in Fig. 6.8(b). Examination shows the consistency of the evolution as observed in Fig. 6.7.

It is interesting to note that the texture evolution is similar by either increasing the applied stress at the same UCT, or increasing the UCT at the same applied stress, both of which show less favorable formation of grains with their 111 lattice planes aligned perpendicular to the tensile loading direction. Since the volume fraction of retained martensite changes in opposite directions in the above two scenarios (expected to increase when increasing the applied stress at the same UCT, but decrease when increasing the UCT with the same applied stress), this suggests that the resultant texture change in austenite is influenced by more than the sole effect of retained martensite. It was shown that not all martensite reflections convert to austenite at the same rate during the phase transformation [38]. At the same UCT, a greater volume fraction of martensite is expected to remain with an increase in the applied stress, however, in different ratios for different martensite variants. Owing to the unique lattice correspondence between the austenite and martensite phases, the variation in the retained martensite texture results in the corresponding texture changes in the austenite phase. In work performed previously, it was observed that the austenite which was initially texture free developed texture during the process of stress induced phase transformation to martensite [36, 38]. In our case, an increase in UCT under the same applied stress causes fewer grains with their 111 planes aligned perpendicular the loading direction. This was also the case when lattice planes parallel to the loading direction were considered. The 111 austenite orientation in tension is an easy direction for transformation. It transforms generating strains of around 7.5% as determined in Chapter Eight. Since it is an

easy direction, it is the first to transform during the forward transformation and the last to transform back during the reverse transformation. Hence, during the reverse transformation the resulting mismatch could possibly lead to localized plastic deformation resulting in a drop in the intensity corresponding to the 111 orientation in the IPFs as presented above.

6.3.2.2 Lattice Strain Evolution

Figs. 6.9(a)-(c) shows evolution of lattice strain for the 110, 111 and 100 reflections of the *B2* phase in the loading direction as a function of UCT and stress. Since it is difficult to obtain a "stress free" state for austenite in the current experimental scheme during the load-bias process, relative lattice strain changes with temperature and stress were studied instead. Therefore, the 100 MPa/165 °C condition was arbitrarily selected as the reference state. Strains due to thermal expansion above 165 °C were further subtracted, using the same value of 13 x 10^{-6}/°C [52] for all three orientations owing to the isotropic nature of thermal expansion in the austenite phase. Therefore, relative changes of the lattice strain with stress and temperature, due to micromechanical and microstructural mechanisms other than thermal expansion, were tracked. Overall, distinctive lattice strain evolution is observed in the three crystallographic orientations, as shown in Figs. 6.9(a)-(c). Since multiple factors that could influence the lattice strain (*e.g.,* retained martensite, elastic anisotropy, strain compatibility due to the polycrystal sample environment, possible plastic anisotropy if there is any localized plasticity, etc.) are present within the austenite state, deconvolution of the exact contribution from each factor was not possible. Instead, a general appreciation (or perception) of the changes in the intergranular strain and stress of different orientations with stress and temperature, as a result of the overall effects of the aforementioned factors, would be more valuable and realistic.

The elastic moduli for 100, 110 and 111 of the *B2* austenite phase were determined to be 51, 78 and 95 GPa, using single crystal stiffness constants C_{11} = 137 GPa, C_{12} = 103 GPa and C_{44} = 34 GPa [66]; and 48, 77, 97 GPa instead using single crystal stiffness constants C_{11} = 162 GPa, C_{12} = 129 GPa and C_{44} = 35 GPa [67]. Since good agreement in estimating the elastic moduli was achieved by using either of the two data sets, the following calculations were only done based on the stiffness constants reported in Ref. [66]. In the 110 orientation, overall evolution of the lattice strain with increasing temperature at different applied stress seems to follow the same trend, as shown in Fig. 6.9(a). This suggests that there is no change for the underlying mechanisms which determine the lattice response, when the stress changes from 100 MPa to 300 MPa during the thermal cycling. The intergranular stress difference on the 110 grains between 165 °C/100 MPa and 165 °C/300 MPa was determined to be 241.8 MPa, which is closely comparable to the difference in the applied stress (200 MPa). The maximum intergranular stress difference was obtained by comparing the 165 °C/100 MPa and 230 °C/300 MPa states, and was determined to be 289.0 MPa. An estimation of the intergranular stress differences due to thermal effects (other than thermal expansion) was also made to appreciate the thermal contribution. In this case, thermal contributions could be manifested in microstructure changes (*e.g.,* conversion of more retained martensite due to temperature increase or local relaxation processes), which could in turn change the lattice strain. By comparing the 165 °C/100 MPa and 230 °C/100 MPa states, the intergranular stress difference due to such effects was estimated to be 33.2 MPa. When increasing the temperature under the same stress, a comparable magnitude of the intergranular stress was obtained, as shown in Fig. 6.9(a).

At temperatures below 290 °C, the 111 orientation exhibits similar lattice strain changes for both the 100 and 200 MPa conditions, as shown in Fig. 6.9(b). However, significant changes are observed upon either increasing the temperature to 320 °C or increasing the applied stress to 300 MPa. These changes imply that a change in underlying mechanism is exhibited above 290 °C and/or 200 MPa. Intergranular stress estimations were attempted to compare with those obtained for the 110 orientation. The internal stress difference between 165 °C/100 MPa and 165 °C/300 MPa was estimated to be 64.4 MPa while a maximum intergranular stress increase of 201.9 MPa was obtained between the 165 °C/100 MPa and 230 °C/300 MPa states. By comparing 165 °C/100 MPa and 230 °C/100 MPa conditions, the internal stress increase due to thermal effects (other than thermal expansion) was determined to be 43.2 MPa for the 111 orientation. However, when comparing 165 °C/200 MPa and 320 °C/200 MPa conditions, the increase of the internal stress due to thermal effects can be as high as 147 MPa for the same orientation.

As shown in Fig. 6.9(c), the intergranular stress difference between 165 °C/100 MPa and 165 °C/300 MPa was estimated to be 503.4 MPa for the 100 orientation. This happens to be the absolute maximum, when all of the available stress/temperature combinations are considered. In comparing the 165 °C/100 MPa and 230 °C/100 MPa conditions, similar to what was previously done for the 111 orientation, it was determined that the thermal contribution to the internal stress increase was only 26.3 MPa for the 100 direction.

In general, the magnitude of the intergranular stress changes due to the thermal effects (thermal expansion not included) is comparable for all three orientations and is an order of magnitude less than the influence from the applied stress. However, as shown for the case of 111 orientation, the

intergranular stress change can be as high as 147 MPa. Hence, for certain orientations, when the temperature is high enough, the influence of changing temperature at the same stress on the changes of the intergranular stress can still be comparable to that of changing the externally applied stress at the same temperature.

We also note that the 100 austenite orientation is incapable of generating a tensile strain during the phase transformation (see Chapter Eight). Therefore, this hard direction under an externally applied tensile stress experiences a large mismatch with the applied tensile stress field and experiences large tensile strains as a result of the need to satisfy compatibility among grains. This explains why the strain in the 100 direction is exceedingly large and decreases with heating as the stresses relax with temperature. Strains in the 111 and 110 austenite orientations on the other hand increase as they relax, eventually reaching an equilibrium stress free state where the average strain lies between that of the 100 and the 111 and 110 oriented austenite grains. We emphasize that this behavior requires retained martensite to be present and is hence only observed in the 200 MPa and 300 MPa experiments.

6.3.2.3 Peak Breadth Evolution

Fig. 6.10 shows evolution of the full width half maximum (FWHM) as a function of UCT and stress, determined from a single peak fitting of the important reflections (*e.g.,* 110, 111 and 100) of the *B2* phase. At a UCT of 165 °C, increasing the stress has a greater likelihood of increasing the heterogeneity of the internal strain distribution, hence leading to the broadening as expected. Additionally, higher stresses can promote greater amounts of retained martensite, which will also contribute to peak broadening, due to the mismatch stress between the austenite and retained

martensite. The difference in the FWHM between different applied stress levels is the largest at a UCT of 165 °C for all the three orientations, and becomes smaller with further increases in UCT. At 320 °C, there is almost no difference among different stresses. Hence, the temperature seems to play a more important role in influencing the peak width than the applied stress. Considering the austenite finish temperature (109 ± 2 ℃) from DSC, the difference in the volume fraction of retained martensite between different stresses is the largest at 165 °C, compared with other temperatures. At the same applied stress, increasing the UCT causes overall peak narrowing, indicated by a reduction in the FWHM. This reduction can be largely due to the relaxation of the mismatch stress between the austenite and retained martensite, as more retained martensite is transformed at higher temperatures.

6.4 Conclusions

While most of the previous work focused on the effect of the applied stress on the load-biased strain-temperature response of shape memory NiTi, we present here the effect of upper-cycle temperature instead, focusing on the microstructural and micromechanical changes responsible for the macromechanical evolution. The texture analyses were presented in the forms of individual peak ratios, inverse pole figures, and axial distribution functions and the evolution of the peak breadth was also determined, to obtain a complete and systematic picture of the underlying microstructural and micromechanical changes. A systematic study in the evolution of texture and lattice strain in both the martensite and austenite phases was hence obtained and the following conclusions were made:

1. While changes in the transformation strain are certainly influenced by the texture evolution of room temperature martensite resulting from the load-biased thermal cycling, the contribution from the austenite phase could be better understood in terms of its internal strain evolution.

2. The differences in transformation strain observed during the load-biased thermal cycling under various combinations of stress and upper cycle temperature were found to correlate with changes in the texture of the room temperature martensite.

3. The volume fraction of the martensite retained in the austenite state additionally affected the transformation strain. When more martensite variants transformed into austenite by decreasing the applied stress at the same UCT and/or increasing the UCT at the same applied stress, higher transformation strain was achieved.

4. In tension, 111 oriented *B2* austenite grains are soft, in terms of the propensity for phase transformation into martensite. Localized plasticity was expected to be induced in the grains of this soft orientation, and may hence be responsible for the decrease in the 111 peak intensity.

The above observations show that evolution of texture in both the martensite and austenite phases and retained martensite play an important role in determining the thermo-mechanical properties of SMA-based actuators. Combined with additional detailed information on the changes in lattice strain and peak breadth for the two phases, this study has indicated changes that may prove useful in optimizing the thermomechanical processing and operation of SMA actuators for desired performance.
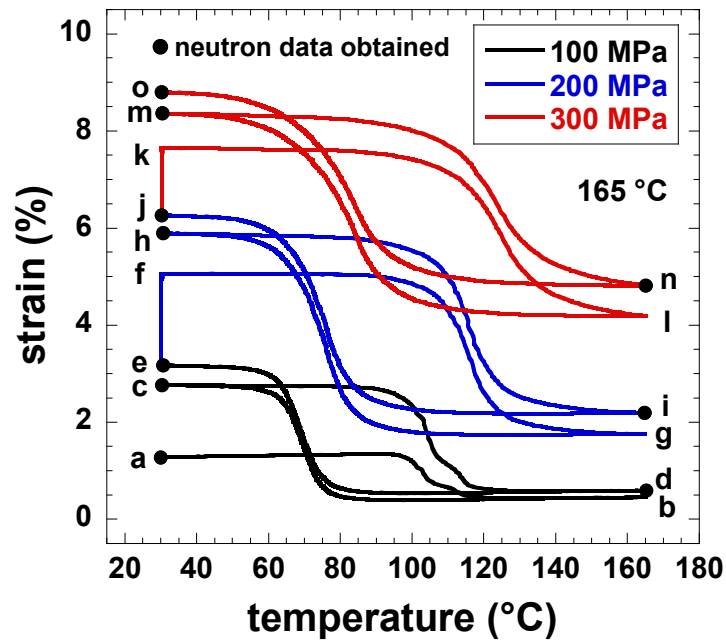
Figure 6.1 Macroscopic strain-temperature response of NiTi during constrained recovery testing to an upper cycle temperature of 165 °C. The strain path is indicated sequentially by the letters a through o. The solid symbols indicate the condition at which neutron diffraction spectra were collected.
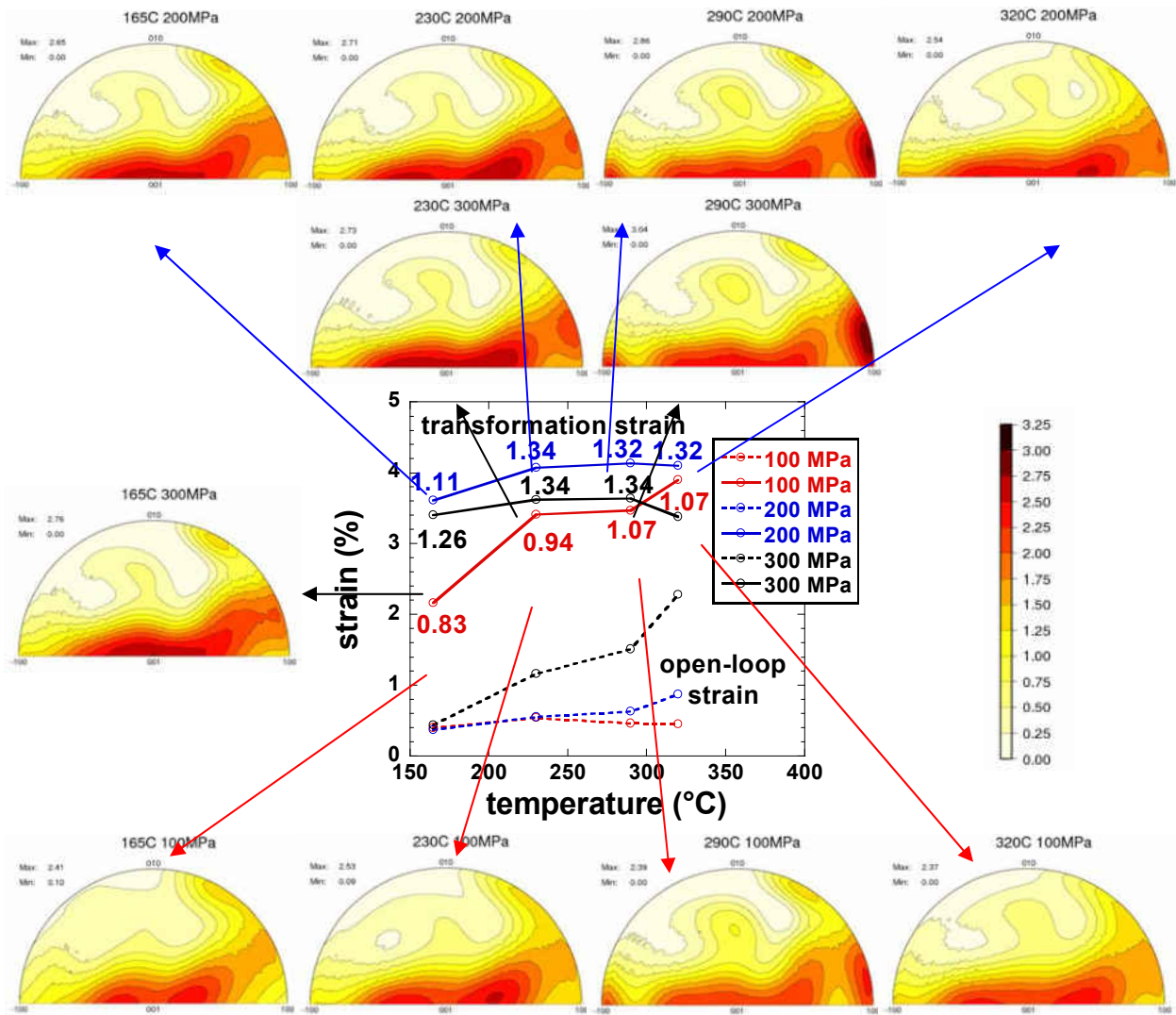
Figure 6.2 Transformation and open-loop strains as a function of upper cycle temperature and stress in NiTi. Numbers in the graph are 100/011 peak intensity ratios of the *B19′* phase at room temperature. The corresponding IPFs show the texture in the transverse direction during the load-biased thermal cycling. The top left hand corner also indicates the respective maximum and minimum intensities observed in the given IPF, in multiples of random distribution (1 corresponding to a random distribution).
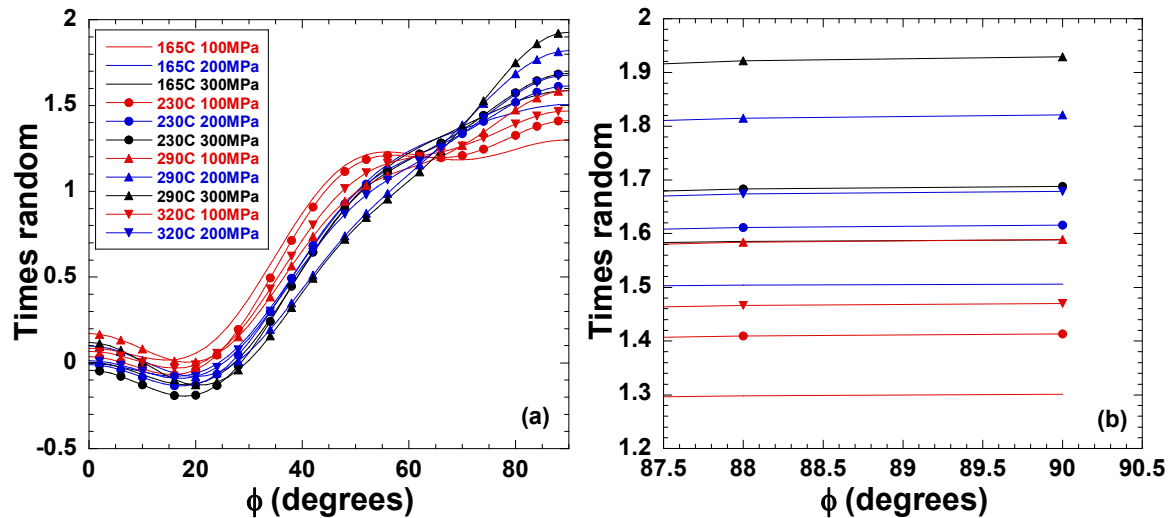
Figure 6.3 100 axial distribution plots of the *B19′* martensite phase at room temperature during the constrained recovery testing at selected combinations of upper cycle temperature and stress, showing (a) the region between $\phi=0$ and $\phi=90$; (b) the magnified region close to $\phi=90$.
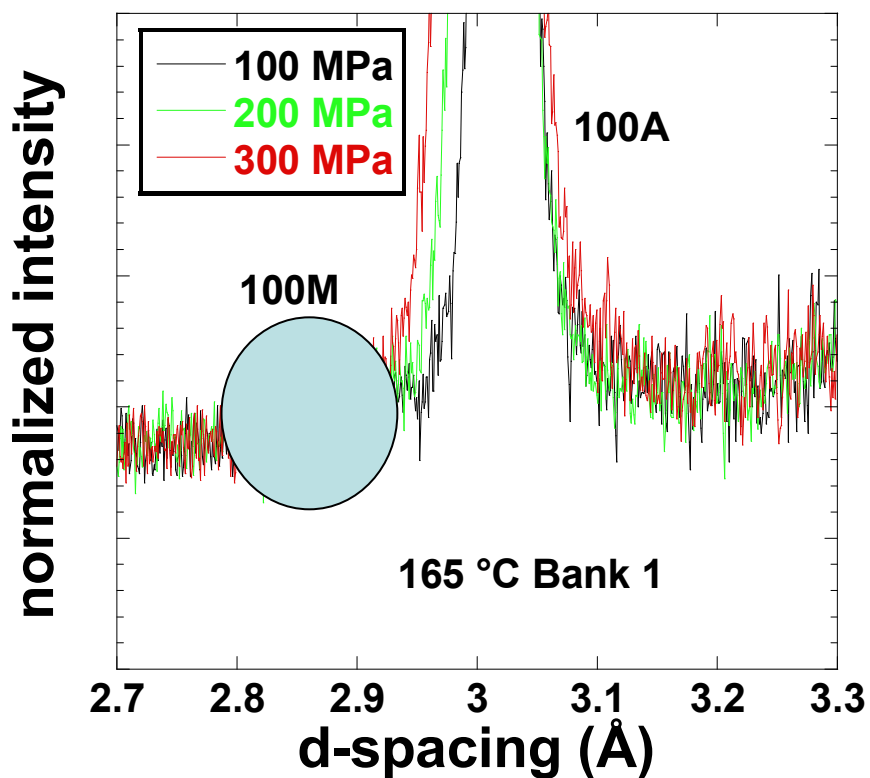
Figure 6.4 Normalized raw spectra recorded at an UCT of 165 °C with different externally applied stresses, showing retained martensite with an increase in stress. The spectra shown here are from diffracting lattice planes parallel to the loading axis.
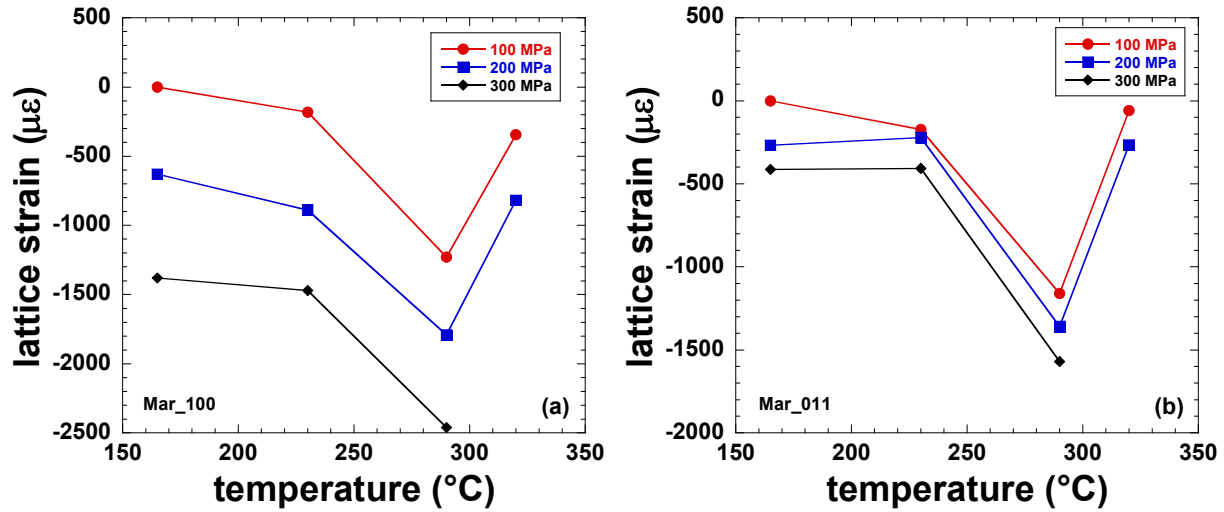
Figure 6.5 Lattice strain evolution in a direction perpendicular to the (a) 100, and (b) 011 planes in the *B19′* martensite phase at room temperature after load-biased thermal cycling at different combinations of upper cycle temperature and stress. Symbols correspond to neutron diffraction measurements from diffracting planes oriented parallel to the loading direction.
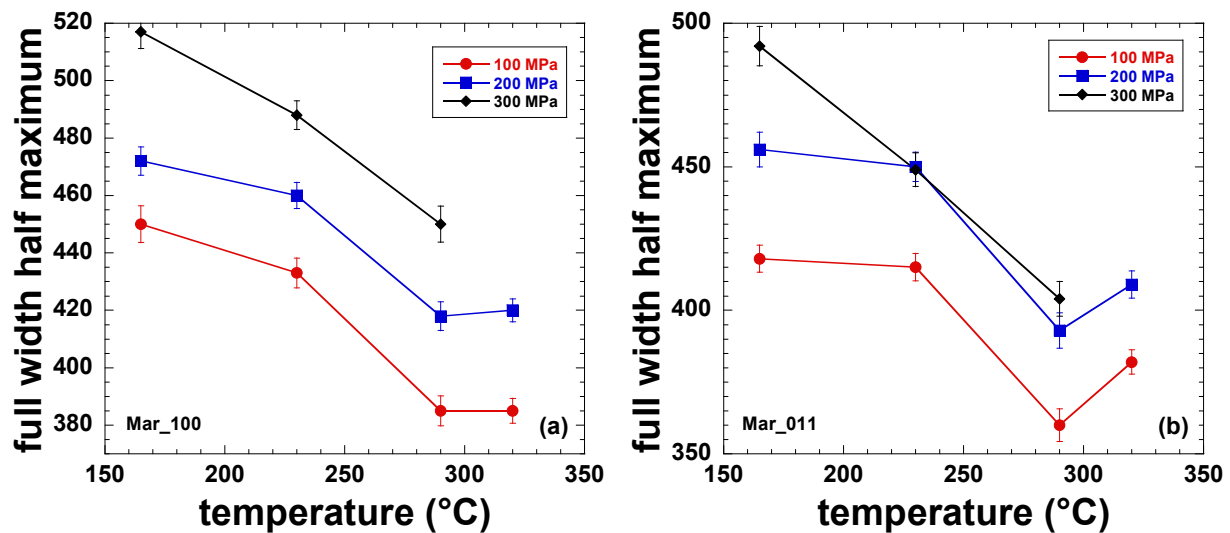
Figure 6.6 Evolution of the full width half maximum (FWHM) of (a) 100, and (b) 011 peak reflections in the *B19′* martensite phase at room temperature after load-biased thermal cycling at different combinations of upper cycle temperature and stress. Symbols correspond to neutron diffraction measurements from diffracting planes oriented parallel to the loading direction.
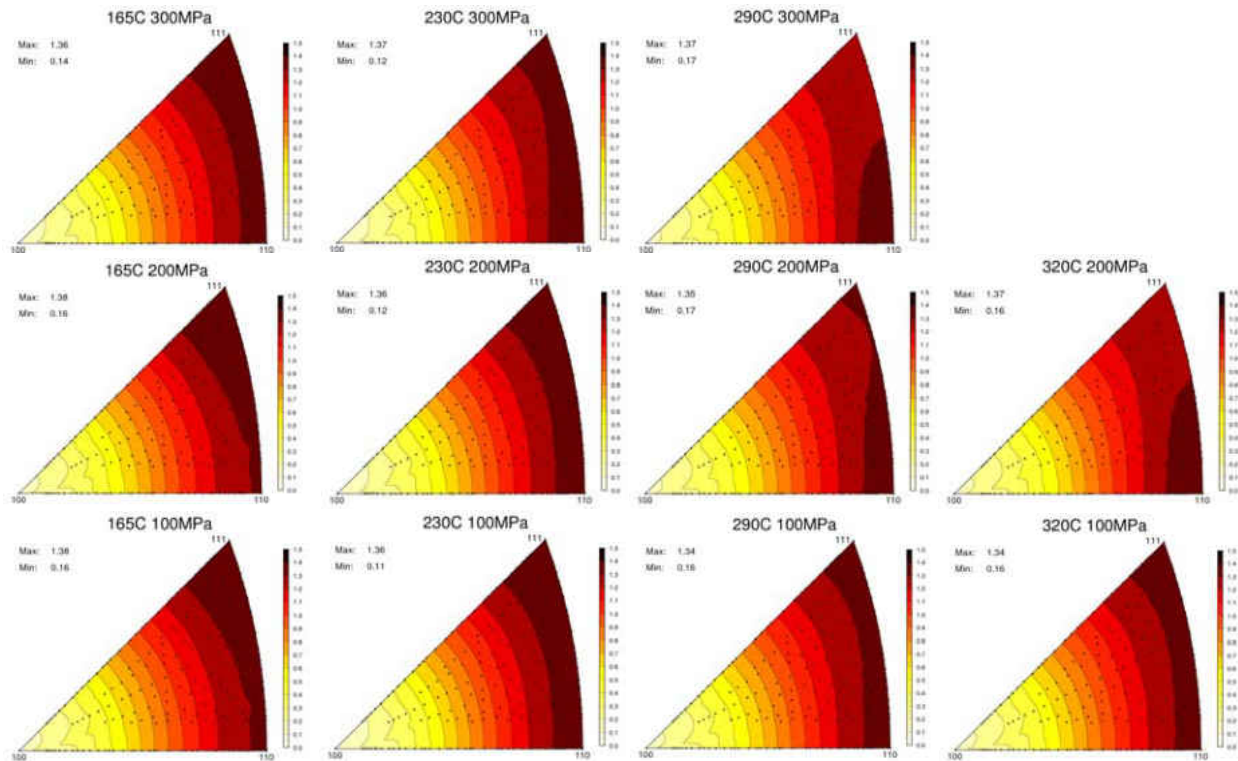
Figure 6.7 Inverse pole figures (IPFs) for the longitudinal direction in the *B2* phase as a function of upper cycle temperature and stress. The top left hand corner also indicates the respective maximum and minimum intensities observed in the given IPF, in multiples of random distribution (1 corresponding to a random distribution).
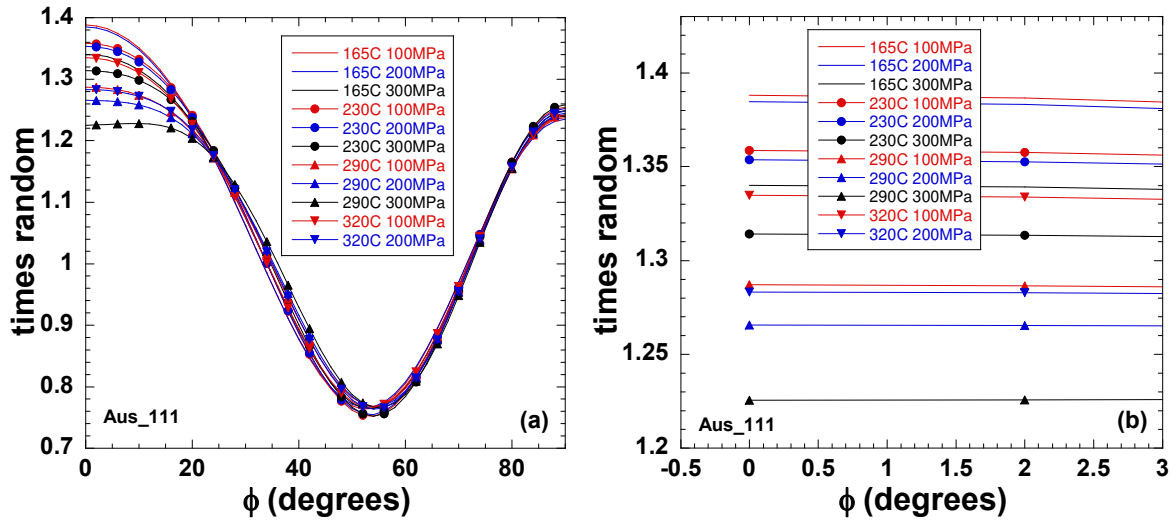
Figure 6.8 111 axial distribution plots for the *B2* austenite phase at selected combinations of upper cycle temperature and stress, showing (a) the region between ϕ=0 and ϕ=90; (b) the magnified region close to ϕ=0.

Figure 6.9 Lattice strain evolution in a direction perpendicular to the (a) 110, (b) 111 and (c) 100 planes in the *B2* austenite phase as a function of upper cycle temperature and stress. Symbols correspond to neutron diffraction measurements from diffracting planes oriented perpendicular to the loading direction.
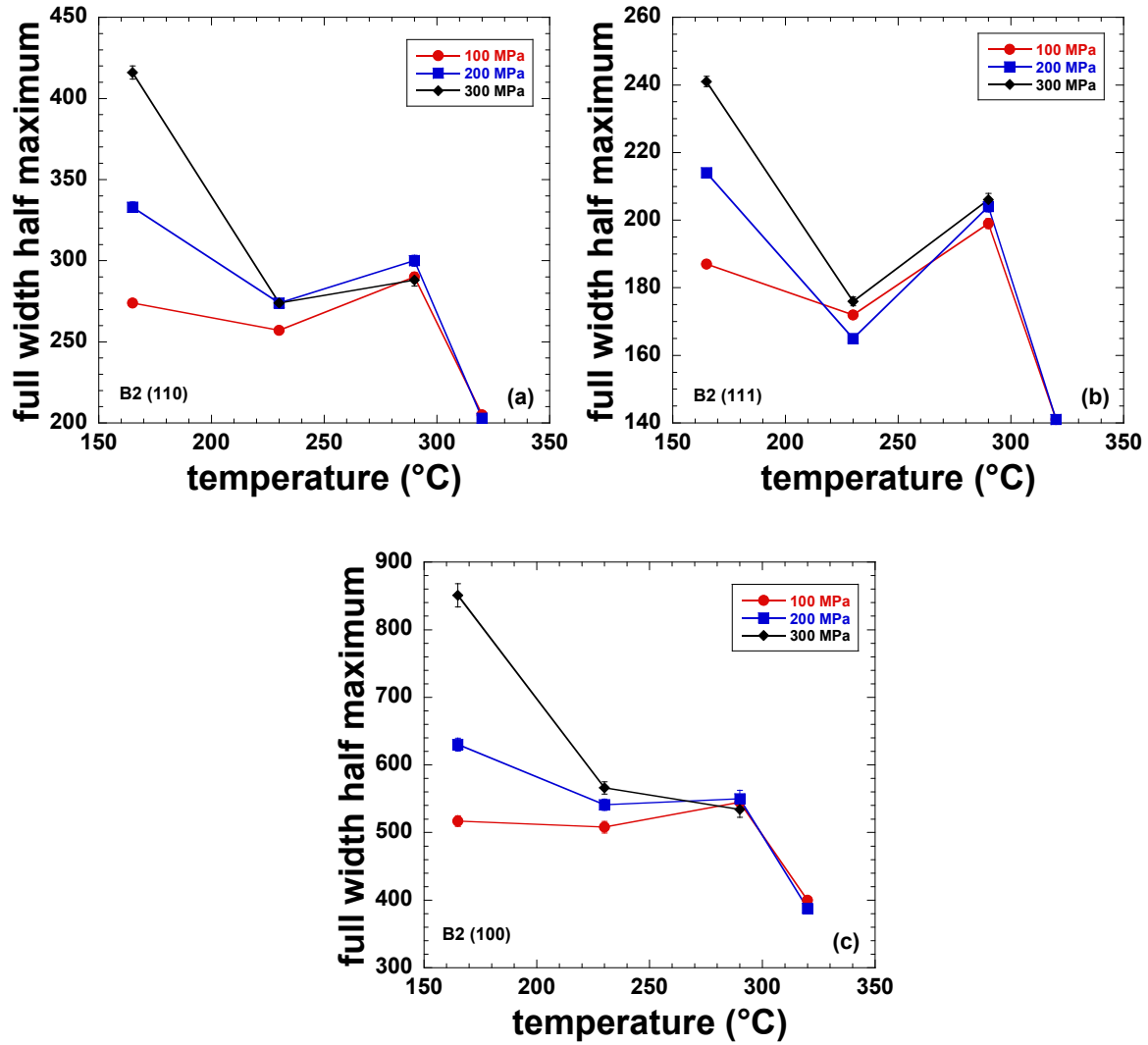
Figure 6.10 Evolution of full width half maximum (FWHM) of (a) 110, (b) 111 and (c) 100 peak reflections in the *B2* phase as a function of upper cycle temperature and stress. Symbols correspond to neutron diffraction measurements from diffracting planes oriented perpendicular to the loading direction.

CHAPTER SEVEN: THE ROLE OF RETAINED MARTENSITE DURING THERMAL-MECHANICAL CYCLING IN NɪTɪ AND NɪTɪPᴅ

The role of retained martensite during thermal-mechanical cycling in NiTi and NiTiPd shape memory alloys is investigated and reported in this chapter. The experiments conducted included selected combinations of loading, heating and cooling while simultaneously acquiring neutron spectra and recording macroscopic strains. Direct correlations were made between macroscopic changes in actuator performance parameters, i.e., transformation strain and open-loop strain that were recorded by extensometry, and atomic-scale evolution in the lattice strain, texture and phase fraction that were obtained through Rietveld refinement and single-peak analyses of neutron spectra. The role of symmetry, i.e., B19' monoclinic martensite vs. B19 orthorhombic martensite in these alloys was also assessed.

7.1 Introduction

Combinations of cyclic thermal and mechanical loading are a major service mode for applications of NiTi shape memory alloys (SMAs). Microstructural and micromechanical changes in strain, texture, and phase volume fraction associated with the cycling process can be expected to change macroscopic characteristics, which can in turn increase fatigue and limit the service life of shape memory components. Research has been done to study structural fatigue in superelastic NiTi [68-72]. However, not much work has addressed the cyclic performance of NiTi actuators in strain-temperature space where the shape memory effect dominates. Lack of experimental data and understanding thus has become a major barrier for present and potential

applications of shape memory actuators. A good understanding of the underlying microstructural changes responsible for the macroscopic evolution is highly desired. This facilitates the establishment of training criteria and rules for safe design of shape memory components.

Previously, the role of upper-cycle temperature, *i.e.,* the maximum temperature reached during thermal cycling, was investigated during load-biased thermal cycling of NiTi SMAs at selected combinations of stress and temperature [64]. Retained martensite was found to be responsible for the internal strain evolution of the *B2* austenite phase and influence the open-loop strain as well. However, due to the small volume fraction of martensite retained in the austenite state, it was difficult to obtain complete insight into its influence. The objective of this work is hence to further assess and understand the role of retained martensite. While conventional binary NiTi SMAs are known for their high work output in actuator applications, they are limited in their operating capability due to a maximum phase transformation temperature of around 100 °C. Recently, there has been a substantial effort to elevate phase transformation temperatures by utilizing ternary elemental additions, *e.g.,* Pd [18, 73-74]. To facilitate potential applications of NiTiPd high temperature SMAs as actuators, a better understanding of the response during thermal-mechanical cycling is essential. In this study, *in situ* neutron diffraction measurements were performed during load-biased thermal cycling at selected stress and temperature in both NiTi and NiTiPd alloys, and assessment of the volume fractions of retained martensite were specifically targeted through multiple thermal cycles. Dimensional stabilities of these alloys were correlated with the volume fraction and texture of the retained martensite, and the internal strain evolution obtained from Rietveld refinement [26, 28, 29] and single-peak analyses [36] of

neutron spectra. The effect of introducing Pd to NiTi on the evolution of transformation strain, open-loop strain as well as the texture evolution was assessed.

7.2 Experimental Procedures

Two alloys were investigated in this study: $Ni_{49.9}Ti_{50.1}$ and $Ni_{29.5}Ti_{50.5}Pd_{20.0}$. For $Ni_{49.9}Ti_{50.1}$, ten millimeter diameter rods were first produced by Special Metals, New Hartford, NY, in the hot-rolled/hot-drawn and hot-straightened condition. For $Ni_{29.5}Ti_{50.5}Pd_{20.0}$, ingots were initially produced by vacuum induction melting using graphite crucibles. After casting, the ingots were homogenized in vacuum at 1050 °C for 72 h, followed by extrusion at 900 °C at an area reduction ratio of 7:1. Cylindrical compressive specimens of the two compositions, 9.01 mm in diameter and 21.6 mm in length, were further fabricated by electrical discharge machining (EDM) rough blanks that were finish ground to the final dimension. The martensite finish (M_f), martensite start (M_s), austenite start (A_s) and austenite finish (A_f) temperatures were determined by differential scanning calorimetry to be 46, 71, 86 and 109 ± 2 ºC, respectively for $Ni_{49.9}Ti_{50.1}$ and 123, 132, 133 and 143 ± 2 ºC for $Ni_{29.5}Ti_{50.5}Pd_{20.0}$.

In situ neutron diffraction measurements, with the sample being mechanically loaded and subjected to temperature changes, were performed in "time-of-flight" mode using the Spectrometer for MAterials Research at Temperature and Stress (SMARTS) at Los Alamos National Laboratory (LANL). Two no-load (at a compressive holding stress of 4 MPa) thermal cycles were performed first on the "as-machined" $Ni_{49.9}Ti_{50.1}$ specimen between room temperature and 200 ºC at a rate of 15 °C/min, to relieve any internal stresses resulting from machining. Under a compressive stress of 150 MPa, the specimen was then subjected to seven

heating/cooling cycles at a rate of 15 °C/min between 25 °C and 130 °C. At both temperature extremes, a holding period of 5 min was allowed for the temperature to equilibrate and 30 min was required to acquire neutron spectra. The temperature of 130 °C was selected based on (A_f+5) °C where A_f was the austenite finish temperature at which the martensite to austenite phase transformation was complete as determined by neutron diffraction at a compressive stress of 150 MPa in the first cycle. The sample was unloaded at 25 °C followed by another thermal cycle between 25 °C and 130 °C. The stress, temperature, and respective cycle number at which neutron data were collected are summarized in Table 7.1. For the $Ni_{29.5}Ti_{50.5}Pd_{20.0}$ specimen, similar procedures were used and are summarized in Table 7.2, with the only difference being that 190 °C was selected instead of 130 °C, to account for the difference in transformation temperatures between the two alloys. Comparable *ex situ* load-biased tests, following the same heating, cooling and mechanical loading scheme, were also carried out at NASA Glenn Research Center on these two alloys to track the strain-temperature response.

7.3 Results

Macroscopic strain-temperature curves corresponding to the aforementioned load-biased thermal cycling tests for the $Ni_{49.9}Ti_{50.1}$ and $Ni_{29.5}Ti_{50.5}Pd_{20.0}$ alloys are shown in Fig. 7.1(a) and Fig. 7.1(b), respectively. Since the response corresponding to Cycle 8 (unloading thermal cycle in the absence of an applied load) was different from other cycles, the response was re-plotted and shown separately for clarity. This is shown in Fig. 7.1(c) for NiTi and Fig. 7.1(d) for NiTiPd. In order to discern changes occurring during thermal cycling, the strain-temperature response of Cycle 2 and Cycle 7 were replotted and offset along the strain axes in order to overlap for easier comparison in both alloys. The results are reported in Fig. 7.1(e) for NiTi and Fig. 7.1(f) for

NiTiPd. Transformation strain, open-loop strain, and temperature hysteresis in the $Ni_{49.9}Ti_{50.1}$ alloy are also defined using Cycle 2 as an example, as shown in Fig. 7.1(e).

Sections of overlaid diffraction spectra from two diffraction banks, corresponding to Cycle 1 through Cycle 7, are shown in Figs. 7.2(a)-(b) for the $Ni_{49.9}Ti_{50.1}$ alloy recorded at -150 MPa/130 °C, and Figs. 7.2(c)-(d) for the $Ni_{29.5}Ti_{50.5}Pd_{20.0}$ alloy at -150 MPa/190 °C. For both alloys, only austenite was present in Cycle 1. However, the martensite phase started to appear and accumulate through additional thermal cycling under stress and temperature. In NiTi, monoclinic *B19′* martensite 100 peaks were observed in Bank 2 and 011 peaks in Bank 1. In NiTiPd, orthorhombic *B19* martensite 100 and 011 peaks were observed in both Banks at the same time. Lattice parameters of both martensite and austenite phases in the NiTi and NiTiPd alloys (under a nominal compressive holding stress of 4 MPa) were obtained by performing Rietveld refinement simultaneously on spectra from diffracting lattice planes both parallel (Bank 1) and perpendicular (Bank 2) to the loading axis. At 25 °C, the lattice parameters were determined to be a = 2.9095 Å, b = 4.6619 Å, c = 4.1306 Å and γ = 97.348° (with relative uncertainty of roughly 1 x 10^{-4} Å) for the *B19′* monoclinic martensite phase of NiTi, and a = 2.7960 Å, b = 4.6921 Å, c = 4.4234 Å for the *B19* orthorhombic martensite phase of NiTiPd. At 200 °C, the lattice parameters for the cubic austenite phase were determined to be a = 3.0306 Å for NiTi, and a = 3.0885 Å for NiTiPd. Fig. 7.2(e) and Fig. 7.2(f) illustrate the evolution of volume fraction of the retained martensite with thermal cycling, determined from the Rietveld refinement for NiTi and NiTiPd, respectively.

Texture analyses procedures used by Von Dreele [29] were adopted, to study the texture evolution in the martensitic and austenitic phases. The methodology established previously for analyzing neutron diffraction spectra in NiTi alloys [35, 36, 52, 56] was followed. A generalized spherical harmonic description [29, 30] was used to account for the evolving texture in the austenite and martensite phases. Inverse pole figures (IPFs) were calculated and plotted with generic mapping tools [34]. While pole figures show how certain specified crystallographic directions of grains are distributed in the sample reference frame, IPFs show how selected directions in the sample reference frame are distributed in the reference frame of the crystal. The input for plotting the IPFs was based on Rietveld refinement of an individual detector bank. Hence the approach enabled the texture evolution to be followed in both longitudinal and transverse directions separately.

Pole locations in monoclinic *B19′* martensitic NiTi and orthorhombic *B19* martensitic NiTiPd were identified in the IPFs and are shown in Fig. 7.3(a) and Fig. 7.3(b), respectively. The low symmetry of the monoclinic and orthorhombic lattices generated more peaks compared to the cubic structure. In order to show the pole locations more clearly, reflections corresponding to lattice planes with small d-spacings (less than 0.85 Å for NiTi and 0.65 Å for NiTiPd) were removed during refinement. Therefore, the focus of these two IPFs was to show the locations of the poles rather than the texture distribution.

Fig. 7.4, Fig. 7.5 and Fig. 7.6 show IPFs for the longitudinal direction in the room temperature *B19′* martensite phase, retained martensite and austenite phases of NiTi as a function of load-biased thermal cycling, between room temperature and 130 °C under -150 MPa, respectively.

Fig. 7.7, Fig. 7.8 and Fig. 7.9 show IPFs for the longitudinal direction in the room temperature *B19* martensite phase, retained martensite and austenite phases of NiTiPd, as a function of load-biased thermal cycling, between room temperature and 190 °C under -150 MPa, respectively.

By fitting individual diffraction peaks, lattice strains in a subset of grains of the same crystallographic orientation relative to the loading direction can be determined. The strain, ε_{hkl}, for a plane, *hkl*, at a given stress and temperature was quantified following the same approach adopted previously [35, 36, 52]. Evolution of lattice strains in the austenite phase, with cycle number and volume fraction of retained martensite, were thus obtained and are shown in Fig. 7.10(a) and Fig. 7.10(b) for NiTi, and Figs. 7.10(c) and Fig. 7.10(d) for NiTiPd. All strains reported here used Cycle 0 as the reference state and were based on the analysis of neutron spectra collected at -150 MPa/130 °C for NiTi and -150 MPa/190 °C for NiTiPd in Cycle 1 through Cycle 7, and -4 MPa/130 °C for NiTi and -4 MPa/190 °C for NiTiPd in Cycle 8.The reference state of Cycle 0 corresponds to -4 MPa/135 °C for NiTi and -4 MPa/200 °C for NiTiPd. The peak reflections correspond to lattice planes perpendicular to the loading direction and therefore the strains are along the loading direction.

7.4 Discussion

In the following sections, the changes observed in the macroscopic strain-temperature curves under load-biased thermal cycling are discussed in the context of the microstructural and micromechanical evolution of phase volume fraction, texture and strain, as determined from Rietveld refinement and single peak analyses of the acquired neutron diffraction spectra.

7.4.1 Texture and Phase Fraction Evolution

7.4.1.1 Martensite

The temperature and stress for the experiments were chosen in order to follow the retained or residual martensite build-up with successive cycles. Volume fraction of the martensite phase retained in the austenite state increased with load-biased thermal cycling for both NiTi and NiTiPd alloys, as observed in Fig. 7.2(e) and Fig. 7.2(f), respectively. However, the rate of accumulation of the retained martensite per cycle slowed down with cycling for the NiTi alloy, while this was not the case for the NiTiPd alloy. In tracking changes with each thermal cycle, higher volume fractions of retained martensite were observed in the NiTiPd alloy when compared to the NiTi alloy. For example, at Cycle 7 around 7 vol.% of martensite did not transform to austenite in NiTi, but 33 vol.% did not transform in NiTiPd.

In order to further investigate the effect of accumulation of retained martensite with thermal cycling under stress, from the macroscopic strain-temperature response of the two alloys (Fig. 7.1 and Fig. 7.2), the change in transformation strain and open-loop strain in each cycle, as a function of the cycle number, was plotted and is shown in Figs. 7.11(a)-(b). The data presented in this way helped understand the differences in the response of the two alloys.

Fig. 7.11(a) shows that NiTi had higher transformation strains than NiTiPd after one thermal cycle under stress. In our previous study [64], we showed that the texture of room temperature martensite plays an important role in determining the transformation strain. Twinning is easier and more extensive in the monoclinic *B19'* martensite (NiTi) than the orthorhombic *B19*

106

martensite (NiTiPd), thereby resulting in more transformation strain. The transformation strain continued to increase with additional thermal cycling and then did not change much after Cycle 4 for both NiTi and NiTiPd. Concomitantly, it is expected that the texture of the room temperature martensite would evolve as well in the initial cycles but would not change much after Cycle 4. This hypothesis was confirmed from the texture analyses, as shown in Fig. 7.4 for NiTi and Fig. 7.7 for NiTiPd. After the first cycle, the texture of room temperature martensite continued evolving between Cycle 1 and Cycle 4 but the evolution was small between Cycle 4 and Cycle 7. This is seen when comparing the IPFs of Cycles 1, 4 and 7 at the same stress and temperature.

As for the effect of retained martensite on the transformation strain, for NiTi after Cycle 4, the volume fraction of retained martensite did not change much when compared to prior cycles (Fig. 7.2(e)). Hence, it is not expected to influence the transformation strain. Small changes in both texture of the room temperature martensite and volume fraction of the retained martensite with cycling, therefore accounted for the small variation of the transformation strain after Cycle 4 in NiTi. For the NiTiPd alloy, however, the volume fraction of retained martensite continued increasing from about 12 vol.% in Cycle 4 to 33 vol.% in Cycle 7. It is at first surprising that this large change did not influence the evolution of the transformation strain. This can be understood by examining Fig. 7.1(f). In Cycle 7, 67 vol.% of the martensite was responsible for a 2.38% change in strain during phase transformation, while the remaining 33 vol.% of martensite only contributed a 0.28% change in strain. Hence, in NiTiPd, the majority of the strain (around 89.5%) generated during the phase transformation from martensite to austenite originated from 67 vol.% of the martensite variants that transformed first and preferentially. Even though a considerable amount of martensite is retained in the austenite phase (in this case 33 vol.% in Cycle 7), it

contributed only a portion of the strain. However, comparison of the strain-temperature response between Cycle 2 and Cycle 7 in Fig. 7.1(f) in the "fully" austenite state determined by extensometry showed differences in slope. Thus, this amount of retained martensite did influence the thermal expansion behavior in the austenite state of the NiTiPd alloy. In NiTi, the volume fraction of retained martensite did not build up as significantly as for NiTiPd with cycling. As a result, its influence on the thermal expansion response was consequently unnoticeable, as observed in Fig. 7.1(e).

Fig. 7.11(b) shows that for both alloys the open-loop strain per cycle continued decreasing with cycling from Cycle 1 to Cycle 7. Possible factors that may influence the magnitude of open-loop strain can be changes in room temperature martensite, austenite and the retained martensite if present. In case no changes occur in the above three phases with cycling, it is expected that the open-loop strain would remain unchanged. The texture evolution of the room temperature martensite slowed down between Cycle 1 and Cycle 7, as shown in Fig. 7.4 for NiTi and Fig. 7.7 for NiTiPd. This trend in texture evolution was consistent with the progression of the open-loop strain. The austenite texture, as will be shown in a later section, did not show appreciable changes with cycling. As for the retained martensite, the texture evolution represented by the IPFs in Fig. 7.5 for NiTi and Fig. 7.8 for NiTiPd, slowed down as well between Cycle 1 and Cycle 7. The decrease in the rate of the retained martensite build-up with cycling was consistent with the observed trend in open-loop strain. Thus, all the aforementioned changes provided a reasonable explanation for the gradual stabilization of the open-loop strain per cycle with cycling.

For both alloys, the initial increase in macroscopic strain at room temperature prior to thermal cycling (Cycle 0 or loading cycle), as shown in Fig. 7.1(a) and Fig. 7.1(b), was due to an applied compressive stress of 150 MPa. However, this stress did not appreciably change the texture in both alloys, as seen in Fig. 7.4 for NiTi and Fig. 7.7 for NiTiPd. Significant changes in texture occurred when the alloys were cooled to room temperature under stress. During cooling under stress, certain martensite variants are expected to preferentially form to maximize the transformation strain and satisfy the compatibility conditions. Correspondingly, there is a significant texture change as well, as seen in Fig. 7.4 and Fig. 7.7 when the two IPFs representative of Cycle 0 (starting condition) and Cycle 1 are compared. In a similar manner, the last thermal cycle (Cycle 8) was performed under a nominal compressive holding stress of 4 MPa. During heating, the phase transformation strain was generated between the already-formed preferred martensite variants (in Cycle 7) and austenite. However, during cooling, the martensite formed from the same austenite essentially under no external stress and hence attempted to return to the self-accommodated structure. Upon comparing the IPFs between Cycle 8 and the previous cycles, the texture of the room temperature martensite in Cycle 8 tended to be more like the texture observed in previous cycles (seen in Fig. 7.4 for NiTi and Fig. 7.7 for NiTiPd). The change in underlying texture resulted in a decrease in the strain during phase transformation, which macroscopically manifests as a difference in strain at the start and finish of the cycles for both alloys, as observed in Fig. 7.1(c) and Fig. 7.1(d). The correlation between texture evolution and changes in macroscopic strain is demonstrated again in this case.

During the phase transformation between the martensite and austenite phases under stress, martensite variants that provide large transformation strains are expected to preferentially form

[56]. It is thus expected that the last remaining martensite variants will be highly textured, as seen for Cycle 2 in Fig. 7.5. This texture appeared to reduce with increasing number of cycles as more retained martensite was present. For the last unloading thermal cycle (Cycle 8), less volume fraction of martensite was retained compared to Cycle 7. The texture hence increased again and the distribution was found to be similar to that observed in Cycle 4 and Cycle 5. This similarity in texture distribution is also consistent with the volume fraction of retained martensite in these three cycles, wherein around 5 vol.%, 6 vol.% and 6 vol.% of retained martensite was found to be present in Cycles 4, 5 and 8, respectively. For NiTiPd, as seen in Fig. 7.8, the texture evolves gradually and the maximum intensity in multiples of random distribution (1 corresponding to a random distribution) drops correspondingly as cycling proceeds, while larger amounts of martensite remain in the austenite state. The 100 retained martensite variants were preferentially oriented along the loading direction. It is worth mentioning that for the last unloading thermal cycle (Cycle 8) the IPF of the retained martensite changed significantly, with 001 variants being selected instead of 100 variants. This was different from NiTi in which the texture did not change abruptly when comparing the unloading thermal cycle (Cycle 8) with previous cycles, as shown in Fig. 7.5. The reason for this change is not clear. One possible explanation is that the volume fraction of the retained martensite in NiTiPd in Cycle 8 was only around 1.5 vol.%. This small volume fraction of martensite variants could be highly textured to accommodate the constraint from the rigid austenite phase as discussed earlier. Also, differences in twinning between the monoclinic and orthorhombic martensite could also possibly account for this abrupt change. Fig. 7.11(b) also shows that initially NiTi had larger open-loop strains than NiTiPd. However, after seven cycles the magnitude of the open-loop strain per cycle was comparable for the two alloys. Thus, after a finite number of cycles, NiTi can achieve

dimensional stability that is comparable to NiTiPd but can additionally provide higher transformation strains.

7.4.1.2 Austenite

For NiTi, the texture in the austenite phase did not seem to change with thermal cycling under stress, as seen in Fig. 7.6. However, it was reported previously that the texture index in the high symmetry *B2* austenite phase only varied from 1 (refers to a random polycrystalline sample) to 1.4 even when highly textured martensite was stress induced [56]. Here we note that IPFs corresponding to certain intermediate cycles are omitted in order to emphasize changes between cycles. Under compression, the intensity (normalized with respect to the austenite phase) of the regions surrounding the 111 pole increased while that of the regions surrounding the 110 pole decreased with cycling between Cycle 1 and Cycle 7. This observation is consistent with the 111 orientation being a hard orientation for compressive loading while 110 is a soft orientation [75] (in terms of the critical stress required for austenite to transform to martensite). 111 austenite grains would thus be the last to transform into martensite but the first to transform back from the martensite phase. Thus, more martensite retained with cycling implies that a relatively larger number of 111 austenite grains remain, compared with 110 grains. This is further supported by observing the evolution of the normalized intensity of austenite 110 and 111 reflections with cycling in NiTi, as shown in Fig. 7.12. The overall decrease of the intensity for the two orientations of austenite with cycling was due to the austenite to martensite phase transformation since more retained martensite formed with cycling. However, for each cycle between Cycle 1 and Cycle 7, the relative intensity of the 111 reflection was higher than that of the 110 reflection. This means that the 111 orientation was relatively harder than the 110 orientation with respect to

111

the transformation and hence the intensity of the 111 reflection changed less than that of the 110 reflection with cycling. This explanation also holds true for the last unloading thermal cycle (Cycle 8). The volume fraction of retained martensite decreased in this cycle and correspondingly the intensity of the regions surrounding the 111 pole decreased as well, with the IPFs of Cycle 8 being comparable to Cycle 3.

For NiTiPd, the starting texture of the austenite was different from that in NiTi. Upon comparing Fig. 7.9 with Fig. 7.6, 110 was the preferred direction instead of the 111 direction. Also, more noticeable changes in austenite texture occurred in NiTiPd during load-biased thermal cycling when comparing the IPFs between NiTi and NiTiPd. This increased texture evolution can be attributed to the larger volume fractions of the retained martensite present in NiTiPd. Given the correspondence between austenite and martensite, this would necessarily imply greater texture. As mentioned earlier, there was only around 1.5 vol.% of retained martensite in NiTiPd following a final thermal cycle under no load. The corresponding texture in this last unloading cycle (Cycle 8) is comparable to that of the starting cycle (Cycle 0). Thus, even though the NiTiPd alloy tended to build up more retained martensite per cycle compared to the NiTi alloy, almost all the accumulated retained martensite was converted to austenite by going through a final free-recovery thermal cycle (under no load).

7.4.2 Lattice Strain Evolution

As seen in Figs. 7.10(a)-(d), the lattice strain changes in the *B2* austenite for both alloys with thermal cycling. For both alloys, changes in lattice strains per cycle slowed down as cycling proceeded. This can be rationalized in terms of the aforementioned changes in texture as well as

phase volume fraction. Since single crystal elastic constants for austenite were only available in the literature for NiTi but not for NiTiPd, the following quantitative analysis was only done for NiTi. Elastic moduli of eight diffracting planes of *B2* austenite phase were determined using single crystal stiffness constants obtained from Refs. [50, 66, 67] and summarized in Table 7.3. The response among different reflections can be partially attributed to the lattice strain anisotropy, recognizing that 111 is the stiffest direction and 100 is the most compliant direction. Thus in the presence of an applied stress, a minimum amount of strain would be expected in the 111 direction while a maximum amount would be expected in the 100 direction. This also held true in other directions, *e.g.,* in 211 and 311, which experience lesser strains due to higher elastic moduli in the corresponding direction. It is important to note that this estimation in elastic response was purely based on a single crystal approach. Constraints in polycrystalline samples can be expected to influence the results in order to satisfy strain compatibility among various grains as well as with the retained martensite. Hence, the observed lattice strain evolution is a convoluted response due to the aforementioned factors. The retained martensite that develops with cycling appears to generate more mismatch in the intergranular stresses. This is seen from the strains diverging after Cycle 1 in Fig. 7.10(a). This behavior is more pronounced in the earlier cycles than it is in the later cycles. The reason for the increased mismatch is two-fold – first, the ability of retained martensite to accommodate strains in the austenite and second, the preferential transformation of austenite to retained martensite which was presented previously. As an example, consider the case of the behavior of 111 oriented austenite. As mentioned earlier, the 111 orientation is a hard direction (both in terms of the stress required as well as compatibility of the transformation strain) and the last to transform into martensite in compression. With the formation of retained martensite upon compressive cycling, the 111

oriented austenite experiences strains in a tensile sense. On the final no-load thermal cycle, the remaining retained martensite accommodates strain resulting in a tensile strain along the 111 direction. In Chapter Six, it was also observed that in tension, strain in the 100 direction displayed an opposite sense analogous to the 111 direction in this case. Under tension, the 100 orientation of austenite is considered a hard direction in terms of its ease to transform into martensite. The same explanation can be applied to explain that behavior as well.

From single peak analyses of strain, direction-dependent internal stresses experienced by austenite grains at -150 MPa/130 °C in Cycle 7 were determined. Given the similarities in the elastic moduli from three previous studies [50, 66, 67] as shown in Table 7.3, the stiffness constants reported in the Ref. [66] were used. Two different references were used and the results are summarized in Table 7.3. The first method compared the lattice strain evolution between Cycle 7 and Cycle 1, both at -150 MPa/130 °C, and considered the contribution of the externally applied -150 MPa before thermal cycling. This can be expressed as:

$$\sigma_{hkl}\big|_{130C,-150MPa,cycle7} = E_{hkl} \cdot \left(\varepsilon_{hkl}\big|_{130C,-150MPa,cycle7} - \varepsilon_{hkl}\big|_{130C,-150MPa,cycle1}\right) + \left(-150\right). \qquad (7.1)$$

where σ, E and ε are the *hkl* dependent stresses, elastic moduli and measured strains, respectively. The second approach directly compared the lattice strain evolution between Cycle 7 at -150 MPa/130 °C and the second "no load" training Cycle at -4 MPa/135 °C, and can be similarly expressed as

$$\sigma_{hkl}\big|_{130C,-150MPa,cycle7} = E_{hkl} \cdot \left(\varepsilon_{hkl}\big|_{130C,-150MPa,cycle7} - \varepsilon_{hkl}\big|_{135C,-3.5MPa,cycle0}\right) \qquad (7.2)$$

The two approaches give comparable results as shown in Table 7.3 and provide an estimation of the magnitude of intergranular stresses in austenite grains of different orientations as a result of load-biased thermal cycling.

For the NiTiPd alloy, the lattice strain in the 100 direction was maximum while it was minimum in the 111 direction. However, the magnitude of the strain first increased and then decreased with cycling as seen in Fig. 7.10(c). Specifically, this increase in strain occurred after Cycle 3 for 100 and Cycle 4 for 311 reflections, as seen in Figs. 7.10(c)-(d). As for the case of NiTi, the retained martensite formed initially with cycling causes more mismatch between the intergranular stresses for the same reasons presented above. However, as the volume fraction of retained martensite increases, this mismatch was accommodated resulting in a decrease in the magnitude of the intergranular strains.

7.5 Conclusions

In summary, the following conclusions were made from load-biased thermal cycling experiments in NiTi and NiTiPd shape memory alloys:

1. The texture evolution of the room temperature martensite correlated well with the evolution of the transformation strain. For both alloys, the transformation strain and the texture of the room temperature martensite remained mostly constant after the fourth cycle.

2. The retained martensite was found to have limited contribution to the transformation strain. The majority of the strain generated as a result of the phase transformation from martensite to austenite was attributed to martensite variants that transformed first and preferentially to austenite. This is particularly true for the case of NiTiPd where large volume fractions of retained martensite were observed. For example, in Cycle 7, 67 vol.% of martensite was responsible for a 2.38% change in strain during phase transformation, while the remaining 33 vol.% of martensite only contributed a 0.28% change in strain.

3. The rate of evolution of texture and volume fraction of the retained martensite, and evolution of texture of the room temperature martensite, decreased with increased cycling. This effect combined with the fact that no appreciable texture changes occurred in the austenite phase, resulted in a decrease in the magnitude of the open-loop strain per cycle.

After a finite number of cycles, NiTi can achieve higher transformation strain and similar open-loop strain when compared to NiTiPd. In actuator applications, this implies higher work output with comparable dimensional stability which facilitates easier control in NiTi. The trade off is in the lower transformation temperature for NiTi when compared to NiTiPd. However, after a final no-load thermal cycle (Cycle 8) about 6 vol.% martensite remained at 130 °C in NiTi but only about 1.5 vol.% martensite remained at 190 °C in NiTiPd. This implies that a recovery cycle could potentially reduce the amount of retained martensite accumulated with cycling thereby increasing the life of the actuator.

7.6 Tables

Table 7.1 Stress and temperature at which neutron spectra were obtained during the load-biased thermal cycling of $Ni_{49.9}Ti_{50.1}$

Stress (MPa)	Temperature (ºC)	Designation
-4	25	two no-load thermal cycles
-4	200	
-4	25	
-4	200	
-4	25	Cycle 1
-150	25	
-150	130	
-150	25	Cycle 2
-150	130	
-150	25	Cycle 3
-150	130	
-150	25	Cycle 4
-150	130	
-150	25	Cycle 5
-150	130	
-150	25	Cycle 6
-150	130	
-150	25	Cycle 7
-150	130	
-150	25	
-4	25	Cycle 8
-4	130	
-4	25	

Table 7.2 Stress and temperature at which neutron spectra were obtained during the load-biased thermal cycling of $Ni_{29.5}Ti_{50.5}Pd_{20.0}$

Stress (MPa)	Temperature (ºC)	Designation
-4	25	two no-load thermal cycles
-4	200	
-4	25	
-4	200	
-4	25	Cycle 1
-150	25	
-150	190	
-150	25	Cycle 2
-150	190	
-150	25	Cycle 3
-150	190	
-150	25	Cycle 4
-150	190	
-150	25	Cycle 5
-150	190	
-150	25	Cycle 6
-150	190	
-150	25	Cycle 7
-150	190	
-150	25	
-4	25	Cycle 8
-4	190	
-4	25	

Table 7.3 Elastic moduli and internal stresses at -150 MPa/130 °C in Cycle 7 as determined from diffracting planes of *B2* austenite in NiTi

h	k	l	E_{hkl} (GPa)			Internal stress (MPa)	
			Brill *et al.* [66]	Mercier *et al.* [67]	Wagner *et al.* [50]	Method 1	Method 2
1	0	0	49	40	45	-269.4	-305.2
1	1	0	76	71	81	-239.8	-234.4
1	1	1	93	97	110	-11.6	9.6
2	1	0	63	56	63	-240.0	-246.1
2	1	1	76	81	71	-156.6	-141.7
3	1	1	63	62	55	-232.8	-242.5
3	2	0	70	72	64	-235.0	-223.4
3	2	1	76	81	71	-252.9	-246.0
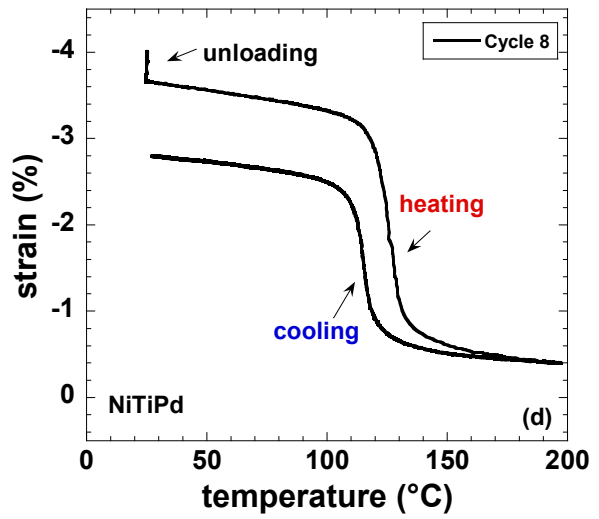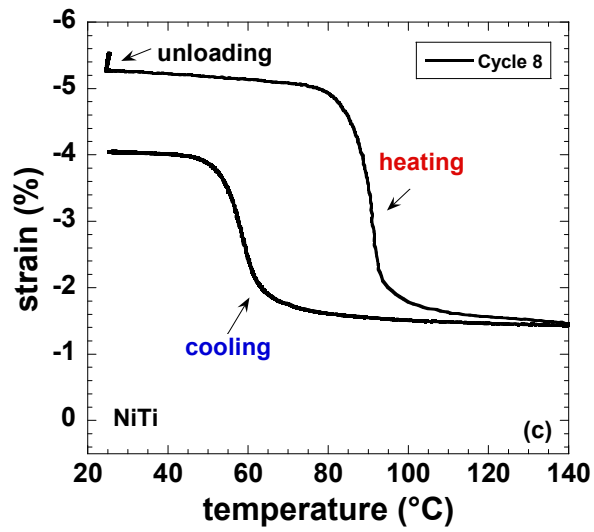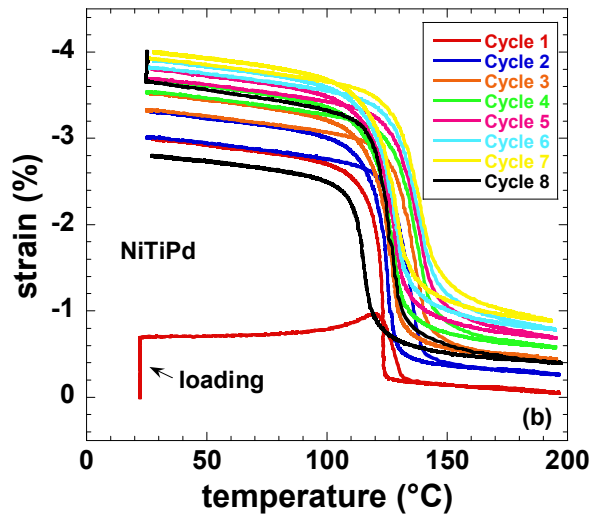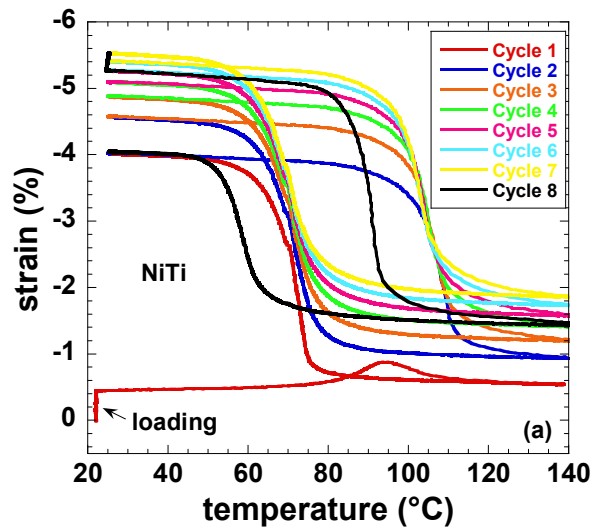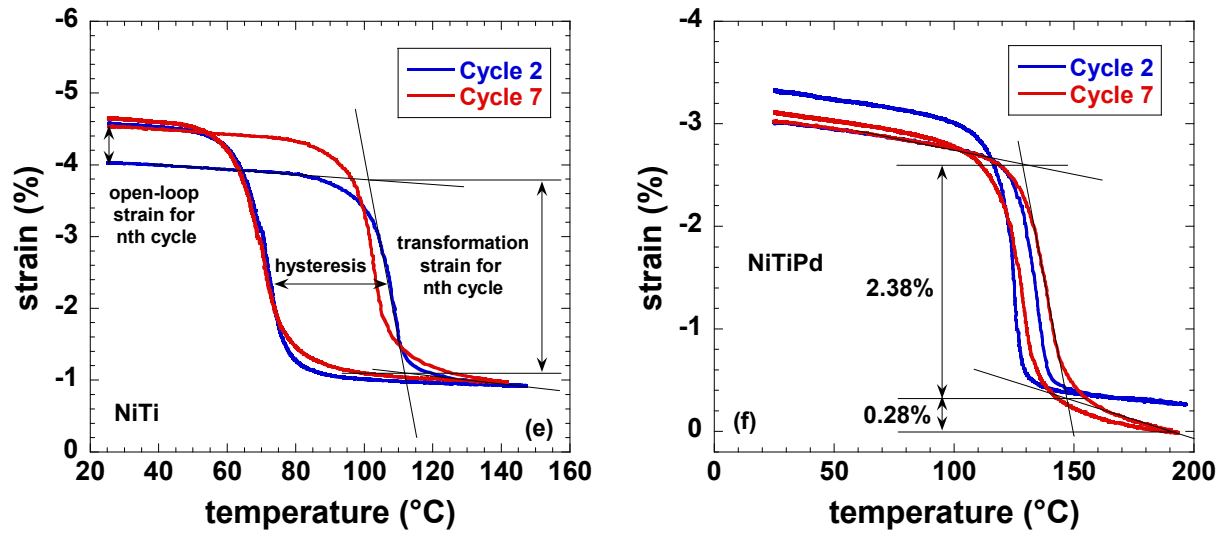
Figure 7.1 Macroscopic strain-temperature response of load-biased thermal cycling tests in (a) $Ni_{49.9}Ti_{50.1}$, and (b) $Ni_{29.5}Ti_{50.5}Pd_{20.0}$ alloys, at a compressive stress of 150 MPa. After unloading, the strain-temperature response in Cycle 8 was plotted separately for (c) NiTi and (d) NiTiPd. The response from Cycle 2 and Cycle 7 were off-set for (e) $Ni_{49.9}Ti_{50.1}$, and (f) $Ni_{29.5}Ti_{50.5}Pd_{20.0}$, for easier comparison.
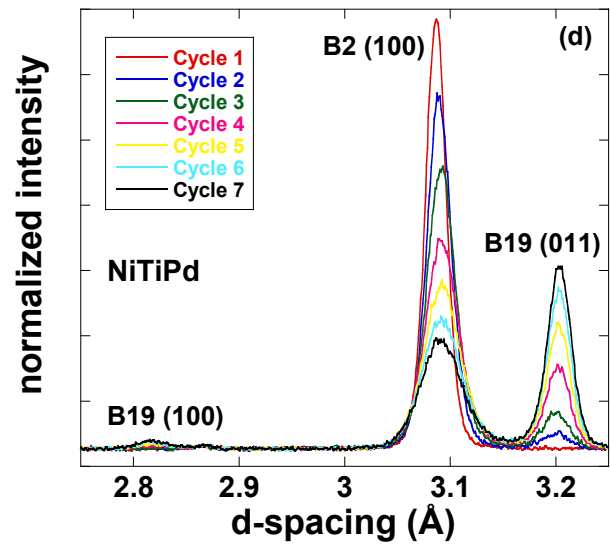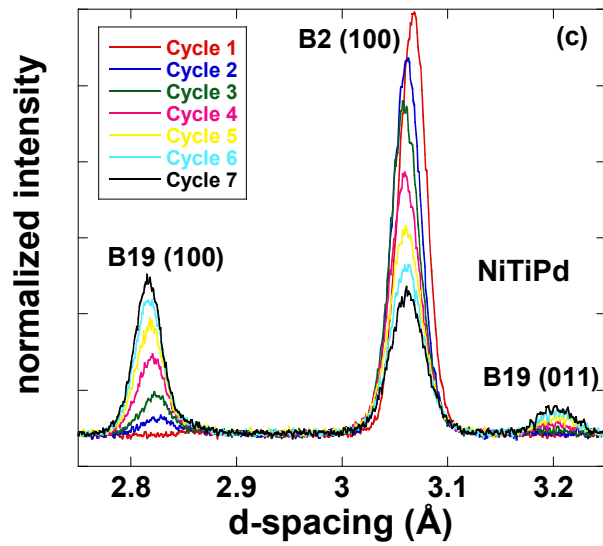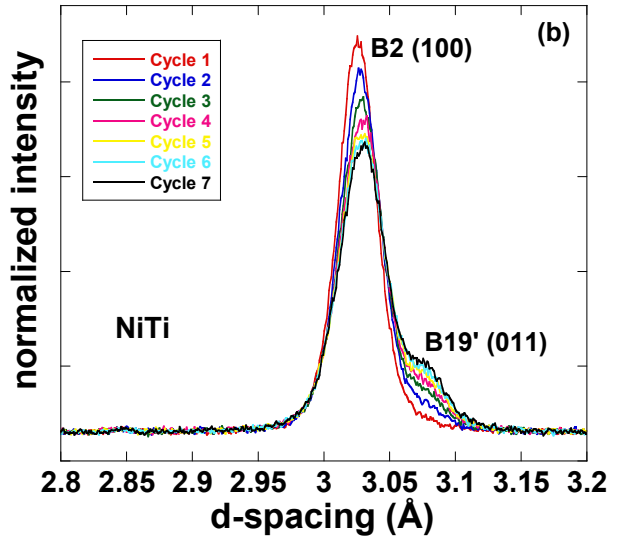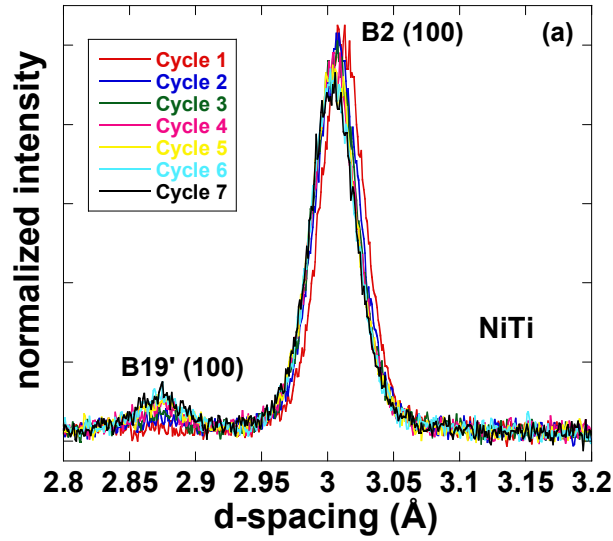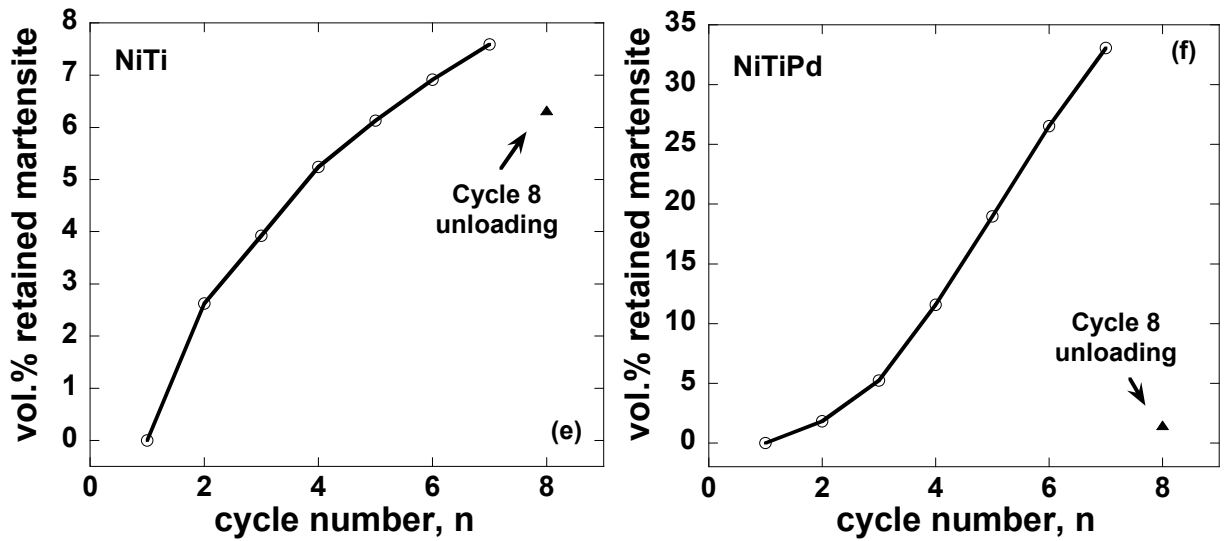
Figure 7.2 Sections of normalized neutron diffraction spectra recorded with cycling in (a) and (b) for $Ni_{49.9}Ti_{50.1}$ at -150 MPa/130 °C, and (c) and (d) for $Ni_{29.5}Ti_{50.5}Pd_{20.0}$ at -150 MPa/190 °C. The spectra overlayed here are from diffracting lattice planes perpendicular (Bank 2) in (a) and (c), and parallel (Bank 1) in (b) and (d) to the loading axis. The volume fraction of the retained martensite determined by Rietveld refinement as a function of cycle number for $Ni_{49.9}Ti_{50.1}$ and $Ni_{29.5}Ti_{50.5}Pd_{20.0}$ alloys are shown in (e) and (f) show, respectively.
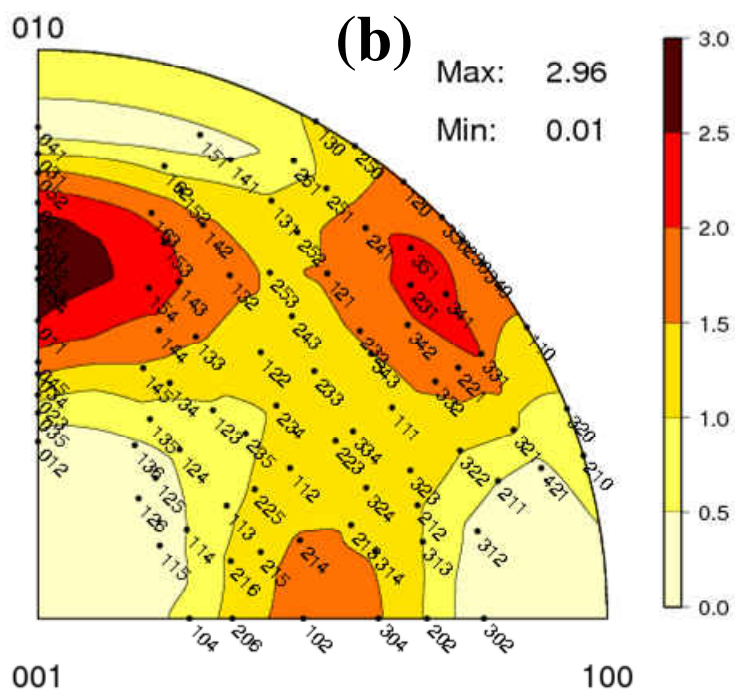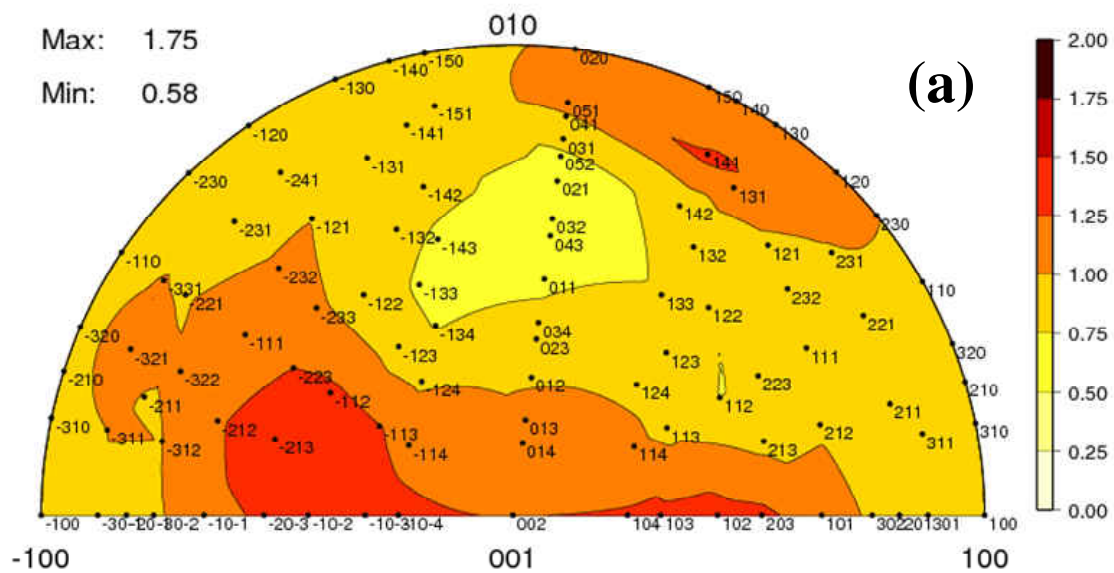
Figure 7.3 Pole locations for (a) monoclinic *B19′* martensite phase in NiTi and (b) orthorhombic *B19* martensite phase in NiTiPd
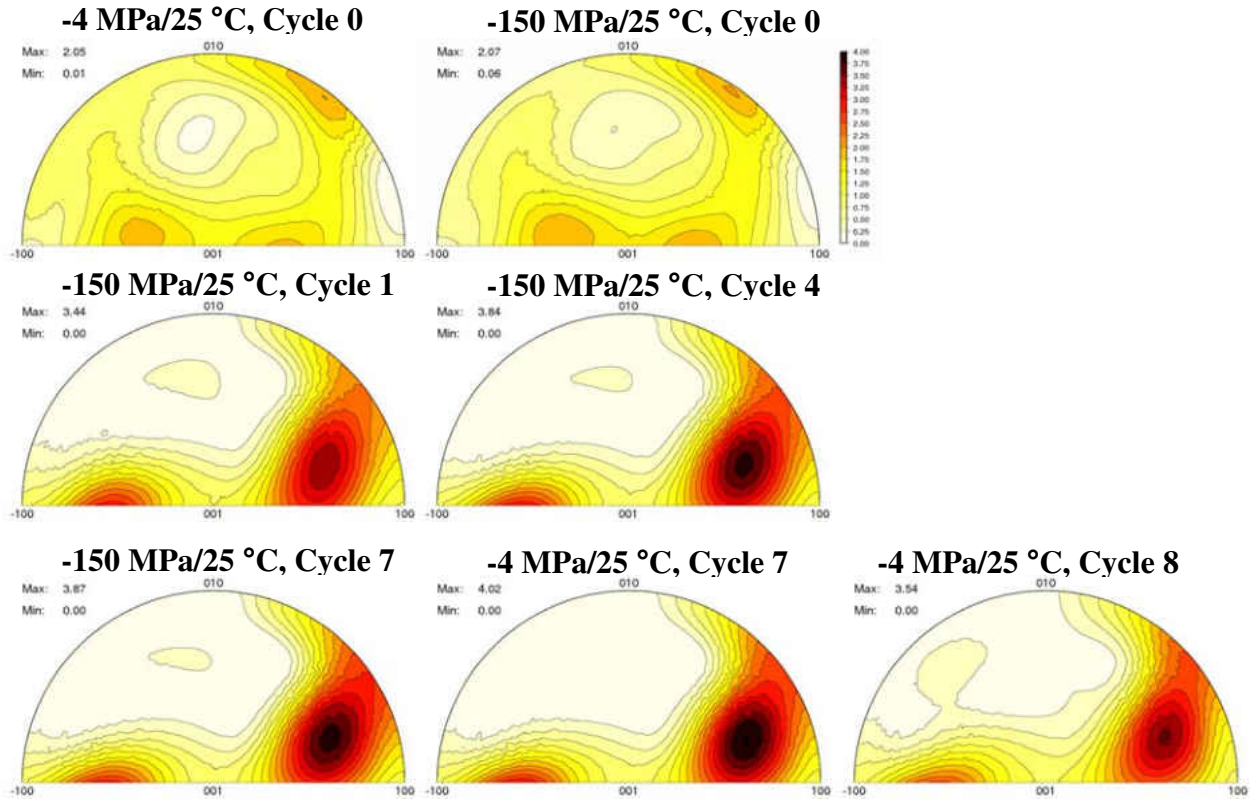
Figure 7.4 Inverse pole figures (IPFs) for the longitudinal direction in room temperature *B19′* martensite phase as a function of thermal cycling showing texture in $Ni_{49.9}Ti_{50.1}$. The top left hand corner also indicates the respective maximum and minimum intensities observed in the given IPF, in multiples of random distribution (1 corresponding to a random distribution). The stress/temperature combinations at which the raw spectra were collected are indicated in each figure as well.

-150 MPa/130 °C, Cycle 2

Max: 24.53
Min: 0.00

-150 MPa/130 °C, Cycle 3

Max: 14.78
Min: 0.00

-150 MPa/130 °C, Cycle 4

Max: 12.66
Min: 0.00

-150 MPa/130 °C, Cycle 5

Max: 9.73
Min: 0.00

-150 MPa/130 °C, Cycle 7

Max: 9.69
Min: 0.00

-4 MPa/130 °C, Cycle 8

Max: 11.32
Min: 0.01
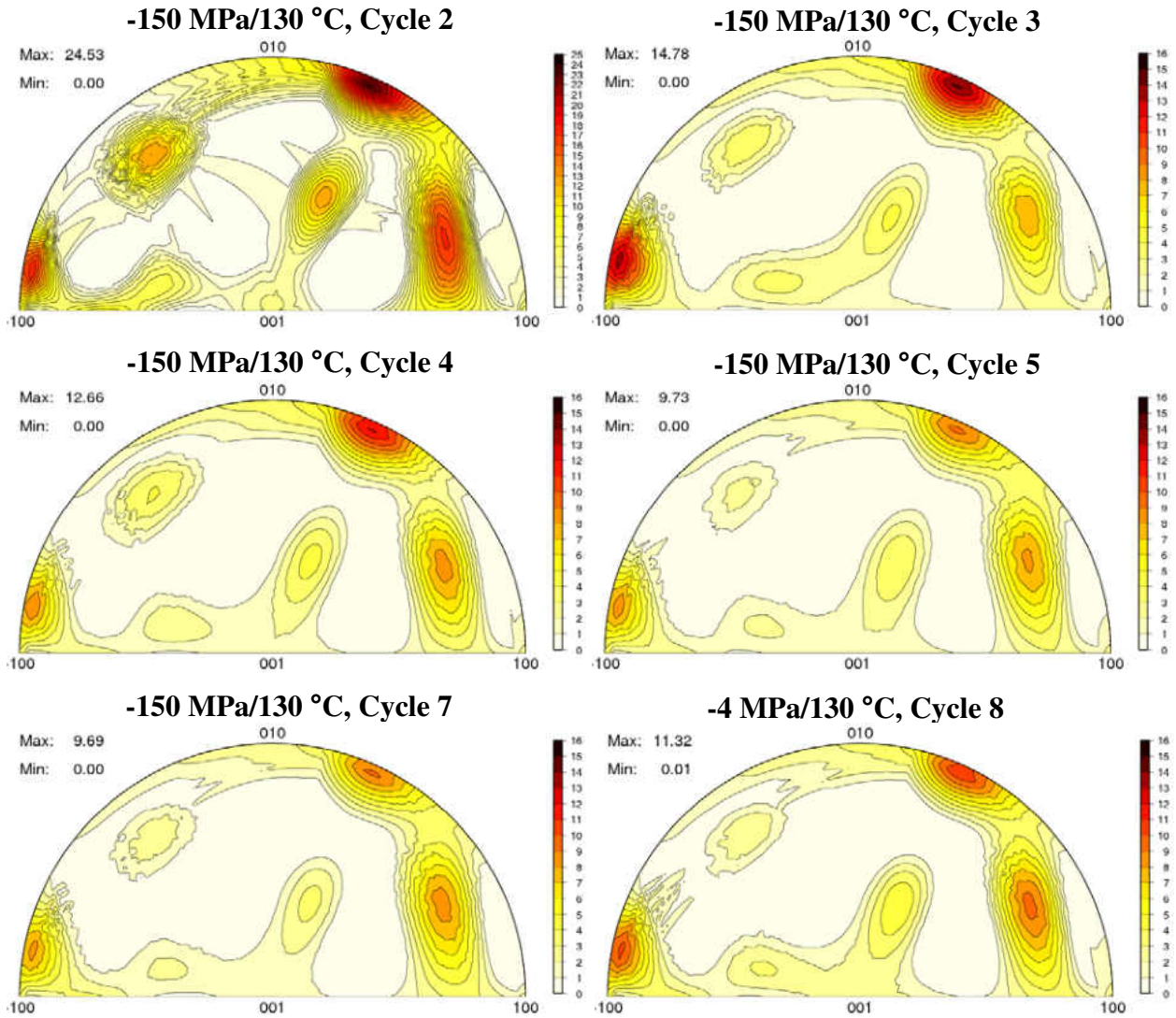
Figure 7.5 Inverse pole figures (IPFs) for the longitudinal direction in retained *B19'* martensite phase as a function of thermal cycling showing texture in $Ni_{49.9}Ti_{50.1}$. The top left hand corner also indicates the respective maximum and minimum intensities observed in the given IPF, in multiples of random distribution (1 corresponding to a random distribution). The stress/temperature combinations at which the raw spectra were collected are indicated in each figure as well.

-4 MPa/135 °C, Cycle 0   **-150 MPa/130 °C, Cycle 1**   **-150 MPa/130 °C, Cycle 3**

-150 MPa/130 °C, Cycle 5   **-150 MPa/130 °C, Cycle 7**   **-4 MPa/130 °C, Cycle 8**
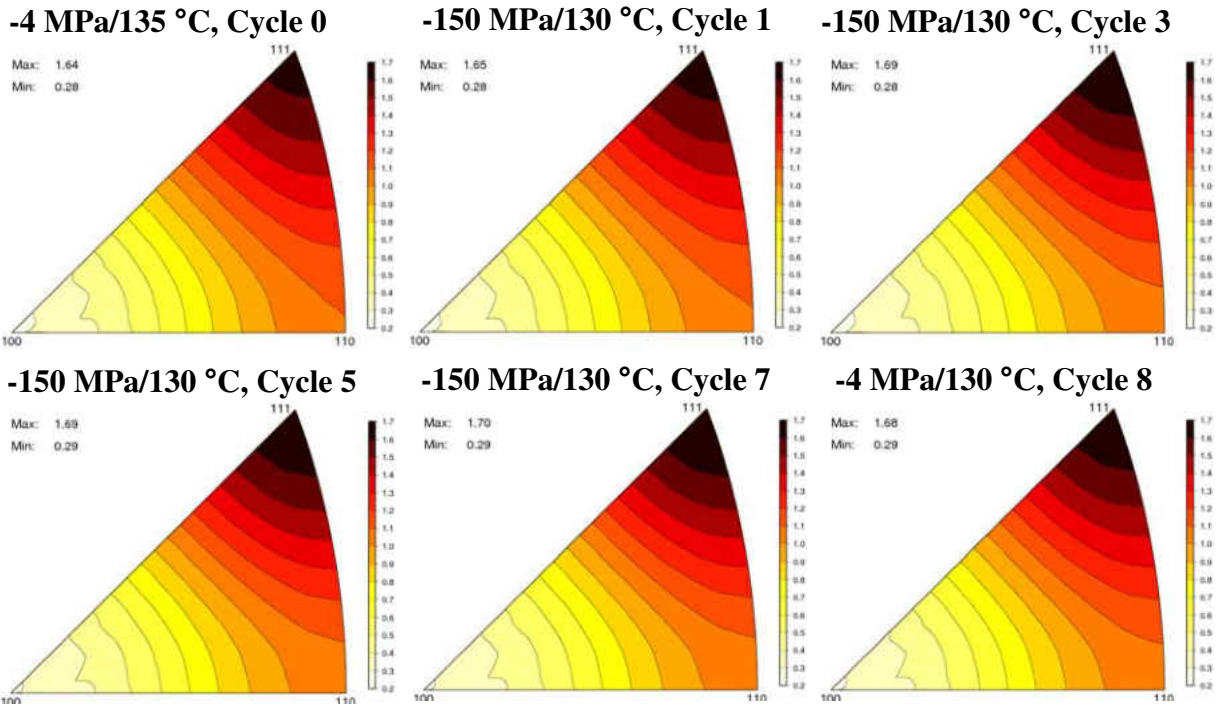
Figure 7.6 Inverse pole figures (IPFs) for the longitudinal direction in *B2* austenite phase as a function of thermal cycling showing texture in $Ni_{49.9}Ti_{50.1}$. The top left hand corner also indicates the respective maximum and minimum intensities observed in the given IPF, in multiples of random distribution (1 corresponding to a random distribution). The stress/temperature combinations at which the raw spectra were collected are indicated in each figure as well.

-4 MPa/25 °C, Cycle 0 **-150 MPa/25 °C, Cycle 0** **-150 MPa/25 °C, Cycle 1** **-150 MPa/25 °C, Cycle 4**

-150 MPa/25 °C, Cycle 7 **-4 MPa/25 °C, Cycle 7** **-4 MPa/25 °C, Cycle 8**
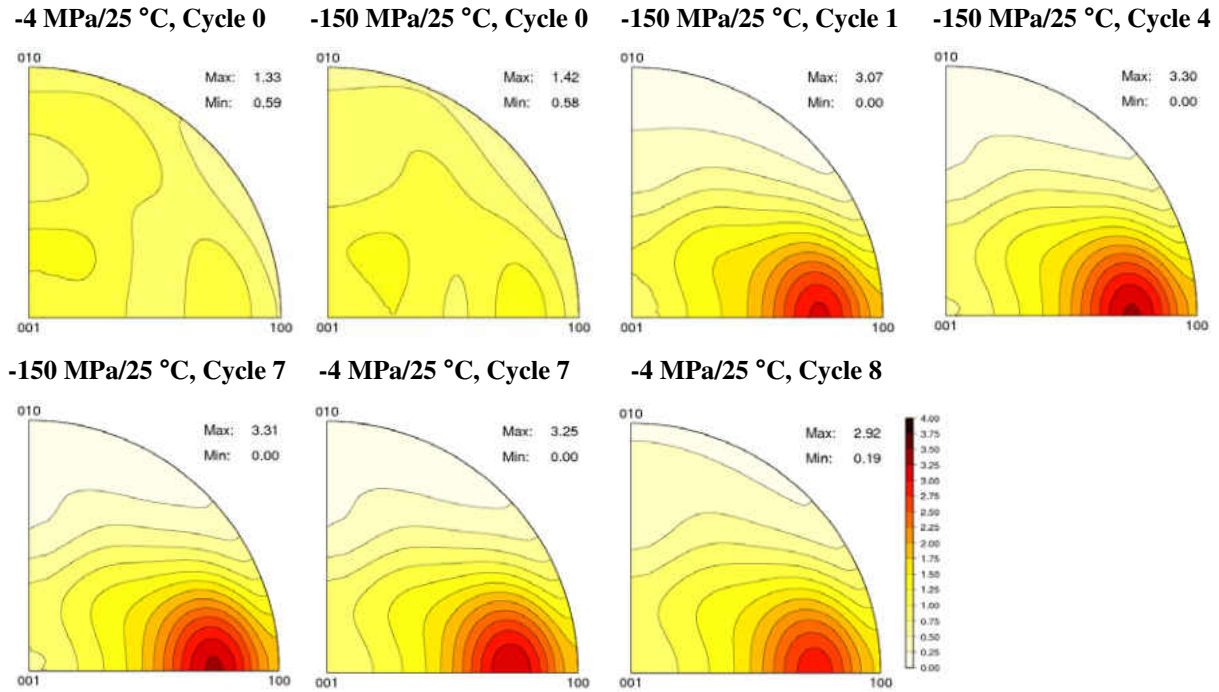
Figure 7.7 Inverse pole figures (IPFs) for the longitudinal direction in room temperature *B19* martensite phase as a function of thermal cycling, showing texture in $Ni_{29.5}Ti_{50.5}Pd_{20.0}$. The top left hand corner also indicates the respective maximum and minimum intensities observed in the given IPF, in multiples of random distribution (1 corresponding to a random distribution). The stress/temperature combinations at which the raw spectra were collected are indicated in each figure as well.

-150 MPa/190 °C, Cycle 3   **-150 MPa/190 °C, Cycle 5**

-150 MPa/190 °C, Cycle 7   **-4 MPa/190 °C, Cycle 8**
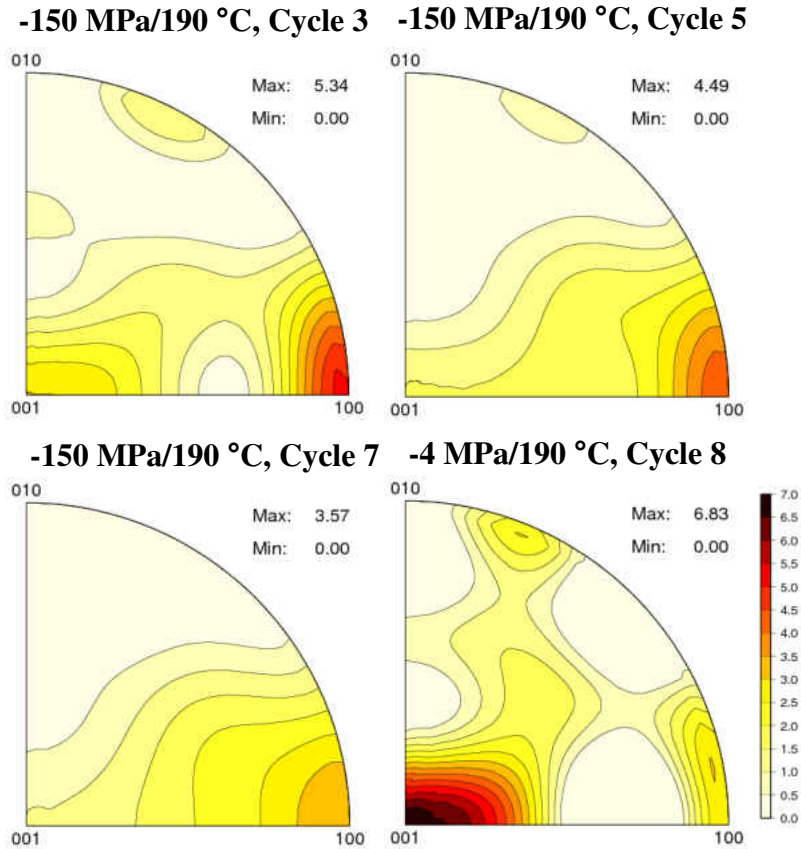
Figure 7.8 Inverse pole figures (IPFs) for the longitudinal direction in retained *B19* martensite phase as a function of thermal cycling, showing texture in $Ni_{29.5}Ti_{50.5}Pd_{20.0}$. The top left hand corner also indicates the respective maximum and minimum intensities observed in the given IPF, in multiples of random distribution (1 corresponding to a random distribution). The stress/temperature combinations at which the raw spectra were collected are indicated in each figure as well.

-4 MPa/200 °C, Cycle 0　　**-150 MPa/190 °C, Cycle 1**　　**-150 MPa/190 °C, Cycle 3**

-150 MPa/190 °C, Cycle 5　　**-150 MPa/190 °C, Cycle 7**　　**-4 MPa/190 °C, Cycle 8**
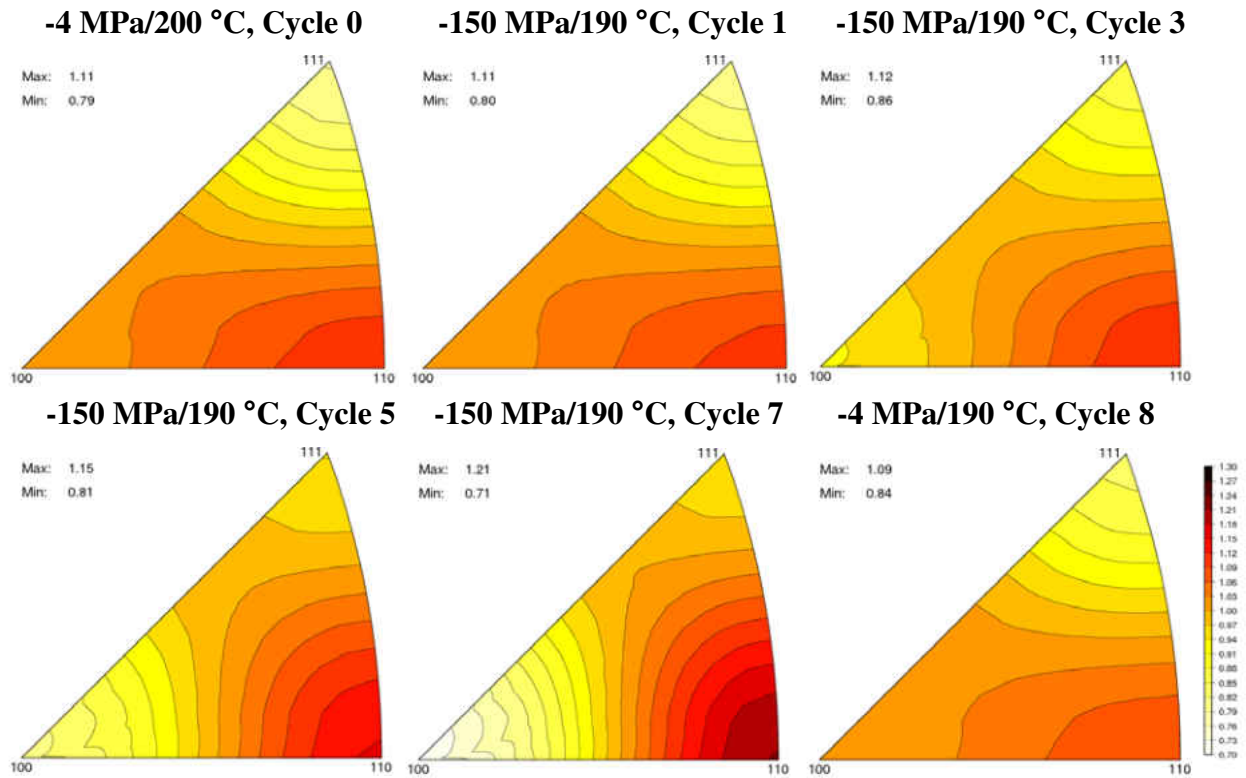
Figure 7.9 Inverse pole figures (IPFs) for the longitudinal direction in *B2* austenite phase as a function of thermal cycling showing texture in $Ni_{29.5}Ti_{50.5}Pd_{20.0}$. The top left hand corner also indicates the respective maximum and minimum intensities observed in the given IPF, in multiples of random distribution (1 corresponding to a random distribution). The stress/temperature combinations at which the raw spectra were collected are indicated in each figure as well.

130
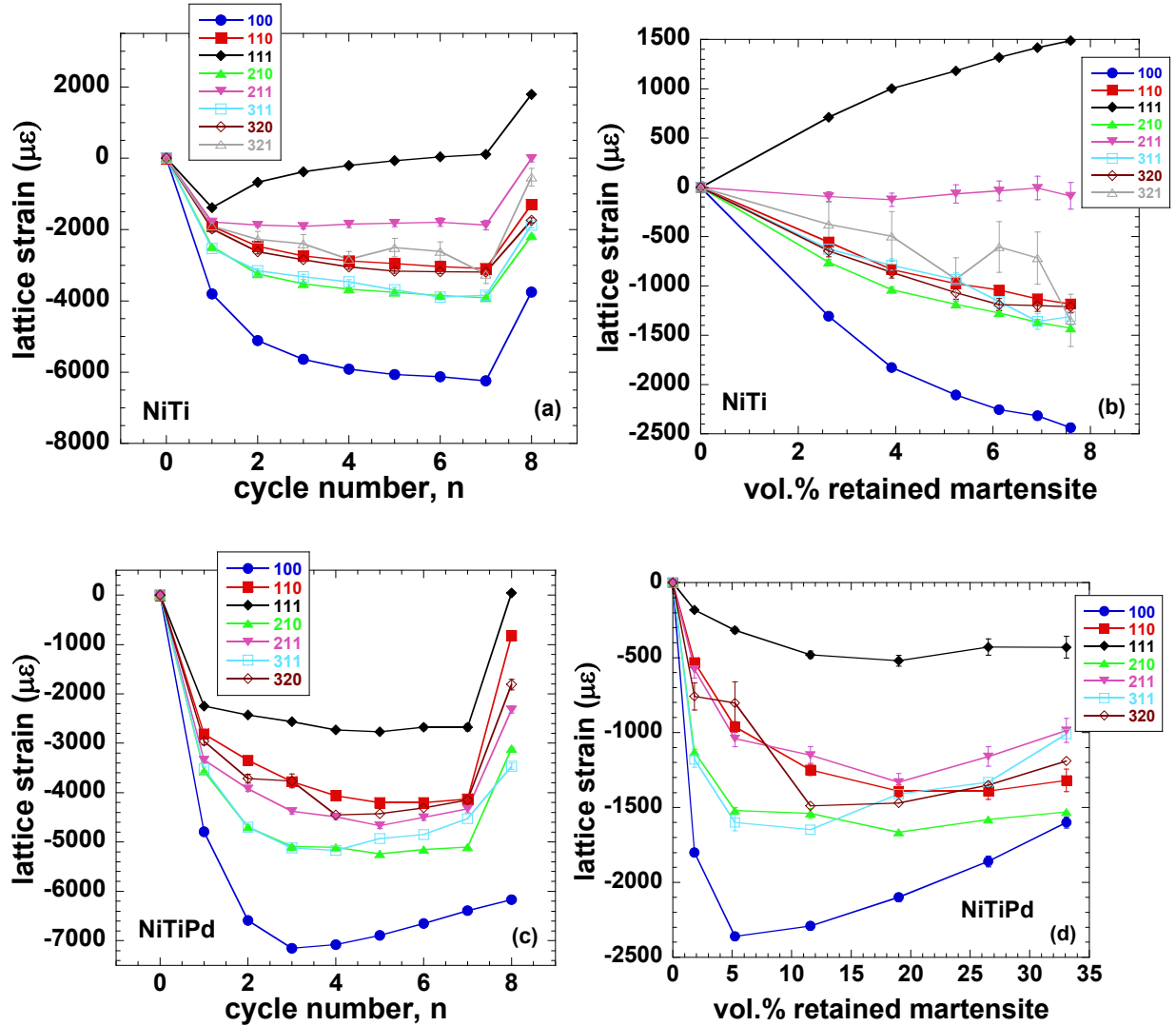
Figure 7.10 Lattice strain evolution in the austenite phase with cycling and volume fraction of retained martensite: (a) and (b) for $Ni_{49.9}Ti_{50.1}$, and (c) and (d) for $Ni_{29.5}Ti_{50.5}Pd_{20.0}$. All strains reported here are along the loading direction and were obtained with the following reference states: -4 MPa/135 °C for NiTi and -4 MPa/200 °C for NiTiPd. Neutron spectra were collected at -150 MPa/130 °C for NiTi and -150 MPa/190 °C for NiTiPd in Cycle 1 through Cycle 7, and -4 MPa/130 °C for NiTi and -4 MPa/190 °C for NiTiPd in Cycle 8.
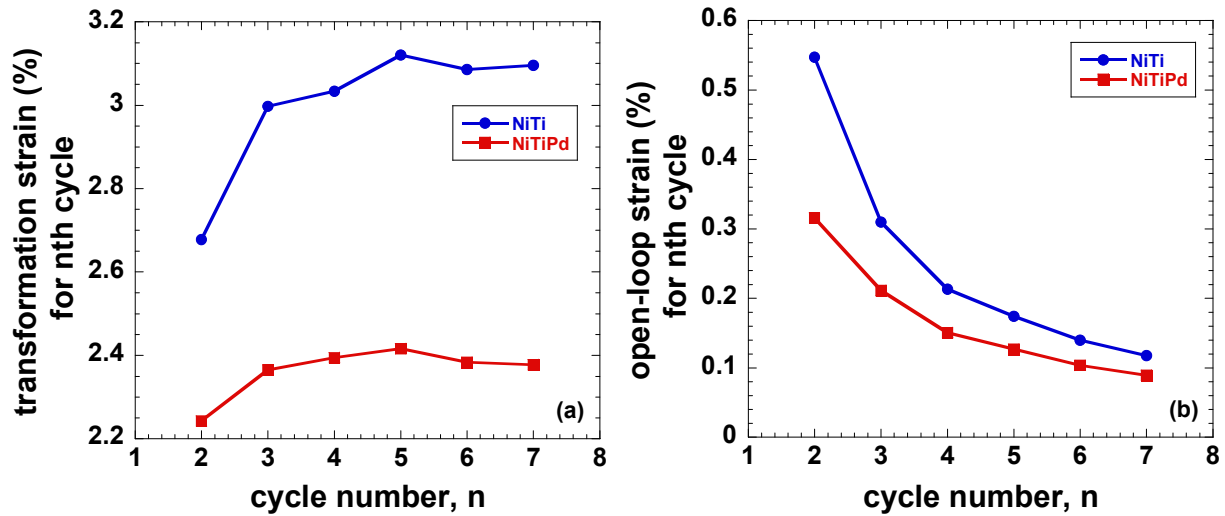
Figure 7.11 Evolution of (a) transformation strain, and (b) open-loop strain as a function of cycle number, during load-biased thermal cycling in both $Ni_{49.9}Ti_{50.1}$ and $Ni_{29.5}Ti_{50.5}Pd_{20.0}$ alloys.
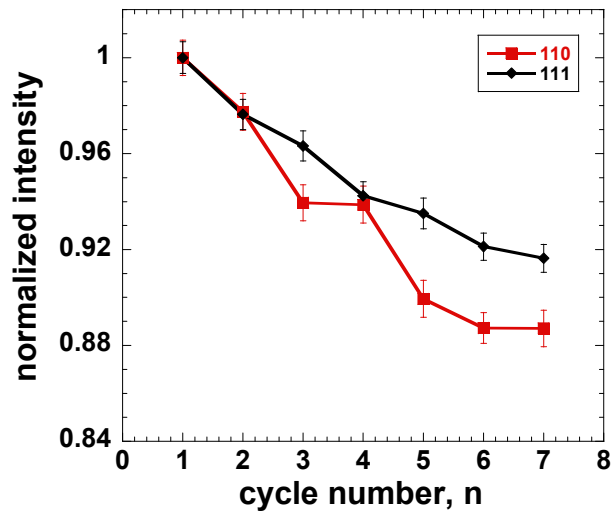
Figure 7.12 Evolution of the normalized intensity of austenite 110 and 111 reflections with cycling in $Ni_{49.9}Ti_{50.1}$. All data reported here were obtained based on the analysis of neutron spectra recorded at -150 MPa/130 °C (except for Cycle 8, which was at -4 MPa/130 °C), using Cycle 1 as the reference state. The data shown here are from diffracting lattice planes perpendicular to the loading axis.

CHAPTER EIGHT: HARD AND EASY DIRECTIONS IN AUSTENITE DURING PHASE TRANSFORMATION

The preference for transformation among 100, 110 and 111 austenite orientations was examined from in situ neutron diffraction measurements during monotonic tension and compression in superelastic NiTi. Theoretical phase transformation strains of the 12 lattice correspondence variants of martensite that are allowed to form from crystallographic symmetry and variant conversion strains (corresponding to (11-1) Type 1 twinning) were determined following a previously established methodology. The preference for transformation observed in this study and the computed strains are consistent with results from compression testing of micron-scaled single crystal NiTi pillars. The transformation sequence observed is also used to support observations of strain evolution in austenite during thermo-mechanical cycling and while assessing the role of the upper cycle temperature during transformation under load.

8.1 Hard and Easy Directions in Austenite during Phase Transformation

From the results shown in previous chapters, the lattice strain evolution of certain hard orientations in austenite seemed to display an opposite sense compared with the rest of the orientations, *e.g.,* 111 orientation in Chapter Seven (effect of thermo-mechanical cycling) and 100 orientation in Chapter Six (effect of upper cycle temperature). To shed light on those observed behaviors, the dependence of the phase transformation on *B2* orientation was studied by *in situ* neutron diffraction during uniaxial loading of superelastic polycrystalline NiTi in both compression and tension.

Cylindrical specimens of $Ni_{50.9}Ti_{49.1}$, 6.35 mm in diameter and 19.05 mm in gauge length, with threaded ends were fabricated by electrical discharge and conventional machining. *In situ* neutron diffraction measurements were performed in "time-of-flight" mode on the Spectrometer for MAterials Research at Temperature and Stress (SMARTS) at Los Alamos National Laboratory (LANL). At room temperature, samples were separately tested in compression and tension, with the crosshead displacement rate being $\pm$ 0.2 mm min^{-1}, while neutron diffraction spectra were simultaneously acquired at selected stresses.

Figs. 8.1(a)-(c) show three sections of neutron diffraction spectra corresponding to 111, 101 and 100 reflections at various stresses during compressive loading. The three peaks each originated from a subset of grains of the same crystallographic orientation with their 111, 101and 100 planes aligned perpendicular to the loading direction, respectively. The spectra are normalized so that 111 peaks have the same intensities at various stresses. Thus the intensity changes in the other two peaks are indicative of the ease or difficulty of transformation. Preferred reduction in intensity of the 100 peaks with increasing stress implies a preferential transformation of 100 oriented grains compared to 101 and 111 oriented grains. The transformation sequence from austenite to martensite thus observed is a preference for 100 oriented grains, followed by 101 grains and lastly by 111 oriented grains.

Neutron diffraction studies were further extended to investigate the effect of orientation in tension to compare to the results just presented for compression. Figs. 8.2(a)-(c) show three sections of neutron diffraction spectra corresponding to 100, 101 and 111 reflections at various stresses during tensile loading. Previously, it was predicted that the 100 direction is a hard

direction in tension [75]. Hence, the spectra are normalized so that 100 peaks have the same intensities at various stresses. While the 100 intensity remained unchanged with stress as a result of the normalization procedure, both 110 and 111 austenite orientations showed reductions in intensity. This experimental observation hence is consistent with the aforementioned prediction that the 100 direction is relatively difficult to transform during tension when compared to the other orientations. However, it was not straightforward to determine the order of the transformation sequence of the 110 and 111 directions. From 320 MPa to 370 MPa a preferential transformation of 111 oriented grains were observed when compared to 110 oriented grains. However, upon increasing the stress to 410 MPa, the intensity of the 111 reflections did not change while that of the 110 peaks continued to decrease. This indicated that grains of 110 orientation transform preferentially at higher stresses compared to those of 111 orientation. The similarity of the predicted maximum uniaxial resolved shear stress factor for phase transformation in tension in the Ref. [75], 0.41 for 110 orientation and 0.39 for 111 orientation, could also be responsible for the observed behavior. The predicted maximum resolved shear stress factor for 100 orientation is 0.21 which points to the fact that the highest stress is required to induce the austenite to martensite phase transformation in the 100 direction when compared to the other two directions.

8.2 Crystallography of the *B2* to *B19'* Transformation

Crystallography of the *B2* to *B19'* phase transformation is presented in this section, to provide the background for calculating the austenite to martensite transformation strain and martensite variant conversion strains. There is a unique lattice correspondence between the austenite *B2*

(CsCl structure) and the martensite *B19′* (2H structure) phases during the stress-induced phase transformation in NiTi. The lattice correspondence has been shown to be of the type [76, 77]:

$$(001)_{B19'} // (011)_{B2}, [\bar{1}10]_{B19'} // [\bar{1}\bar{1}1]_{B2} \qquad (8.1)$$

Only 12 crystallographically different correspondence variants are available to satisfy this relationship, as summarized in Table 8.1 [4]. Each variant yields two crystallographically equivalent habit plane variants, thus a total of 24 habit plane variants are available. Fig. 8.3 shows a schematic of the lattice correspondence between the *B2* (in black) and *B19′* (in red) unit cells for variant 1. There are two mathematically equivalent conventions for labeling the lattice vectors in the *B19′* phase. Either b is along the diad axis, so that β is the monoclinic angle; or c is along the diad axis, which makes γ the monoclinic angle. It is worth mentioning that during the formation of the *B19′* phase, the monoclinic angle is chosen to be between the lattice vectors with minimum and maximum lengths, and the lattice vector with the medium length is the diad axis. For the following transformation and conversion strain calculations, we choose b to be along the diad axis and β to be the monoclinic angle for consistency with the literature [4]. However, due to the choice of axes in the Rietveld refinement program, all the output planes and directions, *e.g.,* in inverse pole figures and axial distribution plots, use a combination of c and γ instead. This choice of axes can be found in [65] and [78].

8.3 Theoretical Determination of Transformation and Variant Conversion Strains

Following the methodology adopted in [79], strains associated with the austenite transforming to a particular martensite variant along a specific direction can be determined. The case of the phase transformation to martensite variant 1 is used as an example to explain the procedure for the

transformation strain calculation. The austenite to martensite phase transformation can be described as a combination of rotation (R), distortion (D) and shear (S). The rotation (R) operation is to align the principal axes of the *B19′* phase with the principal axes of the *B2* phase, following the lattice correspondence relationship summarized in Table 8.1 for each martensite variant. For example, Fig. 8.3 shows the relationship between the austenite and martensite lattice for variant 1, in which $[100]_M//[100]_{B2}$, $[010]_M//[011]_{B2}$ and $[001]_M//[0\text{-}11]_{B2}$. During this step, no lattice deformation takes place in the *B19′* phase. Upon transformation, 100_{B2} and 011_{B2} vectors shrink to become a and b, respectively, while $0\text{-}11_{B2}$ expands to become the c axis of the martensite phase. This is the distortion (D). The shear (S) operation is then introduced to change the angle from 90° on the $0\text{-}11_{B2}$ plane in the 100_{B2} direction. Thus the final monoclinic lattice is created. The transformation process was broken down into the aforementioned steps merely for mathematical clarity. The deformation matrix (G) is defined as the product of distortion (D) and shear (S) and is given by:

$$G = \begin{bmatrix} \dfrac{a}{d_{100,B2}} & 0 & \dfrac{-c\sin\theta}{2d_{110,B2}} \\ 0 & \dfrac{b}{2d_{110,B2}} & 0 \\ 0 & 0 & \dfrac{c\cos\theta}{2d_{110,B2}} \end{bmatrix}, \tag{8.2}$$

in which a, b and c are the lattice parameters of the martensite phase with θ being the difference between β and 90°. $d_{100,B2}$ and $d_{110,B2}$ are the interplanar d-spacings of the 100 and 110 planes in the *B2* austenite phase, respectively. Thus the transformation strain along any arbitrary direction hkl in the austenite *B2* phase during the phase transformation to a martensite *B19′* variant can be determined by:

$$\varepsilon_{hkl}^{\mathrm{var}} = \frac{\left|R \cdot G \cdot R^{-1} \cdot v\right|}{|v|} - 1 \tag{8.3}$$

where R is the rotation matrix and $v = \begin{pmatrix} h \\ k \\ l \end{pmatrix}$.

Details of the calculations of the transformation strain are provided in Appendix A, using variant 1 as an example.

While the transformation strain refers to strain associated with the austenite-martensite phase transformation, the variant conversion strain refers to the strain between two martensite variants. The variant conversion process can happen in the superelastic case when additional stress is applied in the stress-induced martensite phase. Similarly, variant conversion in the shape memory case occurs when the martensite phase is directly loaded. After the transformation strains are obtained for all the martensite variants in the three major directions, the variant conversion strains are calculated for the combinations permitted by the possible twinning mode.

Considering (11-1) type I twinning, as identified previously by neutron diffraction studies [52, 56, 65], only 12 possibilities of the martensite variant conversions are permitted. The transformation strains associated with austenite transforming to martensite as well as martensite variant conversion strains along the 111_{B2}, 101_{B2} and 100_{B2} directions are therefore calculated accordingly and reported in Table 8.2. The lattice parameters used for calculating the strains are: a=3.0010 Å for austenite, and a = 2.8759 Å, b = 4.1531 Å, c = 4.5515 Å and β = 94.91° for martensite (with relative uncertainty of roughly 1 x 10^{-4} Å), as determined from Rietveld refinement of neutron spectra on the material of the same composition used in the

aforementioned measurements shown in Fig. 8.1 and Fig. 8.2. As a result of (11-1) type I twinning, variants 1, 1', 2, 2', 3, 3', 4 and 4' are expected to form. Variant conversion strains corresponding to these possibilities are hence calculated and summarized in Table 8.2 with respect to the three major orientations of the austenite lattice.

8.4 Application of Theory to Experiments

8.4.1 Compression Experiments on Micron-Scaled Single Crystal NiTi Pillars

Micro-compression experiments on single crystal micron-scaled pillars of known orientations were performed to compare with the predictions of easy and hard directions (in terms of the propensity for phase transformation from austenite to martensite) from neutron measurements. The objective was to also compare the experiments with the theoretically determined transformation strains. Information on the sample preparation and experimental procedure can be found in more detail in Ref. [80] and is only summarized here. $Ni_{50.9}Ti_{49.1}$ was fabricated by vacuum induction melting followed by a vacuum arc re-melting process. Select grains (average grain size approx. 30 µm) with 101 and 111 orientations in the austenitic state were identified using electron back scattered diffraction (EBSD). Cylindrical micro-pillars were prepared using an FEI 200 TEM Focused Ion Beam (FIB) instrument. The diameter and height for the 101 oriented pillar was 12.6 µm and 26.4 µm; for the 111 oriented pillar, 9.4 µm and 31.4 µm, respectively. The micro-compression studies were performed using an instrumented Hysitron Triboindenter at the Center for Integrated Nanotechnologies (CINT) at LANL. A 30 µm diameter flat diamond punch was used as the compression platen.

Using a 0.2% strain offset technique (similar to what is traditionally done in elastic-plastic response in materials to measure the yield stress) the onset stresses for inducing the martensite phase from the austenite phase were determined to be 502 MPa and 206 MPa (both in compression), for the 111 and 101 orientation, respectively. The results shown in Figs. 8.4(a)-(b) indicate that the critical stress in compression required for inducing the phase transformation is higher in the 111 orientation, compared to the 101 orientation. Thus, the 111 orientation is relatively harder than the 101 orientation, in terms of the stress required for inducing the phase transformation. This is consistent with the aforementioned results from the neutron diffraction measurements where the 111 orientation was shown to be a hard direction compared to the 101 orientation in compression. This orientation dependence of the sequence of the phase transformation can be attributed to the preferential selection and formation of martensite correspondent variant pairs (CVPs) along the individual orientations [81]. It is worth noting that we should pay attention to the potential issues in comparing single crystals (micro-compression testing) with a polycrystalline specimen (neutron diffraction testing). In our previous studies, we have successfully assessed the role of grain-scale intergranular stresses in the polycrystalline bulk response [52]. Moreover, owing to the strong texture evolution of the martensite phase and the ability of these alloys to accommodate mismatch by variant conversion/reorientation, detwinning, and stress-induced transformation, such comparisons are still valid. The results are also consistent with previous studies, which established that the 111 direction in austenite is hard to induce the phase transformation in compression [75, 82, 83].

Fig. 8.4(a) shows the macroscopic stress-strain response for the 111 oriented pillar up to 1480 MPa. Elastic deformation of the stress-induced martensite phase was observed, after the stress-

induced phase transformation was complete. Consequently, the applied stress was hence high enough for variant conversion to 1, 1' and 4. The austenite to martensite phase transformation in these three variants all produced -2.8% in strain, from Table 8.2. The phase transformation strain along the 111 orientation was determined to be -2.1%, by using a 0.2% strain offset from the elastic stress-strain responses of austenite and martensite in Fig. 8.4(a). The difference can be attributed to Ni_4Ti_3 precipitates available in the austenite matrix, which do not generate recoverable strains. A similar determination for the 101 oriented pillar results in conversion to variants 1, 2', 4 and 4' which generate strains of -3.9%, -3.9%, -2.1% and -2.1%, respectively. From Fig. 8.4(b), the strain associated with the phase transformation of the 101 oriented pillar is -0.9%, which is lower than any of the theoretical estimates. Given the fact that more possible combinations of the resultant variants are available for the 101 orientation compared to the 111 orientation, and the difference in the magnitude of the strain may be attributed to the need to satisfy compatibility, through the operation of numerous variants. Another possible reason could be that the 101 oriented pillars can further reorient with additional stress. Following a similar approach for the 100 orientation in compression, the martensite variant conversions are limited to variants 1, 1', 2 and 2'. The transformation strain associated with the austenite transforming to these martensite variants are determined to be -4.2% for all the cases. For case of tensile loading along different orientations, the preferred variants formed and the magnitude of the transformation strain and variant conversion strain can be determined following the same approach, based on the results summarized in Table 8.2.

8.4.2 Strain in the 111 and 100 Directions in Austenite during Thermal-Mechanical Cycling in NiTi

In Chapter Seven, during thermal-mechanical cycling of NiTi under compression, 111 oriented austenite experienced strains that were tensile in nature, opposite in sense when compared to the other orientations (See Fig. 7.10). By referring to Table 8.2, a compressive stress in the 111 orientation will initiate conversion to variants 1, 1' and 4, in which the austenite to martensite phase transformation in these three variants all produce -2.8% in strain. A similar determination for the 100 orientation results in conversion to variants 1, 1', 2 and 2', all of which generate strains of -4.2% during the phase transformation. The 111 direction is a hard direction while 100 is an easy direction implying that 100 oriented austenite transforms first generating larger strains in compression. The 111 oriented austenite being a hard direction transforms later and can only generate a maximum of 2.8% strain in compression. After the reverse transformation but in the presence of retained martensite, the need to satisfy compatibility causes the strain in the 111 oriented austenite to evolve in tension with increasing retained martensite (since the strain is smaller than in the 100 orientation). This problem is analogous to stresses that develop in composites as a result of differences in the coefficient of thermal expansion. Thus the observed behavior in Chapter 7 of this work can also be rationalized in terms of the preference for transformation of certain orientations of austenite and the corresponding phase transformation strains.

8.4.3 Strain in the 100 Direction in Austenite while Investigating the Effect of Upper-Cycle

Temperature on the Phase Transformation in NiTi

In the study of the effect of upper-cycle temperature on tensile load-biased strain-temperature response of NiTi presented in Chapter Six, the strain along the 100 direction decreases with increasing temperature at high stresses (as the amount of retained martensite is expected to be decrease). This is not the case in the 110 and 111 directions (See Fig. 6.9). From Table 8.2, the 100 orientation results in conversion to variants 1, 1', 2 and 2', all of which generate strains of -4.2% during the phase transformation. This implies that this orientation is incapable of generating a tensile strain during the phase transformation. Therefore, this hard direction under an externally applied tensile stress experiences a large mismatch with the applied tensile stress field and experiences large tensile strains as a result of the need to satisfy compatibility among grains. This explains why the strain in the 100 austenite grains is exceedingly large and decreases with heating as the stresses relax with temperature. Strains in the 111 and 110 austenite grains on the other hand increase as they relax to an equilibrium stress free state where the average strain lies between that of the 100 and the 111 and 110 oriented austenite grains. This is what is observed in Fig. 8.5. We emphasize that this behavior requires retained martensite to be present and is hence only observed in the 200 MPa and 300 MPa experiments.

8.5 Conclusions

This chapter revisits the methodology adopted for the theoretical determination of transformation and variant conversion strains (but with lattice parameters determined in this work) and makes direct comparisons with measurements from compression experiments in single crystal micron-scale NiTi pillars. Additionally, the preference for transformation among 100, 110 and 111

directions in austenite was examined from *in situ* neutron measurements during monotonic tension and compression in superelastic NiTi. The findings are summarized below:

1. Changes in the relative intensity of reflections during the phase transformation from *in situ* neutron diffraction measurements were compared to determine hard and easy directions for the austenite to martensite phase transformation. In compression, a preference for transformation of 100 oriented grains was observed, followed by a preference for 101 oriented grains and lastly by 111 oriented grains. This was consistent with previous predictions of the maximum resolved shear stress factor for phase transformation in the three orientations. The neutron diffraction measurements were also consistent with compression testing of micron-scale pillars. However, it was not straightforward to rank order the preferred orientations in tension due to changes in preference depending on the applied stress. Again this was consistent with previous predictions of the resolved shear stress factors for phase transformation in the three orientations.

2. The preference for transformation of austenite in different orientations along with the transformation and variant conversion strains were also successfully used to explain the strain evolution in the 111 and 100 directions in austenite during compressive thermal-mechanical cycling of NiTi and strain in the 100 direction in austenite while investigating the effect of upper-cycle temperature on the phase transformation in tensile-biased NiTi. In the first case, during the reverse transformation in the presence of retained martensite, the need to satisfy compatibility caused the strain in the 111 oriented austenite to evolve in tension with increasing retained martensite (since the strain is smaller than in the 100

144

orientation). This occurred despite the applied stress being compressive. In the second case, during the formation of retained martensite, the 100 orientation was incapable of generating a tensile strain when the applied stress was tensile. Therefore, this hard direction under an externally applied tensile stress experienced a large mismatch resulting in very large tensile stresses as a result of the need to satisfy compatibility among grains.

8.6 Tables

Table 8.1 Lattice correspondence between the 12 variants of martensite and parent austenite phase. The martensite is represented as M while the austenite is represented as *B2* [4].

Variant	$[100]_M$	$[010]_M$	$[001]_M$
1	$[100]_{B2}$	$[011]_{B2}$	$[0\text{-}11]_{B2}$
1'	$[\text{-}100]_{B2}$	$[0\text{-}1\text{-}1]_{B2}$	$[0\text{-}11]_{B2}$
2	$[100]_{B2}$	$[0\text{-}11]_{B2}$	$[0\text{-}1\text{-}1]_{B2}$
2'	$[\text{-}100]_{B2}$	$[01\text{-}1]_{B2}$	$[0\text{-}1\text{-}1]_{B2}$
3	$[010]_{B2}$	$[\text{-}101]_{B2}$	$[101]_{B2}$
3'	$[0\text{-}10]_{B2}$	$[10\text{-}1]_{B2}$	$[101]_{B2}$
4	$[010]_{B2}$	$[101]_{B2}$	$[10\text{-}1]_{B2}$
4'	$[0\text{-}10]_{B2}$	$[\text{-}10\text{-}1]_{B2}$	$[10\text{-}1]_{B2}$
5	$[001]_{B2}$	$[1\text{-}10]_{B2}$	$[110]_{B2}$
5'	$[00\text{-}1]_{B2}$	$[\text{-}110]_{B2}$	$[110]_{B2}$
6	$[001]_{B2}$	$[110]_{B2}$	$[\text{-}110]_{B2}$
6'	$[00\text{-}1]_{B2}$	$[\text{-}1\text{-}10]_{B2}$	$[\text{-}110]_{B2}$

Table 8.2 Austenite to martensite transformation and martensite variant conversion strains (%) calculated along $<111>_{B2}$, $<101>_{B2}$ and $<100>_{B2}$ directions

Transformation Strain (%)				Variant Conversion Strain (%)			
Variant	$<111>_{B2}$	$<101>_{B2}$	$<100>_{B2}$	Variant Conversion	$<111>_{B2}$	$<101>_{B2}$	$<100>_{B2}$
1	-2.8	-3.9	-4.2	3' → 1	-10.3	-11.1	-6.9
1'	-2.8	2.4	-4.2	6' → 1	0	0	-6.9
2	7.5	2.4	-4.2	5' → 1'	-10.3	0	-6.9
2'	-0.5	-3.9	-4.2	4 → 1'	0	4.5	-6.9
3	-0.5	7.2	2.7	6 → 2	10.3	0	-6.9
3'	7.5	7.2	2.7	4' → 2	10.3	4.5	-6.9
4	-2.8	-2.1	2.7	3 → 2'	0	-11.1	-6.9
4'	-2.8	-2.1	2.7	5 → 2'	0	0	-6.9
5	-0.5	-3.9	2.7	5 → 3	0	11.1	0
5'	7.5	2.4	2.7	6' → 3'	10.3	11.1	0
6	-2.8	2.4	2.7	5' → 4	-10.3	-4.5	0
6'	-2.8	-3.9	2.7	6 → 4'	0	-4.5	0
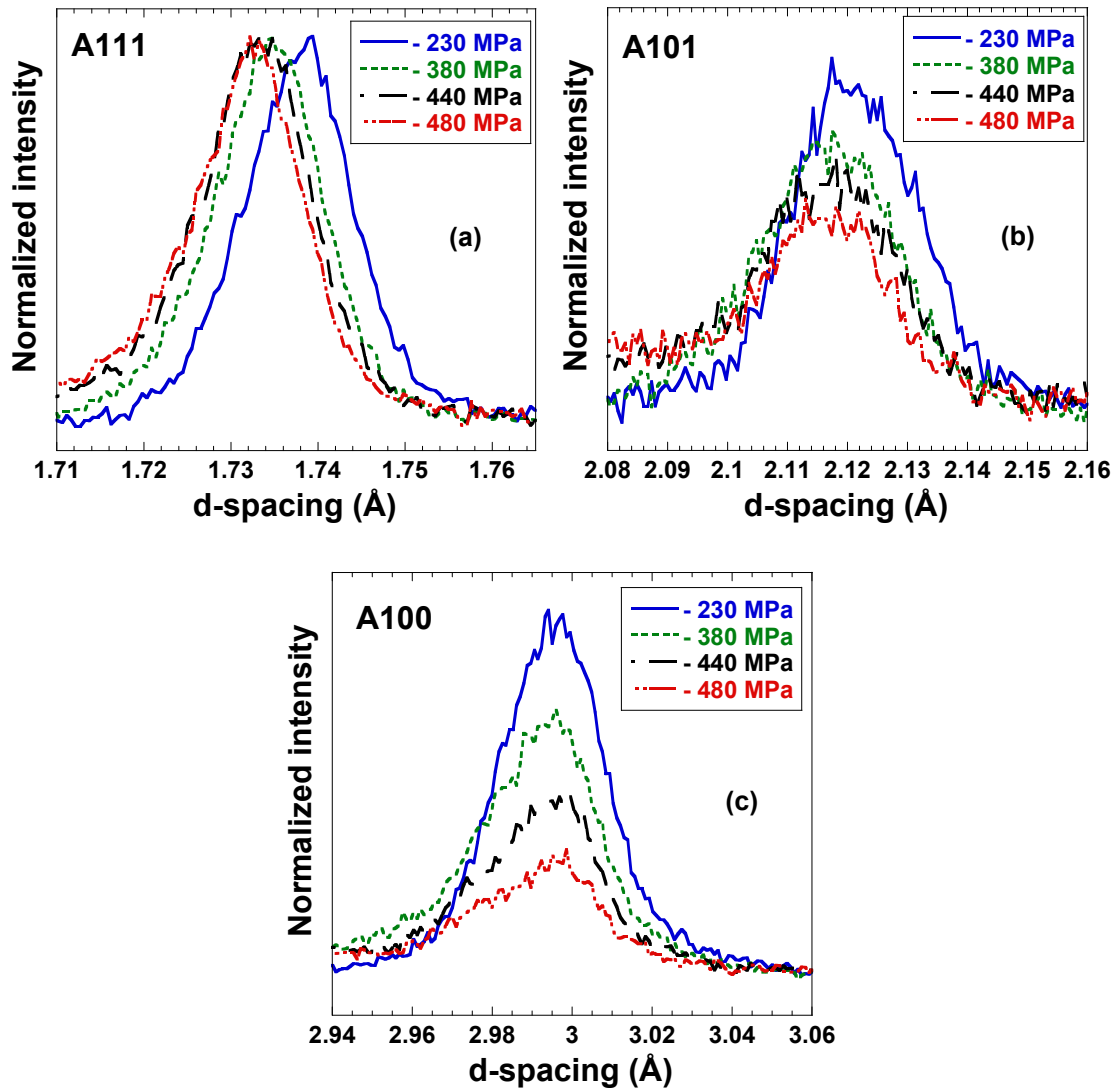
Figure 8.1 Sections of neutron diffraction spectra at various stresses acquired from NiTi during compressive loading. The spectra shown here are from diffracting grains oriented with their 111, 101 and 100 plane normals parallel to the loading direction. The entire spectra were normalized so that 111 peaks have the same peak intensity.
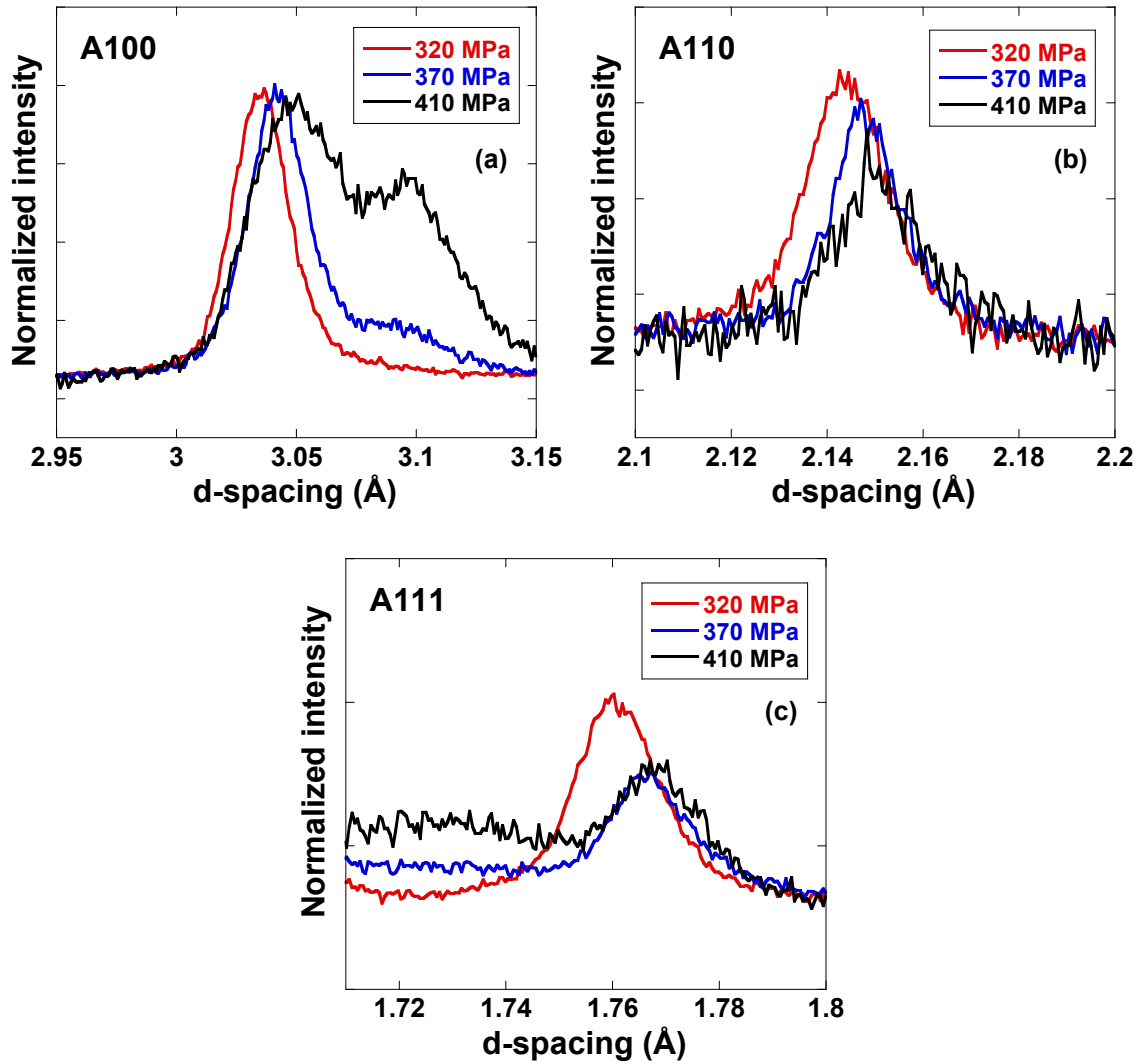
Figure 8.2 Sections of neutron diffraction spectra at various stresses acquired from NiTi during tensile loading. The spectra shown here are from diffracting grains oriented with their 100, 110 and 111 plane normals parallel to the loading direction. The entire spectra were normalized so that 100 peaks have the same peak intensity.
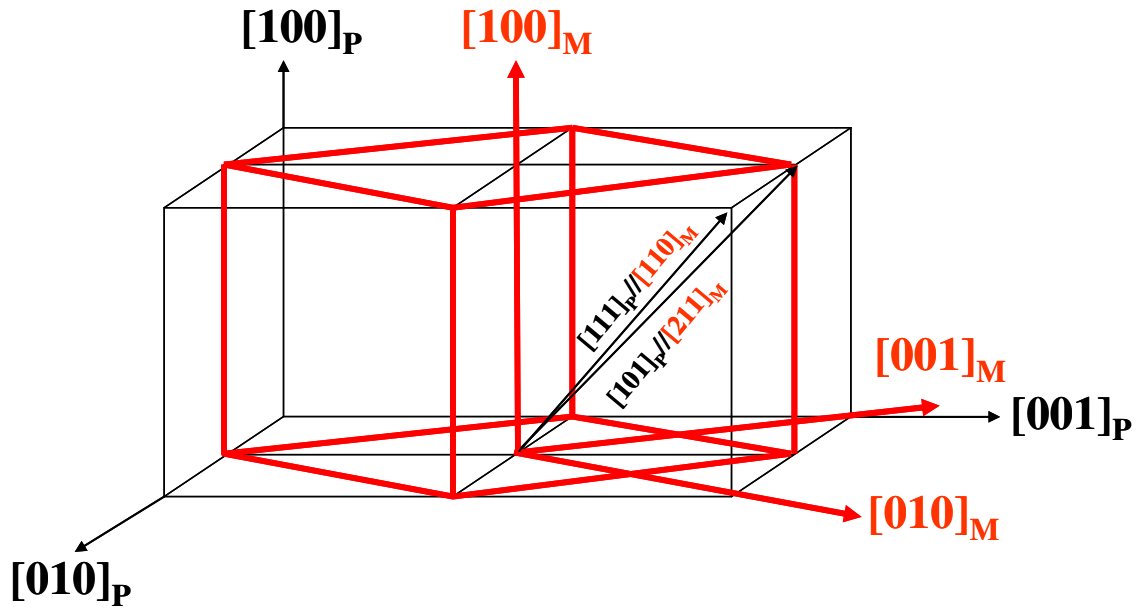
Figure 8.3 Schematic of the lattice correspondence between austenite and martensite for variant 1.
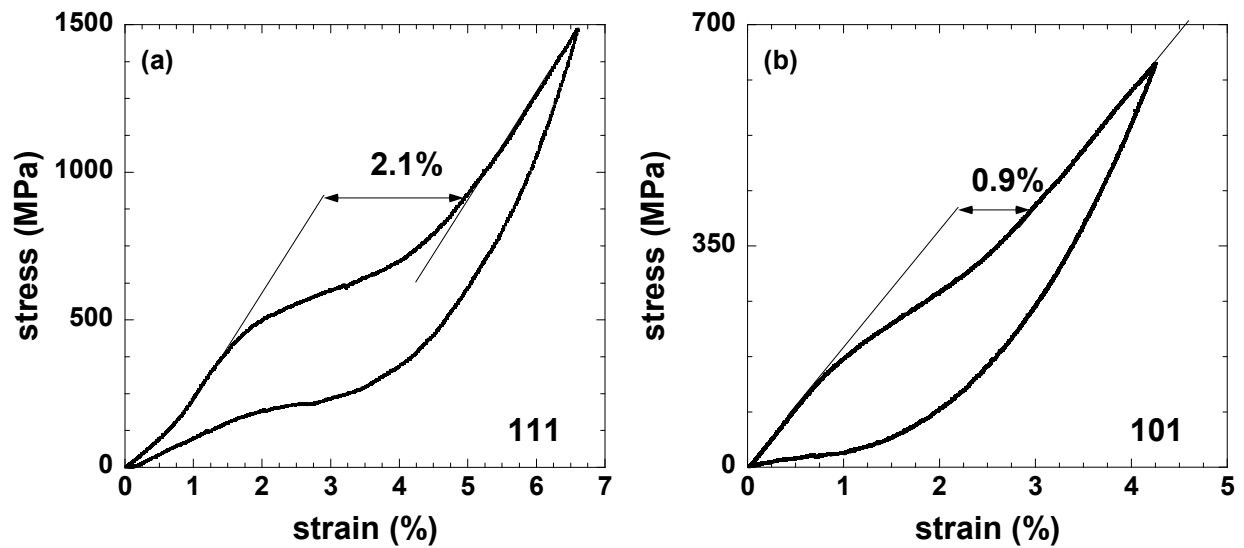
Figure 8.4 Micro-compression stress-strain response of (a) 111 oriented NiTi pillar (b) 101 oriented NiTi pillar. Graphs were obtained from Ref. [80].
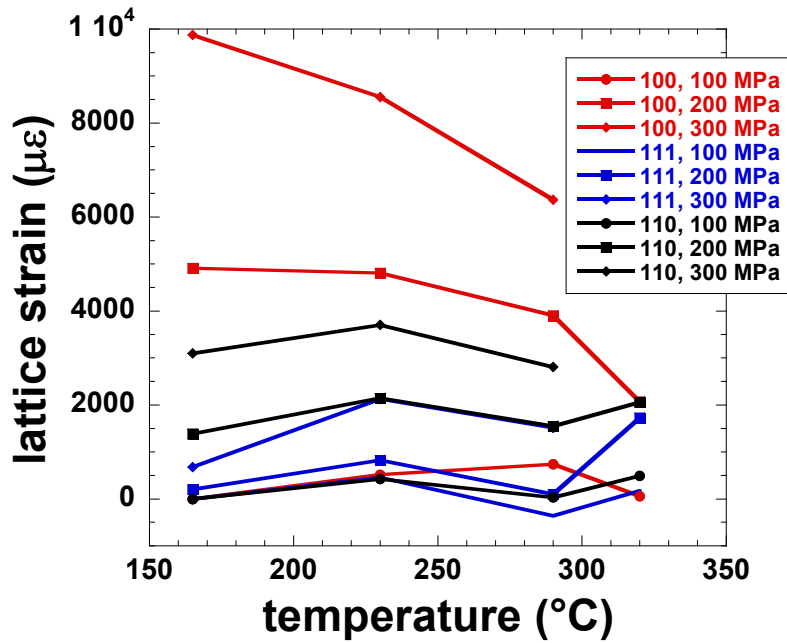
Figure 8.5 Lattice strain evolution in a direction perpendicular to the 100, 110, and 111 planes in the *B2* austenite phase as a function of upper cycle temperature and stress. The data shown here are from diffracting lattice planes perpendicular to the loading axis.

Appendix A: Calculation of transformation strains for variant 1 using MathCAD 13.1

Input lattice correspondence between B2 and B19' for a particular variant, so that

$$\begin{pmatrix} d_{11} & d_{12} & d_{13} \\ d_{21} & d_{22} & d_{23} \\ d_{31} & d_{32} & d_{33} \end{pmatrix} := \begin{pmatrix} 1 & 0 & 0 \\ 0 & 1 & 1 \\ 0 & -1 & 1 \end{pmatrix}$$

Normalization

$$\alpha := \sqrt{d_{11}^2 + d_{12}^2 + d_{13}^2} \qquad \beta := \sqrt{d_{21}^2 + d_{22}^2 + d_{23}^2} \qquad \gamma := \sqrt{d_{31}^2 + d_{32}^2 + d_{33}^2}$$

$$a := \frac{d_{11}}{\alpha} \qquad b := \frac{d_{21}}{\beta} \qquad c := \frac{d_{31}}{\gamma}$$

$$d := \frac{d_{12}}{\alpha} \qquad e := \frac{d_{22}}{\beta} \qquad f := \frac{d_{32}}{\gamma}$$

$$g := \frac{d_{13}}{\alpha} \qquad h := \frac{d_{23}}{\beta} \qquad i := \frac{d_{33}}{\gamma}$$

- **Initial Guesses: (Note: these values are arbitrary)**

$x := 1 \qquad p := 1 \qquad n := 1$

$y := 1 \qquad q := 1 \qquad l := 1$

$z := 1 \qquad r := 1 \qquad o := 1$

- **Solving Equations**

Given

$x \cdot 1 + y \cdot 0 + z \cdot 0 = a \qquad p \cdot 1 + q \cdot 0 + r \cdot 0 = d \qquad l \cdot 1 + n \cdot 0 + o \cdot 0 = g$

$x \cdot 0 + y \cdot 1 + z \cdot 0 = b \qquad p \cdot 0 + q \cdot 1 + r \cdot 0 = e \qquad l \cdot 0 + n \cdot 1 + o \cdot 0 = h$

$x \cdot 0 + y \cdot 0 + z \cdot 1 = c \qquad p \cdot 0 + q \cdot 0 + r \cdot 1 = f \qquad l \cdot 0 + n \cdot 0 + o \cdot 1 = i$

$$\begin{pmatrix} aa \\ bb \\ cc \\ dd \\ ee \\ ff \\ gg \\ hh \\ ii \end{pmatrix} := \text{Find}(x, y, z, p, q, r, l, n, o) \qquad \begin{pmatrix} aa & bb & cc \\ dd & ee & ff \\ gg & hh & ii \end{pmatrix} = \begin{pmatrix} 1 & 0 & 0 \\ 0 & 0.707 & -0.707 \\ 0 & 0.707 & 0.707 \end{pmatrix}$$

Check

$$\begin{pmatrix} aa & bb & cc \\ dd & ee & ff \\ gg & hh & ii \end{pmatrix} \cdot \begin{pmatrix} 1 \\ 0 \\ 0 \end{pmatrix} \cdot \alpha - \begin{pmatrix} d_{11} \\ d_{12} \\ d_{13} \end{pmatrix} = \begin{pmatrix} 0 \\ 0 \\ 0 \end{pmatrix}$$

$$\begin{pmatrix} aa & bb & cc \\ dd & ee & ff \\ gg & hh & ii \end{pmatrix} \cdot \begin{pmatrix} 0 \\ 1 \\ 0 \end{pmatrix} \cdot \beta - \begin{pmatrix} d_{21} \\ d_{22} \\ d_{23} \end{pmatrix} = \begin{pmatrix} 0 \\ 0 \\ 0 \end{pmatrix}$$

$$\begin{pmatrix} aa & bb & cc \\ dd & ee & ff \\ gg & hh & ii \end{pmatrix} \cdot \begin{pmatrix} 0 \\ 0 \\ 1 \end{pmatrix} \cdot \gamma - \begin{pmatrix} d_{31} \\ d_{32} \\ d_{33} \end{pmatrix} = \begin{pmatrix} 0 \\ 0 \\ 0 \end{pmatrix}$$

$$R := \begin{pmatrix} aa & bb & cc \\ dd & ee & ff \\ gg & hh & ii \end{pmatrix}$$

Austenite lattice parameter
a=3.001

$$d_{100} := 3.001 \qquad d_{110} := \frac{3.001}{\sqrt{2}}$$

Nascent Martensite lattice parameter

$$a := 2.8759 \quad b := 4.1531 \quad c := 4.5515$$

$$G := \begin{pmatrix} \dfrac{a}{d_{100}} & 0 & \dfrac{-c \cdot \sin\left(\dfrac{\beta - 90}{180} \cdot \pi\right)}{2 \cdot d_{110}} \\ 0 & \dfrac{b}{2 \cdot d_{110}} & 0 \\ 0 & 0 & \dfrac{c \cdot \cos\left(\dfrac{\beta - 90}{180} \cdot \pi\right)}{2 \cdot d_{110}} \end{pmatrix}$$

$$G = \begin{pmatrix} 0.958 & 0 & -0.092 \\ 0 & 0.979 & 0 \\ 0 & 0 & 1.069 \end{pmatrix}$$

$$R \cdot G \cdot \left(R^{-1}\right) = \begin{pmatrix} 0.958 & 0.065 & -0.065 \\ 0 & 1.024 & -0.045 \\ 0 & -0.045 & 1.024 \end{pmatrix}$$

$$v := \begin{pmatrix} 1 \\ 0 \\ 0 \end{pmatrix} \qquad \left[\frac{\left| R \cdot G \cdot \left(R^{-1}\right) \cdot v \right|}{|v|} - 1 \right] \cdot 100 = -4.169$$

$$v := \begin{pmatrix} 1 \\ 1 \\ 1 \end{pmatrix} \qquad \left[\frac{\left| R \cdot G \cdot \left(R^{-1}\right) \cdot v \right|}{|v|} - 1 \right] \cdot 100 = -2.814$$

$$v := \begin{pmatrix} 1 \\ 0 \\ 1 \end{pmatrix} \qquad \left[\frac{\left| R \cdot G \cdot \left(R^{-1}\right) \cdot v \right|}{|v|} - 1 \right] \cdot 100 = -3.88$$

CHAPTER NINE: CONCLUSIONS

Due to the stand-alone nature of each chapter in this dissertation, appropriate conclusions have already been included at the end of each chapter. This chapter provides a summary for completeness.

1. The thermal expansion tensor of *B19′* NiTi was determined through *in situ* neutron diffraction measurements performed during heating and cooling through the phase transformation in an unloaded sample of shape memory NiTi. The lattice plane specific strain evolution remained linear with temperature and was not influenced by intergranular stresses. The neutron diffraction measurements were consistent with macroscopic dilatometric measurements and a 30,000 grain polycrystalline self-consistent model. The accommodative nature of *B19′* NiTi resulted in macroscopic shape changes being offset (with temperature) from the start and finish of the transformation.

2. The elastic response of *B19′* martensitic NiTi variants as they exist in bulk, polycrystalline aggregate form was investigated. There was good agreement between the neutron diffraction measurements reported in this work and the stiffness tensor predicted from *ab initio* studies in Ref. [50]. Given the challenges in obtaining good quality single crystals of martensitic NiTi and the large number of independent constants in the stiffness tenor (thirteen), to the best of the authors' knowledge, this was the first reported validation of a theoretically predicted stiffness tensor for *B19′* martensite. The validation was accomplished by measuring elastic moduli in several directions, an average Young's modulus and Poisson's ratio, as well as by defining and measuring a unique Poisson's

ratio, and comparing the neutron experiments with theory. From the neutron diffraction measurements, an average Young's modulus of 134 GPa and a Poisson's ratio of 0.39 were determined. Corresponding measurements from extensometry resulted in a deflated Young's modulus due to variant reorientation and detwinning that occur even at lower stresses where the macroscopic stress-strain extensometry appeared mostly linear. Direct evidence of variant reorientation and detwinning at low stresses was provided in IPFs constructed from *in situ* neutron diffraction measurements during loading. The neutron diffraction measurements of direction dependent elastic moduli from martensite variants in a polycrystalline aggregate were influenced by crystalline symmetry (or lack thereof), intergranular interaction and constraints, and strain re-distribution among variants due to variant reorientation and detwinning. When variant conversion and detwinning relax most of the intergranular constraint arising from the neighboring variants, the moduli from neutron measurements compared well with the predictions of single crystal behavior.

3. The effect of the upper-cycle temperature on the load-biased strain-temperature response of shape memory NiTi was studied, focusing on the microstructural and micromechanical changes responsible for the macromechanical evolution. Results showed that the differences in transformation strain observed during the load-biased thermal cycling under various combinations of stress and upper cycle temperature were due to changes in the texture of the room temperature martensite. The volume fraction of the martensite retained in the austenite state additionally affected the transformation strain. When more martensite variants transformed into austenite by decreasing the applied stress and/or increasing the UCT, higher transformation strain was achieved. Some localized plasticity was expected to be induced in the grains of soft orientation (in terms of the propensity for

phase transformation from austenite to martensite). In tension, 111 oriented *B2* austenite grains are soft and localized plasticity may hence be responsible for the observed decrease in the 111 peak intensity.

4. The role of retained martensite during thermal-mechanical cycling in NiTi and NiTiPd shape memory alloys was investigated. The retained martensite was found to have limited contribution to the transformation strain. The majority of the strain generated as a result of the phase transformation from martensite to austenite was attributed to the martensite variants that transformed first and preferentially to austenite. For both NiTi and NiTiPd shape memory alloys, the transformation strain and the texture of the room temperature martensite remained mostly constant after the fourth cycle during load-biased thermal cycling, at the selected temperatures and stresses used in this study. The rate of evolution of texture and volume fraction of the retained martensite, and evolution of texture of the room temperature martensite, decreased with increased cycling. This effect combined with the fact that no appreciable texture changes occurred in the austenite phase, resulted in a decrease in the magnitude of the open-loop strain per cycle.

5. The preference for transformation among 100, 110 and 111 directions in austenite was examined from *in situ* neutron measurements during monotonic tension and compression in superelastic NiTi. Changes in the relative intensity of reflections during the phase transformation were compared to determine hard and easy directions for the austenite to martensite phase transformation. In compression, a preference for transformation of 100 oriented grains was observed, followed by a preference for 101 oriented grains and lastly by 111 orientated grains. This was consistent with previous predictions of the resolved shear stress factors for phase transformation in the three orientations. The neutron

diffraction measurements were also consistent with compression testing of micron-scale pillars. However, it was not straightforward to rank order the preferred orientations in tension due to changes in preference depending on the applied stress. Again this was consistent with previous predictions of the resolved shear stress factors for phase transformation in the three orientations. In addition, the preference for transformation of austenite in different orientations along with the transformation and variant conversion strains were also successfully used to explain the strain evolution in the 111 and 100 directions in austenite during compressive thermal-mechanical cycling in NiTi and strain in the 100 direction in austenite while investigating the effect of upper-cycle temperature on the phase transformation in tensile-biased NiTi. In the first case, during the reverse transformation in the presence of retained martensite, the need to satisfy compatibility caused the strain in the 111 oriented austenite to evolve in tension with increasing retained martensite (since the strain is smaller than in the 100 orientation). This occurred despite the applied stress being compressive. In the second case, during the formation of retained martensite, the 100 orientation was incapable of generating a tensile strain when the applied stress was tensile. Therefore, this hard direction under an externally applied tensile stress experienced a large mismatch resulting in very large tensile stresses as a result of the need to satisfy compatibility among grains.

REFERENCES

[1]   Bhattacharya K. Microstructure of Martensite: Why It Forms and How It Gives Rise to the Shape-Memory Effect? New York: Oxford University Press, 2003.
[2]   Bhattacharya K and James RD. Science 2005;307:53.
[3]   Otsuka K, Wayman CM. Shape Memory Materials. Cambridge: Cambridge University Press, 1999.
[4]   Otsuka K and Ren X. Prog. Mater. Sci. 2005;50:511.
[5]   Duerig TW and Pelton AR. "Ti-Ni Shape Memory Alloys" in Material Properties Handbook: Titanium Alloys: ASM International, 1994.
[6]   Miyazaki S, Jgo Y, Otsuka K. Acta metal. 1986;34:2045.
[7]   Funakubo H. Shape Memory Alloys. New York: Gordon and Breach, 1987.
[8]   Olander A. J. Amer. Soc. 1932;54:3819.
[9]   Greninger AB and Mooradian VG. Trans. AIME 1938;128:337.
[10]   Chang LC and Read TA. Trans. AIME 1951;191:47.
[11]   Buehler WJ and Wang FE. Ocean Eng. 1967;1:105.
[12]   Duerig TW, Melton KN, Stoeckel D, Wayman CM. Engineering Aspects of Shape Memory Alloys. London: Butterworth-Heinemann, 1990.
[13]   Massalski TB, Okamoto H, Subramanian PR, Kacprzak L. Binary Alloy Phase Diagrams. Materials Park: ASM Internatinal, 1990.
[14]   www.memry.com.
[15]   Mabe JH, Calkins F, Butler G. 47th AIAA/ ASME/ ASCE / AHS / ASC Structures, Structural Dynamics and Materials Conference. Newport, Rhode Island, 2002.
[16]   Takaoka S, Horikawa H, Kobayashi J, Shimizu K. The International Conference on Shape Memory and Superelastic Technologies, 2001. p.61.
[17]   Duerig T, Pelton A, Stockel D. Mater. Sci. Eng. A 1999;273-275:149.
[18]   Bigelow GS. Master thesis. Colorado School of Mines, 2006.
[19]   Hodgson DE. Using Shape Memory for Proportional Control. In: Duerig TW, Melton MN, Stökel D, Wayman CM, editors. Engineering Aspects of Shape Memory Alloys. London: Butterworth-Heinemann, 1990. p.362.
[20]   Dianoux AJ and Lander G. Neutron Data Booklet. Philadelphia: Old City Publishing, 2003.
[21]   Krawitz AD. Introduction to Diffraction in Materials Science and Engineering: Wiley-Interscience, 2001.
[22]   Hutchings MT, Withers PJ, Holden TM, Lorentzen T. Introduction to the Characterization of Residual Stress by Neutron Diffraction: Taylor & Francis, 2005.
[23]   Bacon GE. Neutron Diffraction: Oxford University Press, 1962.
[24]   Fitzpatrick ME and Lodini A. Analysis of Residual Stress by Diffraction using Neutron and Synchrotron Radiation: Taylor & Francis, 2003.
[25]   Bourke MAM, Dunand DC, Ustundag E. Appl. Phys. A 2002;74:S1707.
[26]   Rietveld HM. J. Appl. Cryst. 1969;2:65.
[27]   Rietveld HM. Acta Crystallographica 1966;20:508.

[28]   Larson AC and Von Dreele RB. General Structure Analysis System (GSAS). Los Alamos National Laboratory Report LAUR 86-748 2004.

[29]   Von Dreele RB. J. Appl. Cryst. 1997;30:517.

[30]   Bunge HJ. Texture Analysis in Materials Science. London: Butterworth-Heinemann, 1982.

[31]   Hutchings MT and Krawitz AD. Measurement of Residual and Applied Stress using Neutron Diffraction. Dordrecht: Kluwer Academic, 1992.

[32]   Vondreele RB, Jorgensen JD, Windsor CG. J. Appl. Crystallogr. 1982;15:581.

[33]   Daymond MR, Bourke MAM, VonDreele RB, Clausen B, Lorentzen T. J. Appl. Phys. 1997;82:1554.

[34]   Wessel P and Smith WHF. EOS Trans. Am. Geophys. Union 76, 329 1995.

[35]   Vaidyanathan R, Bourke MAM, Dunand DC. Acta Mater. 1999;47:3353.

[36]   Vaidyanathan R, Bourke MAM, Dunand DC. J. Appl. Phys. 1999;86:3020.

[37]   Standard test method for transformation temperature of nickel-titanium shape memory alloys by bend and free recovery. ASTM F2082-03, 2003.

[38]   Bourke MAM, Vaidyanathan R, Dunand DC. App. Phys. Lett. 1996;69:2477.

[39]   Rajagopalan S, Little AL, Bourke MAM, Vaidyanathan R. Appl. Phys. Lett. 2005;86:3.

[40]   Rathod CR, Clausen B, Bourke MAM, Vaidyanathan R. Appl. Phys. Lett. 2006;88:3.

[41]   Brinson LC. J. Intelligent Mater. Syst. Structures 1993;4:229.

[42]   Boyd JG and Lagoudas DC. Int. J. Plasticity 1996;12:805.

[43]   Patoor E, Lagoudas DC, Entchev PB, Brinson LC, Gao XJ. Mech. Mater. 2006;38:391.

[44]   Thamburaja P and Anand L. J. Mech. Phys. Solids 2001;49:709.

[45]   Fukami-Ushiro KL, Dunand DC. Metall. Mater. Trans. A 1996;27:193.

[46]   Brown DW, Sisneros TA, Clausen B, Abeln S, Bourke MAM, Smith BG, Steinzig ML, Tomé CN, Vogel SC. Acta Mater. 2009;57:972.

[47]   Nye JF. Physical Properties of Crystals. Oxford: Clarendon Press, 1985.

[48]   Clausen B, Tomé CN, Brown DW, Agnew SR. Acta Mater. 2008;56:2456.

[49]   Turner PA and Tomé CN. Acta Mater. 1994;42:4143.

[50]   Wagner MFX, Windl W. Acta Mater. 2008;56:6232.

[51]   Plietsch R, Ehrlich K. Acta Mater. 1997;45:2417.

[52]   Qiu S, Krishnan VB, Padula II SA, Noebe RD, Brown DW, Clausen B, Vaidyanathan R. Appl. Phys. Lett. 2009;95:141906.

[53]   Eshelby JD. Proc. Roy. Soc. Lond. 1957;A 241:376.

[54]   Clyne TW and Withers PJ. An Introduction to Metal Matrix Composites. New York: Cambridge University Press, 1995.

[55]   Sturcken EF and Croach JW. Trans. TMS-AIME 1963;227:934.

[56]   Vaidyanathan R, Bourke MAM, Dunand DC. Metall. Mater. Trans. A 2001;32:777.

[57]   Brown DW, Bourke MAM, Clausen B, Korzekwa DR, Korzekwa RC, McCabe RJ, Sisneros TA, Teter DF. Mater. Sci. Eng. A 2009;512:67.

[58]   Clausen B, Lorentzen T, Leffers T. Acta Mater. 1998;46:3087.

[59]   Daymond MR, Bourke MAM, Von Dreele RB. J. Appl. Phys. 1999;85:739.

[60]   Kocks UF, Tome CN, Wenk HR. Texture and Anisotropy: Preferred Orientations in Polycrystals and their Effect on Materials Properties. Cambridge, Cambridge University Press, 1998.

[61]   Padula II SA, Gaydosh DJ, Noebe RD, Bigelow GS, Garg A, Lagoudas D, Karaman I, Atli KC. In: Dapino MJ, Ounaies Z, editors. Behavior and Mechanics of Multifunctional

and Composite Materials 2008, vol. 6929. San Diego, California, USA: Proc. of SPIE, 2008. p.692912.

[62] Stebner A, Padula II S, Noebe R, Lerch B, Quinn D. J. Intell. Mater. Syst. Struct. 2009;20:2107.

[63] Bigelow GS, Noebe RD, Padula II SA, Garg A. In: Berg B, Mitchell MR, Proft J, editors. SMST - 2006. Pacific Grove: ASM International, 2006. p.113.

[64] Padula II S, Qiu S, Gaydosh D, Noebe R, Bigelow G, Garg A, Vaidyanathan R. Metall. Mater. Trans. A (in review).

[65] Dunand D, Mari D, Bourke M, Roberts J. Metall. Mater. Trans. A 1996;27:2820.

[66] Brill TM, Mittelbach S, W Assmus, Mullner M, Luthi B. J. Phys.: Condens. Matter 1991;3:9621.

[67] Mercier O, Melton KN, Gremaud G, Hagi J. J. Appl. Phys. 1980;51:1833.

[68] Melton KN and Mercier O. Acta metal. 1979;27:137.

[69] Miyazaki S. Zairyo 1990;39:1329.

[70] Hornbogen E. Fatigue Fract. Eng. Mater. Struct. 2002;25:785.

[71] Miyazaki S, Imai T, Otsuka K, Suzuki Y. Scr. Mater. 1981;15:853.

[72] Liu Y, Liu Y, Humbeeck JV. Scr. Mater. 1998;39:1047.

[73] Bigelow GS, Padula II SA, Garg A, Noebe RD. Proc. of SPIE 2007;6526:65262B.

[74] R. Noebe, T. Biles, Padula II SA. In: Soboyejo WO, Srivatsan TS, editors. Advanced Structural Materials: Properties, Design Optimization, and Applications. CRC Press, 2007. p.145.

[75] Gall K and Sehitoglu H. Int. J. Plasticity 1999;15:69.

[76] Gupta SP and Johnson AA. Trans. JIM 1973;14:292.

[77] Otsuka K, Sawamura T, Shimizu K. Physica Status Solidi 1971;5:457.

[78] Madangopal K, Singh J, Banerjee S. Scr. Metall. 1991;25:2153.

[79] Saburi T, Nenno S. In: Aaronson HI, Laughlin DE, Sekerka RF, Wayman CM, editors. Solid Phase Transformations. Warrendale, PA: TMS-AIME, 1981.

[80] Manjeri RM, Qiu S, Mara N, Misra A, Vaidyanathan R. J. Appl. Phys. 2010; 108:023501.

[81] Gall K, Sehitoglu H, Chumlyakov YI, Kireeva IV. Acta Mater. 1999;47:1203.

[82] Sehitoglu H, Karaman I, Anderson R, Zhang Z, Gall K, Maier HJ, Chumlyakov YI. 2000;48:3311.

[83] Miyazaki S, Kimura S, Otsuka K, Suzuki Y. Scr. Metall. 1984;18:883.